# QUASI-STATIONARY CONVECTIVE SYSTEMS FORMING PERPENDICULAR TO, AND ABOVE THE COLD POOLS OF, STRONG BOW ECHOES

A Thesis

by

KELLY M. KEENE

Submitted to the Office of Graduate Studies of
Texas A&M University
in partial fulfillment of the requirements for the degree of

MASTER OF SCIENCE

August 2011

Major Subject: Atmospheric Sciences

Quasi-Stationary Convective Systems Forming Perpendicular to, and Above the

Cold Pools of, Strong Bow Echoes

# QUASI-STATIONARY CONVECTIVE SYSTEMS FORMING PERPENDICULAR TO, AND ABOVE THE COLD POOLS OF, STRONG BOW ECHOES

A Thesis

by

KELLY M. KEENE

Submitted to the Office of Graduate Studies of
Texas A&M University
in partial fulfillment of the requirements for the degree of

MASTER OF SCIENCE

Approved by:

| | |
|---|---|
| Chair of Committee, | Russ S. Schumacher |
| Committee Members, | Courtney Schumacher |
| | Steven Quiring |
| Head of Department, | Kenneth Bowman |

August 2011

Major Subject: Atmospheric Sciences

## ABSTRACT

Quasi-Stationary Convective Systems Forming Perpendicular to, and Above the Cold Pools of, Strong Bow Echoes. (August 2011)

Kelly M. Keene, B.S., The University of Georgia

Chair of Advisory Committee: Dr. Russ S. Schumacher

The accurate prediction of warm-season convective systems, and the heavy rainfall and severe weather associated with them, remains a challenge for numerical weather prediction models. This study looks at one such circumstance in which back-building convection forms perpendicular to, and above the cold pool region behind strong bow echoes. We refer to this phenomenon as a "bow and arrow" because, on radar imagery, the two convective lines resemble an archer's bow and arrow. The "arrow" can extend over hundreds of kilometers and can cause damage from high winds, hail and flooding. Events of this nature pose a particular challenge to forecast because they require an accurate forecast of the earlier convection and the effects of that convection on the environment. In this study, radar and surface observations of four events are presented to identify common environmental conditions prior to the development of the back-building convection. Additionally, simulations of three cases using the Weather Research and Forecasting (WRF) model are analyzed in an attempt to understand the mechanisms responsible for initiating and maintaining the convective line. Due to

coarse resolution, observational analyses are only useful for inspection of the synoptic-scale. Model output from numerical simulations is utilized to examine the mesoscale in the vicinity of the convective arrow. Several environmental characteristics are evident in each of the studied cases. Strong southwesterly flow (inducing warm air advection and gradual isentropic lifting), in addition to directional and speed convergence into the convective arrow region possibly contribute to convection initiation. Horizontal wind speed shear and increased wind speed in the area surrounding the arrow may be associated with the linear orientation of the arrow. It seems as though when these ingredients are combined with thermodynamic instability, there is a greater possibility of formation and maintenance of a convective arrow behind a bow echo.

## ACKNOWLEDGEMENTS

This research is supported by the National Science Foundation grant AGS-0954908.

The composite radar reflectivity archives, as well as the Hovmöller time-distance diagrams of estimated rainfall rate, are provided by the National Center for Atmospheric Research's (NCAR) Mesoscale and Microscale Meteorology Division, sponsored by the National Science Foundation. Surface and upper-air observational analyses are obtained from the National Oceanic and Atmospheric Administration's (NOAA) Hydrometeorological Prediction Center. Precipitation estimates are provided by the National Weather Service's Office of Hydrology. Hail and wind reports are obtained from NOAA's Storm Prediction Center Archived Storm Reports. The North American Mesoscale model output is obtained from NCAR's Computational and Information Systems Laboratory Research Data Archive.

I would like to thank Morris Weisman and Clark Evans for providing forecast data from NCAR. I would also like to thank NCAR's Bluefire system for their computing resources.

I would like to thank the members of my graduate committee, Dr. Courtney Schumacher and Dr. Steven Quiring, for their service in reviewing my thesis, and all of their thoughts and suggestions regarding my work. I especially want to thank my advisor, Dr. Russ Schumacher, for all the guidance he provided to me over the past two years. I appreciate all of his patience, suggestions, intellect and

encouragement that helped me through the entire process, from conducting research to writing and defending my thesis. I also would like to thank his wife, Andrea Schumacher, who coined the term “bow and arrow,” providing a fitting name for the phenomenon that I studied in this project.

I would also like to thank the other student members of my research group, Charles Yost, Samantha Lynch, and Melissa Ackerman, for their assistance in improving my defense presentation. Finally, I would like to thank all of my friends and family for their endless support and encouragement, and a special thanks to my daughter, Brooklynn, for her patience and understanding throughout this entire process.

# TABLE OF CONTENTS

Page

# LIST OF FIGURES

FIGURE Page

FIGURE Page

FIGURE Page

FIGURE Page

FIGURE Page

# LIST OF TABLES

# 1. INTRODUCTION

A bow echo (Fujita 1978), as defined by the American Meteorological Society's Glossary of Meteorology, is "a bow-shaped line of convective cells that is often associated with swaths of damaging straight-line winds and small tornadoes." They are often associated with, and found embedded in, systems on a larger scale, known as Mesoscale Convective Systems (MCS). An MCS is defined as "a cloud system that occurs in connection with an ensemble of thunderstorms and produces a contiguous precipitation area on the order of 100 kilometers (km) or more in horizontal scale in at least one direction (AMS Glossary of Meteorology). In addition to severe winds and tornadoes, bow echoes can cause extensive damage from excessive precipitation in a short period of time. This is known as a flash flood.

Typically behind the bow echo region follows what is commonly known as the cold pool. Behind the area of strongest convection, evaporative cooling takes place, as a result of dry mid-tropospheric entrainment into the storm and a precipitating downdraft (Goff 1976). This dense cool air spreads out in a shallow layer along the surface behind the bow echo region, and forms what is known as an outflow boundary along its periphery. Because this boundary converges with warmer, less-dense air it often serves as a density current, creating lifting at its edges.

---

This thesis follows the style of *Weather and Forecasting.*

Corfidi (2003) shows that it is common for convection to form along the outflow boundary, as it would along a cold frontal boundary (although the secondary convection is typically weaker than that found along a strong cold front). This study investigates a circumstance in which back-building convection forms in an orientation that is perpendicular to, and above the cold pool region of, strong bow echoes (i.e. not along the outflow boundary). We refer to this phenomenon as a "bow and arrow" because, on radar imagery, the two convective lines resemble an archer's bow and arrow. A total of 14 cases have been observed during the course of this study; three of which will be analyzed in detail. These three cases have easily accessible data, have been reproduced by a numerical model, and appear to be representative of the larger population of events. The three cases are analyzed to determine environmental conditions that may lead to favorability for the occurrence of this phenomenon. The cases occur on 18 June 2006, 09 May 2008, and 15 September 2010 in the Great Plains region of the United States.

Observational analysis is conducted to determine the environmental conditions prior to the development of the bow. A combination of surface analysis, with an overlay of radar composites, and upper-air observations are reviewed. This helps to get a broad view of the synoptic-scale setting prior to, and during the phenomenon.

In order to obtain a further understanding of the environment on the mesoscale, the cases are reproduced through model simulation. Several different combinations of physical and initial conditions are used in an attempt to recreate

the bow and arrow as precisely as possible. Successful simulations are more deeply examined to reach a conclusion about the cause of such an event.

Model output is used to perform analysis of conditions at several layers of the atmosphere, as well as to pinpoint the origin of air parcels. This helps to obtain a better understanding of the temperature gradients and wind conditions the parcels encounter along their path into the arrow. These conditions could potentially play a role in upward motion of parcels and orientation of resulting convection. Additionally, verification of the impact of such storms is shown, as well.

Section two will provide background information regarding the nature of MCSs and the common properties of bow echoes. The data and methodology used to carry out the analysis of these events will be discussed in section three. Section four will give a discussion of the synoptic-scale environment prior to, and during, the events. Section five will break down the three cases and discuss the analysis of model output and impact verification. Concluding remarks and anticipated future work will be discussed in section six.

# 2. BACKGROUND AND MOTIVATION FOR THIS STUDY

## 2.1 Mesoscale Convective Systems

As mentioned in the introduction section, an MCS, a cluster of long-lived (≥ three hours) convective storms that are organized on the mesoscale, is a precipitating system that can sometimes embed bow echoes, or sometimes the entire system is made up of a bow echo. Occasionally bow and arrows are formed behind the bow echoes associated with these systems. There are several different types of MCSs, which include both linear and non-linear systems. A contiguous or nearly contiguous chain of convective echoes that form a convective line characterizes linear MCSs. The line can be oriented in a nearly straight line or a curved arc (Parker and Johnson 2000).

Parker and Johnson (2000) categorize linear MCSs into three different archetypes, based on the orientation of the stratiform precipitation to the line of strongest convection. The three types are shown in Fig. 2.1. The trailing stratiform (TS) archetype, shown in Fig. 2.1a, has a strong line of convection out front, with a weaker stratiform precipitation area behind it. The leading stratiform (LS) archetype (Fig. 2.1b) is shown to have the strongest convection trailing the weaker (stratiform) convection. The parallel stratiform (PS) archetype (Fig. 2.1c) displays a line of stronger convection, with the stratiform region paralleling to the left of the area of highest reflectivity. When surveying the distribution of the three archetypes for 88 MCS cases, they found that the most common type is the TS

archetype. They made up 58% of the 88 total linear cases they observed (although the LS and PS are not necessarily uncommon, each making up 19% of the cases). A total of 15 bow and arrow cases (discussed in more detail in section 3.1) are used in this study, and all are categorized as a TS archetype.

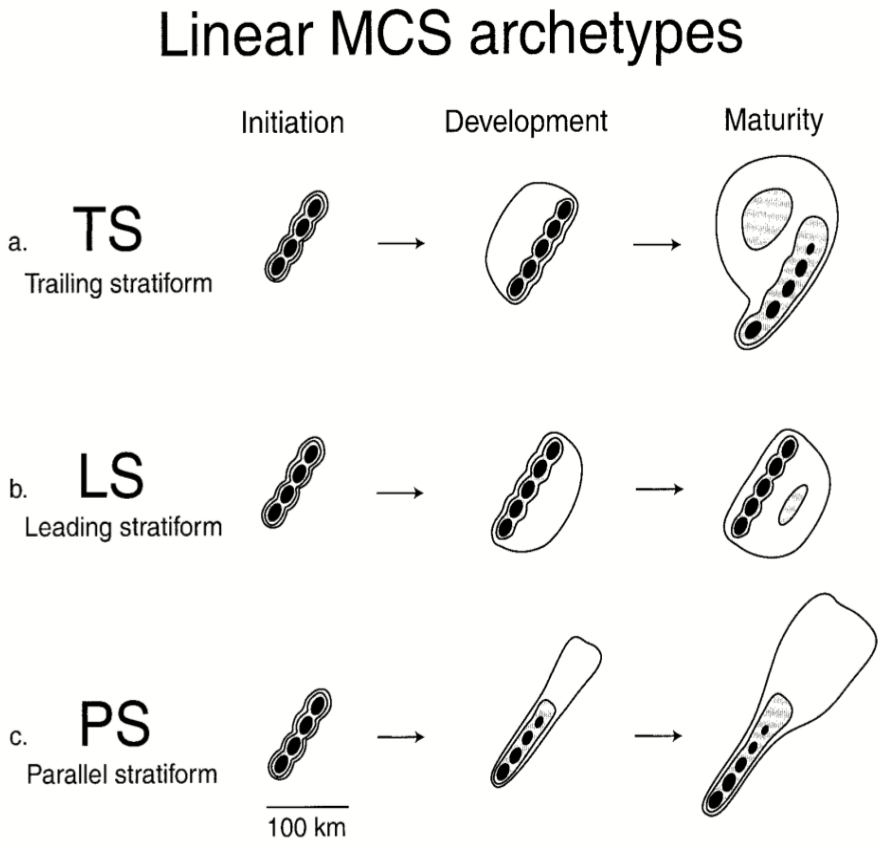


**Fig. 2.1.** Schematic reflectivity drawing of idealized life cycles for three linear MCS archetypes. (a) TS, (b) LS, and (c) PS. Approximate time intervals between phases: for TS 3-4 h; for LS 2-3 h; for PS 2-3 h. Levels of shading roughly correspond to 20, 40, and 50 dBZ. From Parker and Johnson (2005).

Houze et al. (1989) describe leading-line/trailing-stratiform MCSs using several defining characteristics. The leading convective line generally has an arc shape (convex toward the leading edge). The orientation is typically northeast to southwest, although this can vary depending on the overall motion of the system. The overall motion is rapid (greater than 10 m $s^{-1}$ and is usually directed toward the east or south. It has an overall solid appearance, with an area of high-reflectivity cells connected by an echo of more moderate intensity. The trailing stratiform region is usually very large (over $10^4$ $km^2$ over a horizontal area). It also tends to have a notched concave area at the rear edge, which has been shown to have an association with inflow of dry air (Smull and Houze 1985, 1987). The trailing stratiform region also usually has an area of secondary maximum intensity embedding within, and separated from the leading line.

Houze et al. (1989) also show that the TS MCSs are categorized based on symmetry (symmetric or asymmetric). In a symmetric case, the most intense cell(s) can be found anywhere along the convective line, as new cell growth occurs all along this line; however, the centroid is always located directly behind the center point of the leading line. An example of this is shown in Fig. 2.2a. An asymmetric TS MCS typically has the strongest convection located on its southern (or southwestern or western) end. The newer, more intense cells are located at one end of the convective line, while they decrease in intensity toward the other end. This causes the centroid to be located more toward the north (or northeast or east) end of the line. This is shown in Fig. 2.2b. The 14 cases in this study are

categorized as both symmetric and asymmetric types, although the symmetric type is more prevalent, as ten of the cases are this type, while only four are asymmetric.

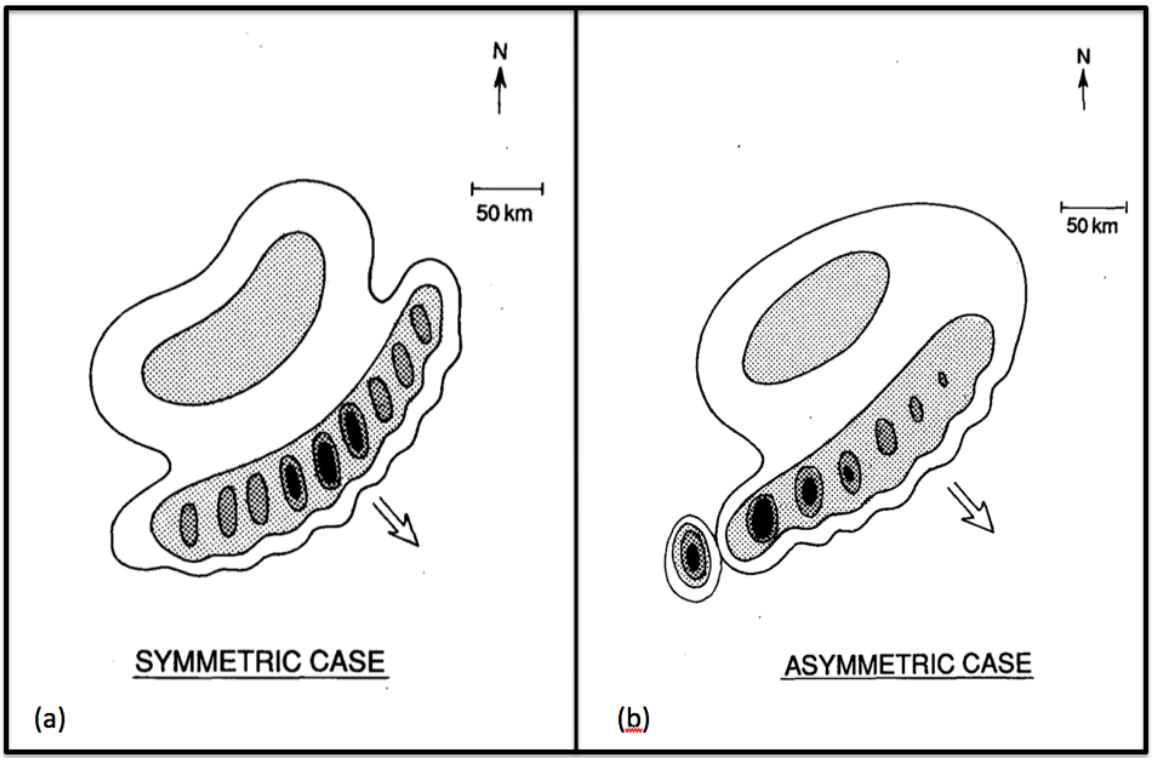


**Fig. 2.2.** (a) Schematic depicting symmetric type of leading-line/trailing stratiform mesoscale precipitation system organization. Large vector indicates direction of system motion. Levels of shading denote increasing radar reflectivity, with most intense values corresponding to convective cell cores. Horizontal scale and north arrow are shown. (b) As in Fig. 2.2a except for asymmetric type of leading-line/trailing-stratiform mesoscale precipitation system organization. From Houze et al. (1989).

Maddox (1980) studied a particular subset of MCSs known as mesoscale convective complexes (MCCs). MCCs tend to occur in unstable environments that contain horizontal convergence. This convergence is often associated with an east-west-oriented surface front and a low-level jet. Additionally it is common to find

warm air advection at the low levels of the environment prior to the development of these storms (Maddox 1983, Cotton et al. 1989).

Trier and Parsons (1992) conducted a study to determine the evolution of the environmental conditions preceding the development of nocturnal MCCs. They found much of the same evidence as Maddox (1983) and Cotton et al. (1989), regarding interception of the low-level jet with a surface frontal boundary in an area with horizontal convergence. They found that this tends to occur in a substantially unstable mesoscale region that provides the proper ingredients for air parcels to lift near the level of the low-level jet. A large north to south horizontal temperature gradient is also found at the mid-tropospheric levels.

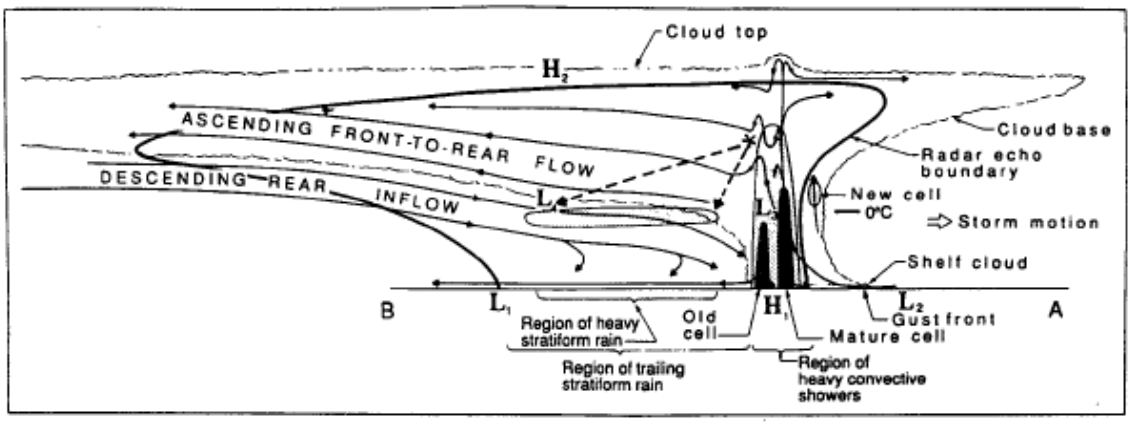


**Fig. 2.3.** Conceptual model of a squall line with a trailing stratiform area viewed in a vertical cross section oriented perpendicular to the convective line (i.e., parallel to its motion) (from Houze et al. 1989).

An important feature in mesoconvective systems is the rear-inflow jet. This is a current of air that is "generated in response to the development of an upshear-

tilted updraft, as the horizontal buoyancy gradients along the back edge of the expanding system create a circulation that draws midlevel air in from the rear. (Weisman 1992). They play a crucial role in supplying colder, drier air from the midlevels to boost the production of downdrafts from the system. Fig. 2.3 shows a schematic depicting a squall line in its mature phase, with a leading line of convective cells, and a stratiform precipitation region behind it. The rear-inflow jet is shown, originating at midlevels in the anvil cloud region, and descending toward the leading line.

## 2.2 Background of Bow Echoes

Bow echoes, mentioned in the introduction, are typically long-lived and cover an area of 60-100-km long. They are a mesoconvective structure that consists of a bow-shaped segment of smaller reflectivity echoes. These severe systems are known for producing long swaths of damaging winds, as well as heavy precipitation and occasionally tornadoes. They are commonly found to be associated with MCSs, which often embed squall lines that are capable of this bowing pattern (Weisman 1992).

Nolen (1959) first identified a structure known as a line echo wave pattern, which he defined as "a configuration of radar echoes in which a line of echoes has been subjected to an acceleration along one portion and/or a deceleration along that portion of the line immediately adjacent, with a resulting sinusoidal mesoscale wave pattern in the line." Hamilton (1970) determined that the bulge in the echo

was associated with a mesohigh, while the crest of the feature was associated with a mesolow. He is also credited for first noting the damaging capabilities of this phenomenon (mentioned above). The term "bow echo" was first coined by Fujita (1978).

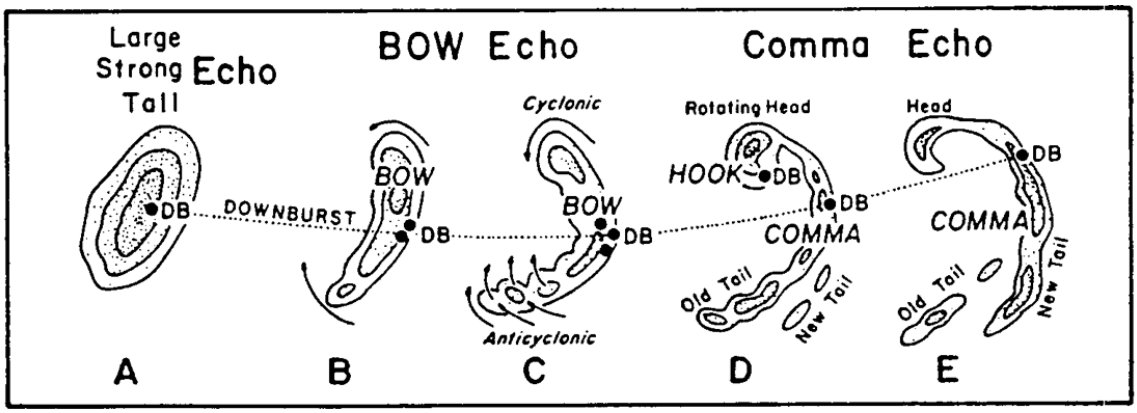


**Fig. 2.4.** (Adapted from Fujita 1978) A typical morphology of radar echoes associated with bow echoes that produce strong and extensive downbursts, labeled DB on the figure.

Fig. 2.4 depicts the morphology of radar echoes that are associated with bow echoes (Fujita 1978). The system typically begins with a strong, large single cell of convection that is either completely isolated or is part of a larger squall line. This cell then begins to extend, forming a bow-shape of segmented cells. This coincides with strengthening surface winds, where the strongest winds are found at the apex of the bow. When the bow echo reaches its phase of greatest intensity, it forms an area of cyclonic motion on one end, and anticyclonic motion on the other end. Eventually the system will evolve into a comma shape, only maintaining the cyclonic head on the left flank.

Analysis to determine the reason for a convective cell to evolve into a bow-shaped cell has been done with several modeling studies in the past. Weisman and Klemp (1986) found that precipitation that occurs due to an updraft, falls then evaporates, creating a cold pool that spreads out along the surface. This cold pool produces new cells in a bow-shaped arc, along its leading edge, due to convergence, which causes lifting and convection. The cells are oriented perpendicular to the vertical wind-shear vector. Using this logic, it seems that any cells that form behind the bow echo (e.g., the arrow) would be oriented parallel to the bow, and not perpendicular, like each of the events in this study. This is one reason (among many) why the perpendicular orientation of the arrow is so mystifying.

Klemp (1986) notes that as vertical wind shear increases, the ability to produce new cells along this arc also increases. They also found this to increase if the wind shear is maintained in only the lowest 2-3 km above ground level. Rotunno et al. (1988) found the reason for this to be associated with horizontal vorticity (which is caused by a gradient of buoyancy at the leading edge) matching opposing horizontal vorticity found in the low-level vertical wind shear. This creates a vertical jet of air at the leading edge of the cold pool, and that cool air creates more prominent lifting in that area.

Weisman et al. (1988) used model simulations to study the structure and evolution of squall lines. A simulation that features a bow echo is used to analyze the environmental conditions in place prior to the development of the bow. Convective available potential energy (CAPE) is 2400 J $kg^{-1}$. Over the lowest 2.5 km

above ground level, the vertical wind shear is 25 m $s^{-1}$, while the vertical wind-shear vector is oriented perpendicular to the leading convective line. Finally a strong cold pool exists and causes intense lifting, creating strong cells along the leading line.

Johns and Hirt (1987) examined the environmental conditions preceding convectively induced derechos. They found that the most significant ingredients that contribute to the conditions necessary for such a phenomenon are extremely high levels of instability, as well as the presence of a great amount of moisture at low-levels. They found that the average lifted index was -9 degrees C, and that surface dewpoints were typically greater than 20 degrees C. Additionally, they found wind speeds at the lower to mid-troposphere to be greater than those for other types of severe weather phenomena. They found that the average 700-hPa winds were 17 m $s^{-1}$, while the 500-hPa winds were 21 m $s^{-1}$.

Klimowski et al. (2004) conducted a study to determine the early evolution of bow echoes. They proposed a classification system for their organization. They described a *classic bow echo* (BE; Fig. 2.5a) as those that have no association with any large-scaled linear system. They are larger than a single thunderstorm, and mostly isolated from any other convection. The *bow echo complex* (BEC), shown in Fig. 2.5b is a system in which the bow echo is the primary convective structure, but may include other components, such as supercell thunderstorms. Przybylinski and DeClaire 1985, Johns and Hirt 1987, and Moller et al. 1994 describe this type of bow echo as associated with derechos. A *cell bow echo* (CBE; Fig. 2.5c) occurs on a very

small scale (10-25 km), and is not associated with any larger-scale system (Lee et al. 1992). The fourth type is the *squall line bow echo* (SLBE; Fig. 2.5d). This is the type that is part of a large-scale, quasi-linear convective system (Lee et al. 1992; and Przybylinski and DeClaire 1985).

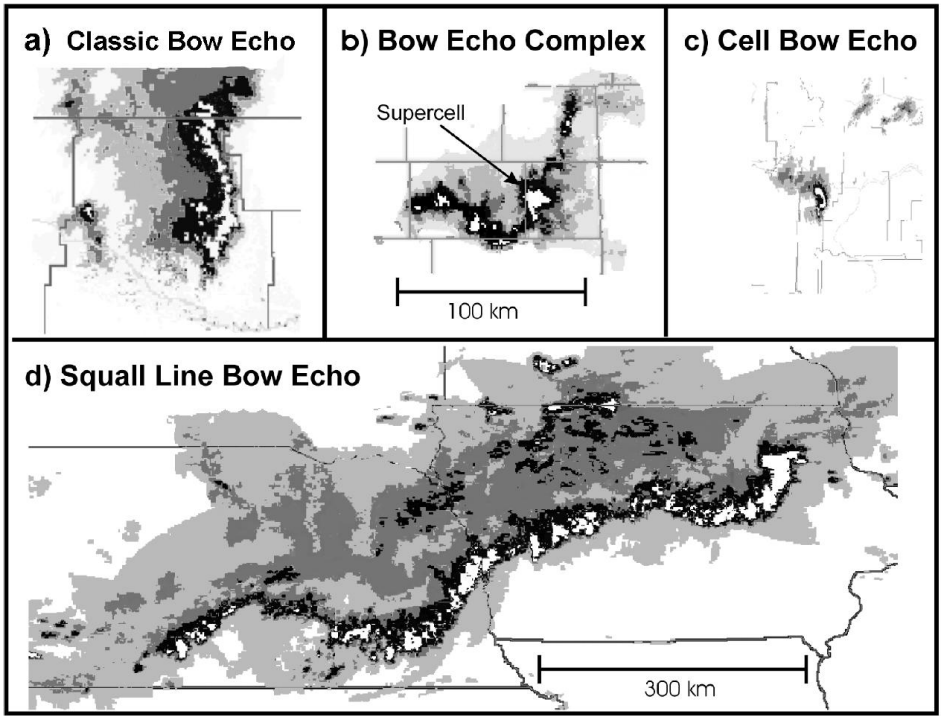


**Fig. 2.5.** The four general types of bow echoes described in the text. (a) BE, (b) BEC, (c) CBE, and (d) SLBE. The BE, BEC, and CBE are all relative to the scale as given in (b). Reflectivity shaded every 10 dBZ. From Klimowski et al. (2004).

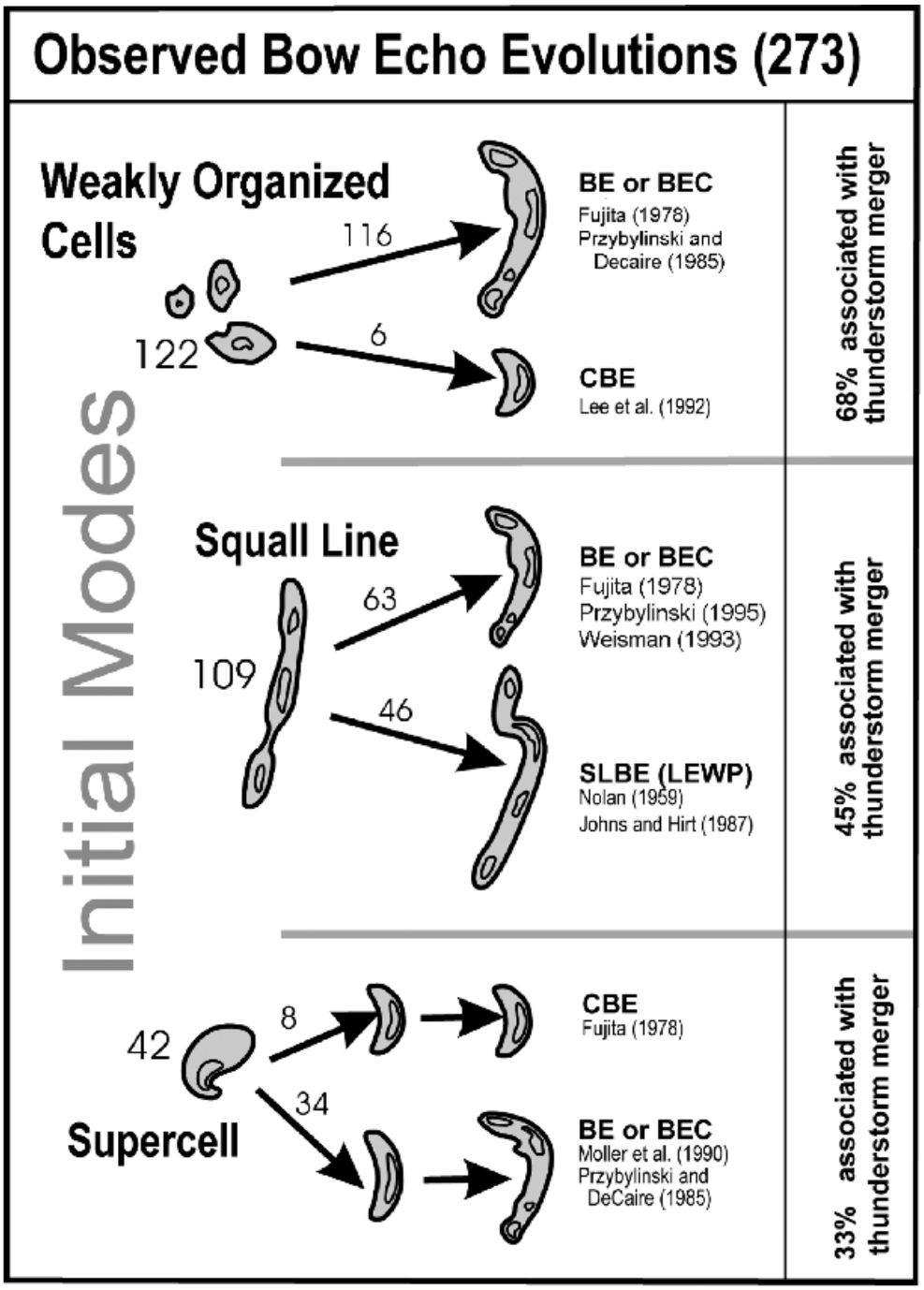


**Fig. 2.6.** Illustration of the primary evolutionary pathways for bow echoes observed in a study. The number of cases identified following each path is indicated above the arrows. References for representative bow echo cases are given. The percentage of bow echoes preceded by merging storms is given at the right. From Klimowski et al. (2004).

In addition to this classification system, Klimowski et al. (2004) identified three types convective organization modes from which bow echoes originate. They are weakly organized cells (WO), squall lines (SL), and supercells (SC). Fig. 2.6 illustrates the evolutionary transition from the original convective mode to the mature bow echo organization mode. Using visual identification from radar imagery, most of the bow echoes for the cases used in this study are determined to be the BE type, and originate from WO (8 cases). Other alternatives, however, are WO to BEC, SC to BE, and SC to BEC (2 cases for each of these).

## 2.3 Background of Extreme Rainfall and Flash Flooding

A bow and arrow is a phenomenon in which convection forms behind, and perpendicular to, a bow echo. The arrow region is typically quasi-stationary (or sometimes back-building), and found to be elevated above the cold pool. Chappell (1986) notes that the most significant flash floods are those that are produced by these types of systems, wherein several convective cells reach maturity and produce their heaviest rainfall over the same area. He states that quasi-stationary systems typically occur under conditions in which the wind profile is unidirectional and cell propagation offsets cell advection. Back-building, however, is a result of propagation exceeding advection, which causes overall upwind motion. Both of these types of events are significant in the sense that they are capable of producing large amounts of rainfall over a small area. A combination of the ample amount of precipitation resulting from the bow echo, and the additional rainfall associated

with the quasi-stationary (or back-building) convective arrow region, can result in a vast amount of precipitation to a particular area, which can lead to flash-flooding.

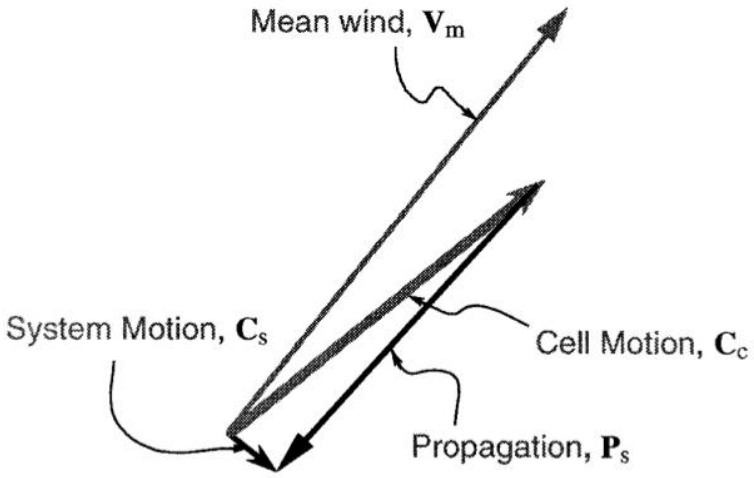


**Fig. 2.7.** Schematic showing the near cancellation between cell motion, $\mathbf{C_c}$, and propagation, $\mathbf{P_s}$. From Doswell et al. (1996).

Doswell et al. (1996) use a vector schematic to explain the reason quasi-stationary (or back-building) convective cells can produce flooding. Convective system movement, $\mathbf{C_s}$, is the vector sum of the contributions from $\mathbf{C_c}$ (convective cell movement, which is related to $\mathbf{V_m}$, which is the mean wind ), and $\mathbf{P_s}$, which is the propagation effect. They define propagation as "the contribution to system movement from the development and dissipation of individual convective cells." The near-cancellation of cell movement by propagation is what causes the slow movement of these cell systems (Fig. 2.7).

According to the National Oceanic and Atmospheric Administration (NOAA), flash flooding is defined as flooding that occurs within 6 hours of the precipitation that causes it. It causes more deaths each year in the United States than any other type of convective storm system. (NOAA 2011c). Doswell et al. (1996) note that the total precipitation at any particular point is directly proportional to the rate and duration of the rainfall. They emphasize that the rate is dependent on the available moisture in the atmosphere, vertical motion, and efficiency of precipitation, while rainfall duration is dependent on the size and speed of the storm system, as well as the variations of rainfall intensity within the convective cells.

As mentioned above, the amount of moisture in the air is a key ingredient in a convectively unstable environment, capable of maintaining systems that induce flash flooding. Glass et al. (1995), Junker et al. (1999), and Moore et al. (2003) all mention the significance of strong low-level winds (typically found in the form of a low-level jet), which are responsible for advecting this moisture, as well as warmer temperatures, into the area. They also find that the orientation of fronts, as well as outflow boundaries, plays a key role in extreme rainfall events. In addition, it is also common in areas containing low-level positive equivalent potential temperature ($\theta_e$) advection, as well as moisture convergence.

In a study using a sample of 116 extreme rain event cases in the eastern United States, Schumacher and Johnson (2005) find that 65% of the events were associated with MCSs. This coincides with the hypothesis presented by Doswell et al. (1996), that the majority of extreme rain events, including flash floods, are a

result of MCSs. Schumacher and Johnson (2005) also find that the second most common type (second to a parallel convective cell pattern, which causes a training effect of precipitation over one area) of extreme-rain-producing MCSs is that which is associated with a line of quasi-stationary or back-building convection. They note that this type of MCS occurs when convective cells are repeatedly forming upstream of the preceding cells. These cells will continually pass over a particular area, and this leads to a large amount of precipitation in a localized area. Back-building or quasi-stationary systems often form on the cool side of a boundary. This boundary is usually an outflow boundary produced by recent convection. The back-building (or quasi-stationary) convection found in the bow and arrow system, however, is not associated with the outflow boundary from the bow echo convection. Instead, it forms above the cold pool, in a perpendicular (to the bow) orientation that is puzzling, given the findings in previous studies.

## 2.4 The Role of Cold Pools in Mesoscale Convective Systems

Cold pools, as described in the introduction, are located in the region just behind convective cells or lines. They are one of the more distinctive features in MCSs and bow echoes, and are a result of a combination of dry mid-tropospheric entrainment into the storm and downdrafts that result from negative buoyancy. Because this air is cooler, it is denser, resulting in its location as a shallow layer close to the surface. Several processes may enhance downdraft development and strengthen cold pools. These processes include “sublimation and/or melting and

evaporation of precipitation falling through unsaturated air, precipitation drag, and vertical perturbation pressure gradients" (Corfidi, 2003).

Corfidi (2003) notes that the periphery of a cold pool often serves as a secondary boundary behind a thunderstorm due to the baroclinicity between it and its ambient air. Due to the convergence and ascent along this boundary (Purdom 1973; Charba 1974; Goff 1976), it is not uncommon to find new cell development along its edges. It is also pointed out that the new cell development is not necessarily evenly distributed along these boundaries, but is found to form in discrete zones in which the kinematic and/or thermodynamic factors are in place for such new development.

It is suggested by Corfidi (2003) that new cell development at the gust front is found, most commonly, in areas in which low-level inflow into the boundary is strongest. This is due to the fact that these areas will also serve as a region of greatest convergence (at low-levels). It is typical that the position of these areas is determined by the position and orientation of the low-level jet, although it is possible for these areas of maximum convergence to develop away from the low-level jet (along the boundary). This can occur if there is a substantial amount of relative motion between an outflow boundary and the low-level ambient wind. These factors are considered when analyzing the 14 cases in this study. A low-level jet seems to be at least evident, if not intense, in all of the analysis. This will be discussed in greater detail in the Observational Analysis, and Analysis of Numerical Model Simulations sections.

## 2.5 Motivation and Forecasting Difficulty

To obtain an accurate forecast, a numerical model needs to correctly predict multiple environmental conditions and resulting convective processes that take place before and throughout the duration of an event, such as the bow and arrow phenomenon. This is not an easy task for the models, which is somewhat evident by their failure to reproduce many of the cases found for this study. A lack of detection by numerical models typically leads to an incorrect forecast, since most forecasts are primarily dependent on model output and analysis. In addition to heavy precipitation and flooding, the arrow portion of a bow and arrow can also produce severe winds and hail.

It is important to consider the environmental conditions necessary for producing MCSs and bow echoes to determine the ingredients needed for a bow and arrow event, as well. It is expected that many of the conditions will be similar, but there should be key features that play a part in taking the bow echo a step further to produce the perpendicular convective line (the arrow) behind it. While it is also important to diagnose the problems that lie in the models for producing such an event, that is out of the scope of this study, and will be considered for future work. Nevertheless, identifying common environmental conditions prior to the development of the back-building convection, in addition to understanding the mechanisms responsible for initiating and maintaining the convective line should be beneficial to operational forecasters so that they can recognize such features.

Prior knowledge of these patterns should help them to make more accurate forecasts for this phenomenon in the future.

# 3. DATA AND METHODS

## 3.1 Selection of Cases

Although Bow and Arrow cases occur commonly enough that it raises a great concern for prediction purposes, they are not found to coincide with the majority of bow echo cases. This makes the process of searching for relevant cases for the dataset somewhat challenging. Since this phenomenon is not known to have been previously studied, there is no standard method already established for finding cases.

The first identification of the Bow and Arrow phenomenon was through previous work regarding extreme rainfall produced by convective systems (Schumacher and Johnson 2006). The phenomenon was not analyzed in detail, however. When the opportunity to study these cases became available, further investigation was needed to add more cases in an effort to increase the sample size and to create an awareness of the severity of this problem.

Although searching through daily radar archives is the most thorough method for finding additional cases, it is an extremely time-consuming task. To speed up the process Hovmöller time-distance diagrams of estimated rainfall rate (Carbone et al. 2002) are utilized to locate certain patterns that may be indicative of a bow and arrow event. In these diagrams, national composites of radar reflectivity are converted to rainfall rate using:

$$Z = 300R^{1.5} \quad (3.1)$$

where Z represents the reflectivity factor in $mm^6m^{-3}$ and R is the rainfall rate in mm $h^{-1}$.

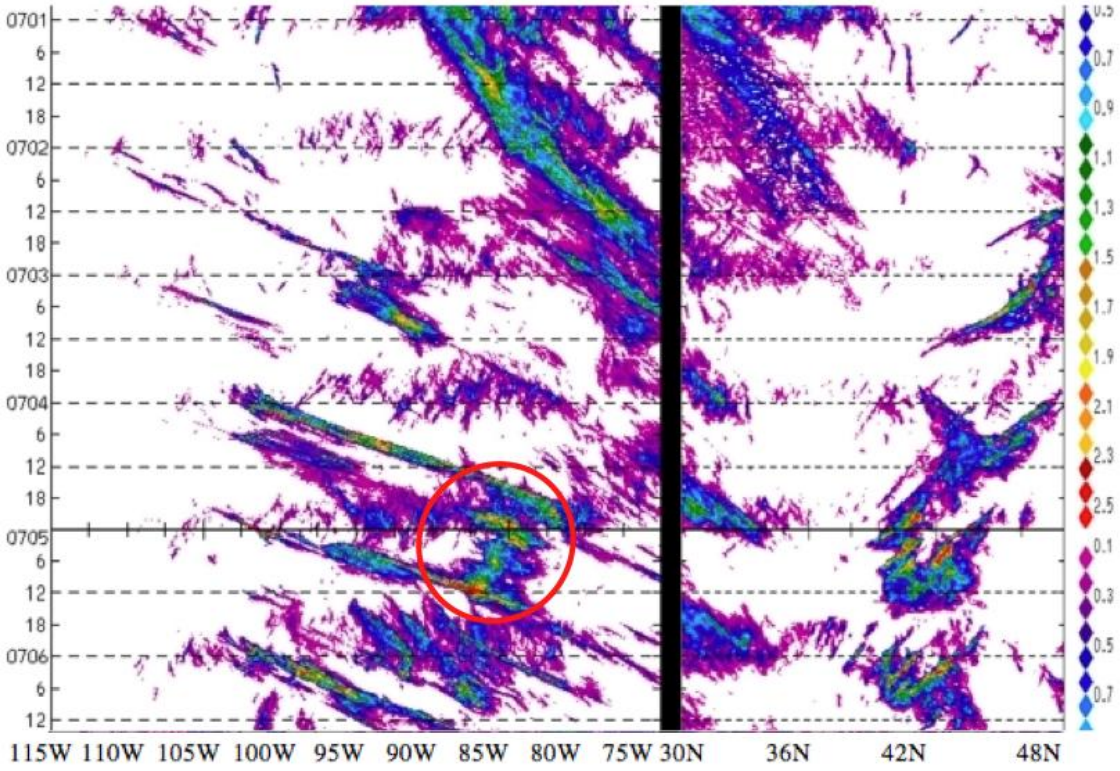


**Fig. 3.1.** Hovmöller diagram representing time-distance data of estimated rainfall from 1 July 2003 through 6 July 2003. The left X-axis represents evenly spaced longitudinal points across the United States (from 75 West to 115 West), while the right side of the X-axis shows points of latitude across the US (from 30N to 48N). The Y-axis represents days of the month, increasing toward the bottom. Each day is divided into six-hour time frames (0000, 0600, 1200, and 1800 UTC). From NCAR's MMM Precipitation Episodes website.

Fig. 3.1 shows an example of one such diagram from 5 July 2003 (a day on which one of the Bow and Arrow cases occurs). The area of interest is circled in red. This particular pattern portrays precipitation that occurs over two consecutive

days, moving from west to east as time progresses (shown by the two diagonal lines that extend, longitudinally, over time). It also shows quasi-stationary precipitation over one area (the area of increased precipitation that connects the two diagonal lines). This is indicative of a potential slow-moving MCS or other heavy precipitating event. Once the above-mentioned pattern is recognized, archived radar animations are observed to visually determine whether a bow and arrow event actually occurs.

Hovmöller diagrams are examined for a course of 12 warm seasons (1996 through 2007) to identify suitable cases. Several other cases were identified in radar imagery in real time, and others were previously identified among the cases analyzed by Schumacher and Johnson (2005, 2006). A total of 14 cases have been identified during the course of this study. The cases range from August 1999 through September 2010. All of the cases occur during the warm season (May through September), and in the Great Plains region of the United States, with the exception of one case that lies in the Midwest (Illinois and Indiana). This is the area and time period that is commonly associated with the occurrence of MCSs, as well as bow echoes (Augustine and Caracena, 1993).

**Table 3.1.** Dates of bow and arrow events listed in chronological order, with their location time of day, duration, and time between the passage of the bow echo, and the appearance of the first convective cells of the arrow. Times are in UTC, and are determined based on the time that the first convective cells in the arrow are observed. Some of the cases have multiple times listed because there were multiple arrows on that day. The duration is the length of time (in hours) that the arrow was present on radar reflectivity (not the duration of the MCS as a whole).

| Date | Location | Time (UTC) | Duration (hr) | Time from passage of bow echo to formation of arrow (hr) |
|---|---|---|---|---|
| 30 August 1999 | South Dakota | 0300, 0530 | 1.5, 3 | 1.5, 1.5 |
| 12 June 2003 | Texas | 0230 | 5 | 1 |
| 5 July 2003 | Indiana/Illinois | 0115, 0515 | 3, 2 | 4, 1.5 |
| 2 June 2004 | Texas | 0400 | 5 | 1.5 |
| 18 June 2006 | Texas | 0430 | 5 | 2 |
| 4 June 2008 | Kansas | 0315 | 3 | 1 |
| 26 June 2008 | Iowa/Missouri | 0645, 1100 | 3.5, 2 | 2, 1.5 |
| 3 May 2009 | Texas/Louisiana | 1225 | 2 | 2 |
| 8 May 2009 | Missouri | 1530 | 4 | 2 |
| 11 June 2009 | Texas | 0000 | 4 | 2.5 |
| 8 July 2009 | Iowa/Nebraska | 0600 | 3 | 2.5 |
| 18 June 2010 | Iowa | 1430 | 5 | 2.5 |
| 13 July 2010 | Missouri/Arkansas | 0830 | 2 | 5 |
| 15 September 2010 | Nebraska/Kansas/Missouri | 0300, 1130, 1600 | 6.5, 2, 4.5 | 1.5, 2.5, 1.5 |

Table 3.1 lists the events in chronological order, and gives the location for each event and the time that each occurred. The time listed is in UTC and is the time that the first convective cells appeared in the arrow region behind the bow echo. Several of the cases have multiple times because the bow and arrow phenomenon occurs more than once (in the same MCS) during that day. The

duration for all cases is between 1.5 hours and 6.5 hours, with an average of ~3.5 hours. The time difference between the passage of the bow echo to one location, and the formation of the arrow in that location, for all cases, is between 1 hour and 5 hours, with an average of ~2 hours. Fig. 3.2 is a map of the United States, with the spatial distribution of the events over the course of the 12 years. Red bullets are plotted in the location of the events, and are placed in the arrow region of the system. A total of 14 events are found during this time period, but 16 events are shown here. This is due to the 3 times the event occurs on 15 September 2010 (mentioned above), as it occurred in several locations. The multiple times the bow and arrow occurred for other events took place in the same location, so only one bullet is plotted for those events. Although only 14 cases are used in this study, it is likely that other events occurred during this time period, and were just not identified for this study.

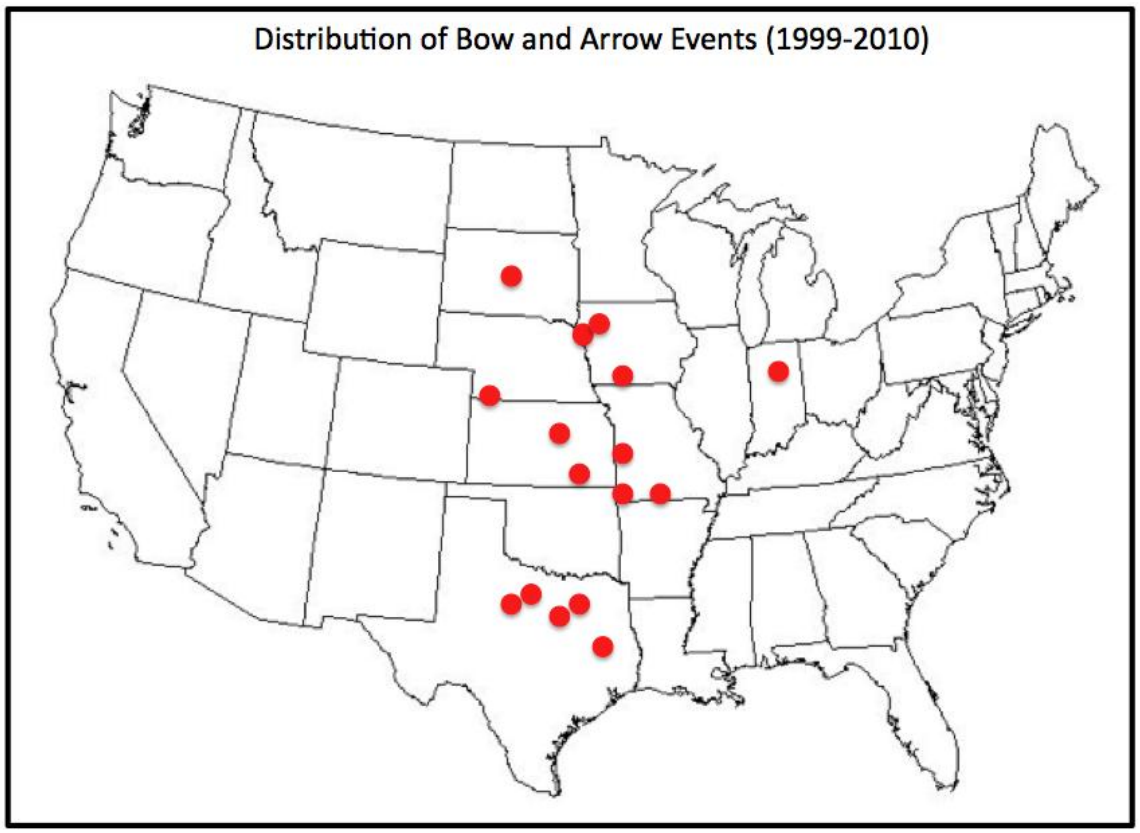


**Fig. 3.2.** Distribution of bow and arrow events from 1999-2010. Red bullets indicate location of the convective arrow in each case.

Three cases are numerically simulated in order to conduct further analysis on the output. These three cases all have easily accessible data, and seem to be representative of the total population of cases. The cases occurred on 18 June 2006, 08 May 2009, and 15 September 2010. Observational analysis, impact verification, data collection and model simulation for these three cases will be discussed in sections 3.2 through 3.5.

## 3.2 Observational Analysis

It is important to look at various observations to determine the actual characteristics of the environment prior to, and during the time of the bow and echo cases. Using surface analysis from the Barnes objective analysis method (Koch et al. 1983) and the General Meteorology Package (GEMPAK), plots showing sea-level pressure and temperature, with an overlay of composite radar reflectivity are studied. Analysis of these plots helps to determine any temperature advection, surface boundaries, and cold pools, as well as wind speed and direction, which might be explanatory for the cause of the arrow formation.

Several upper air observations, as well as surface analysis, are downloaded from the National Oceanic and Atmospheric Administration's (NOAA) Hydrometeorological Prediction Center (NOAA, 2011a). Surface analysis is available every three hours, and shows sea-level pressure contours, along with frontal boundaries. 850 and 500-hPa plots are also used. These are available every 12 hours. They provide information on upper air observations (which includes temperature, pressure, dewpoint temperature, wind speed and wind direction), geopotential height contours, temperature contours, and contours for dewpoint depression greater than, or equal to, 8 degrees Celsius (C). These plots are collected for times at least 24 hours in advance of the formation of the arrow. They help to analyze the synoptic-scale conditions of the atmosphere before the events occur.

### 3.3 Impact Verification

As mentioned in the introduction section, bow and arrows are capable of producing severe winds, hail, and heavy precipitation that can lead to flash flooding. It is important to show verification of this to emphasize the reason this phenomenon is so important to understand in detail for forecasting purposes. The impacts are verified using different methods.

The National Weather Service (NWS) Office of Hydrology stage IV analyses are performed on a 4-km grid. Rain gauge data are combined with hourly estimates derived from a composite of all the WSR-88Ds from around the country (Fulton et al. 1998). Three-hour estimates of rainfall are plotted. These three-hour time periods reflect the time the arrows pass over the regions. This is then compared to radar composites to determine the amount of estimated precipitation that fell in the arrow region.

Hail and severe wind information is collected from NOAA's Storm Prediction Center Archived Storm Reports (NOAA, 2011b). This site gives an archived map of the United States for each day, with bullets where reports of hail, severe wind, and tornadoes occur. Storm reports for dates on which bow and arrows occurred are compared to radar composites to determine potential storm reports that may have been caused by the arrow. Afterward, times and places of the actual storm reports are reviewed to determine whether the reports were likely a result of the arrow.

## 3.4 Data Collection and Model Simulation

### *3.4.1 15 September 2010*

North American Mesoscale (NAM) 212 grid (40 km) model output is used to determine the initial and boundary conditions for numerical simulation. It is found at the National Center for Atmospheric Research's (NCAR) Computational and Information Systems Laboratory (CISL) Research Data Archive. This data has a time resolution of six hours, and is retrieved for 14 September, beginning at 1200 Coordinated Universal Time (UTC) through 2400 UTC 15 September.

The Weather Research and Forecasting (WRF) model, version 3.2 is a system for atmospheric simulation and numerical weather prediction (Skamarock et al. 2011), and the one used in this study. The Advanced Research WRF (ARW) is the dynamics solver that is used for producing simulations, and the one that is used in this study. It includes different physics schemes, numerics/dynamics options, and initialization routines. After NAM data is collected, it is used as initial conditions and boundary conditions for the WRF-ARW simulations. The model is run with a large coarse mesh domain that includes two nested grids. The spatial resolutions of the grids are 27 km, 9 km, and 3 km, and there are 48 vertical levels. Domains for horizontal grids are shown in Fig. 3.3. Model output is saved every 15 minutes.

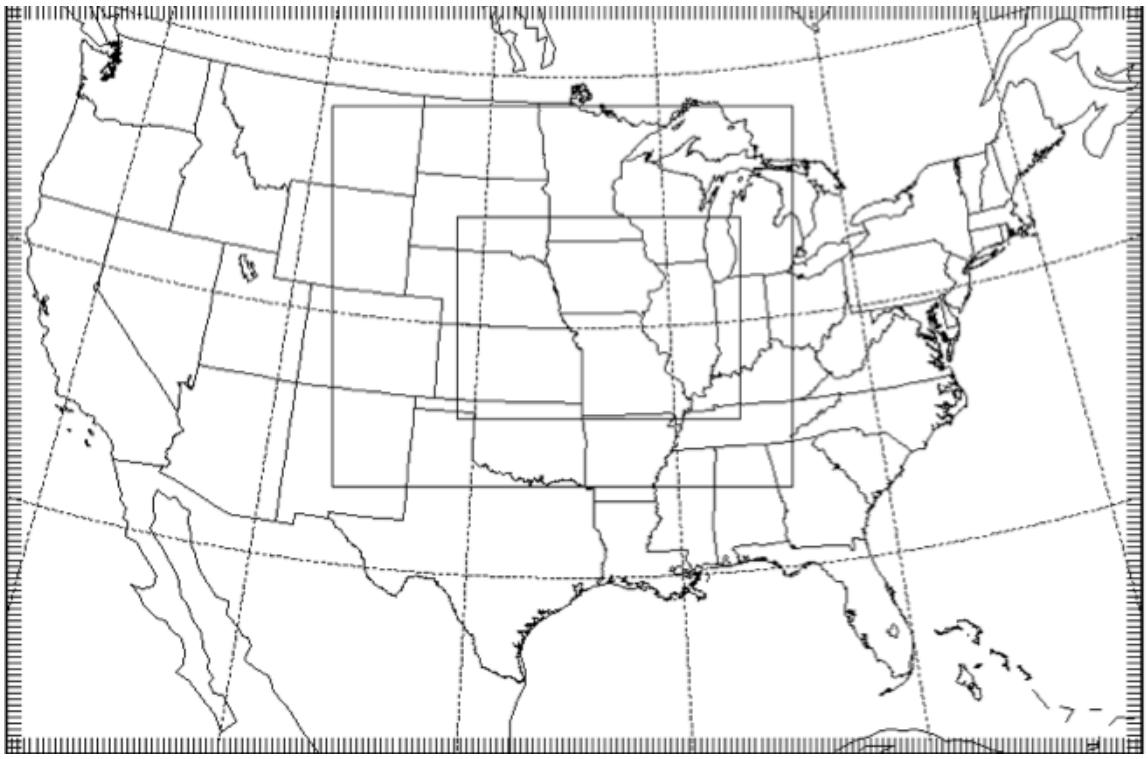

**Fig. 3.3.** Nested domain used for 15 September 2010 numerical simulation. Grid spatial resolution is 27 km, 9 km, and 3 km.

Per the recommendation of Skamarock and Weisman (2008), a positive definite moisture advection scheme is used. This scheme is found to significantly reduce positive bias for surface precipitation forecasts, especially in high precipitation cases. Configuration for microphysics schemes, cumulus parameterization schemes, and planetary boundary layer (PBL) schemes, is similar to those used in previous studies. Weisman et al. (2008) have shown success using the Yonsei University (YSU) boundary layer scheme (Hong and Lim 2006), and the WRF single-moment six-class microphysics scheme (WSM6; Hong and Lim 2006). Done et al. (2004) show success using the Kain-Fritsch cumulus parameterization

scheme (new ETA; Kain 2004). These three configurations are discussed in greater detail below.

WRF-ARW offers several microphysics schemes, which range from simplified physics best suited for idealized studies, to mixed-phase physics that are best for process studies and numerical weather prediction. The WSM6 is a scheme that includes ice, snow and graupel processes that are suitable for high-resolution simulations. It is noteworthy that this scheme has been found to create large, strong cold pools in previous strong convection simulations (Dawson et al. 2007). This is the microphysics scheme used for this particular case.

Cumulus parameterization schemes are adjustment and mass-flux schemes used for mesoscale modeling. Chosen for this case is the Kain-Fritsch scheme, a deep and shallow convection sub-grid scheme that uses a mass flux approach with downdrafts and a CAPE removal time scale. This parameterization is used on the two outer grids, which are more coarse, and unable to resolve individual updrafts.

The PBL scheme chosen for this case is the YSU scheme, which is a non-local-K (vertical diffusion coefficient) scheme with an explicit entrainment layer and parabolic K profile in an unstable mixed layer (Skamarock et al. 2011). This scheme is found to be successful in the WRF model because it produces a more realistic structure of the PBL and its development.

### *3.4.2 18 June 2006 and 08 May 2009*

Each year, daily 36-hour warm season forecasts are conducted by the National Center for Atmospheric Research (NCAR; Weisman, et al. 2008). Initial and boundary conditions are determined using the 40-km NAM/Eta analysis. A forecast is initialized each day at 0000 UTC and boundary conditions are updated every three hours. The data is fed into the WRF-ARW, and uses 3-km horizontal grid spacing over a large domain centered on the United States. Data for these two particular cases is obtained from NCAR through personal communication.

The WRF output for the 18 June 2006 case has a time resolution of one hour. The output is collected, beginning on 17 June at 1200 UTC and ending on 18 June at 0600 UTC. The microphysics scheme used is the above-mentioned WSM6. Since this simulation used only a single high-resolution grid, cumulus parameterization is unnecessary. The PBL scheme used is the Mellor-Yamada-Janjic (MYJ) scheme (also known as the Eta operational scheme; Janjic 1994). This scheme is one-dimensional, and is a prognostic turbulent kinetic energy scheme with local vertical mixing. This scheme was tested and showed positive results when used on cases with heavy precipitation.

For the 08 May 2009 case, the WRF output has a time resolution of 15 minutes. This output collected begins on 7 May at 1200 UTC and ends on 9 May at 0000 UTC. The microphysics scheme used is the New Thompson et al. scheme (Thompson et al. 2008). It is a scheme that also includes ice, snow and graupel processes suitable for

high-resolution simulations, but also adds rain number concentration. It is the updated, and most recent, version of the previous Thompson microphysics schemes. Again, since the domain is a single high-resolution grid, no cumulus parameterization is used. The PBL scheme used is the MYJ scheme.

### 3.5 Analysis of Model Output

After all data has been collected and simulations are run, the next step is to analyze the output. The Read/Interpolate/Plot, version 4 (RIP4) is a Fortran program that creates plots from mesoscale model output, and is the primary tool used here. The program has the capability to create both horizontal and vertical cross-section plots, vertical profiles and soundings, as well as to calculate trajectories (Skamarock et al. 2011). All of these are utilized for diagnosing model output for this project.

Once a simulation is run, RIP4 is used to create radar imagery to be analyzed for accuracy, as compared to composite radar observations. Simulated radar reflectivity is plotted over the chosen domain, and shown on an overlay of United States state borders, as shown in an example in Fig. 3.4. This imagery is used to determine whether the simulation is successful in the recreation of the bow and arrow event from that day. Often, even if the simulation is successful, the location and time may differ from reality. Since the primary concern is with the processes leading up to the formation of the bow and arrow, these simulations are still useful

despite the errors in time and location. If an event can be simulated, further analysis can be conducted to determine the ambient conditions.

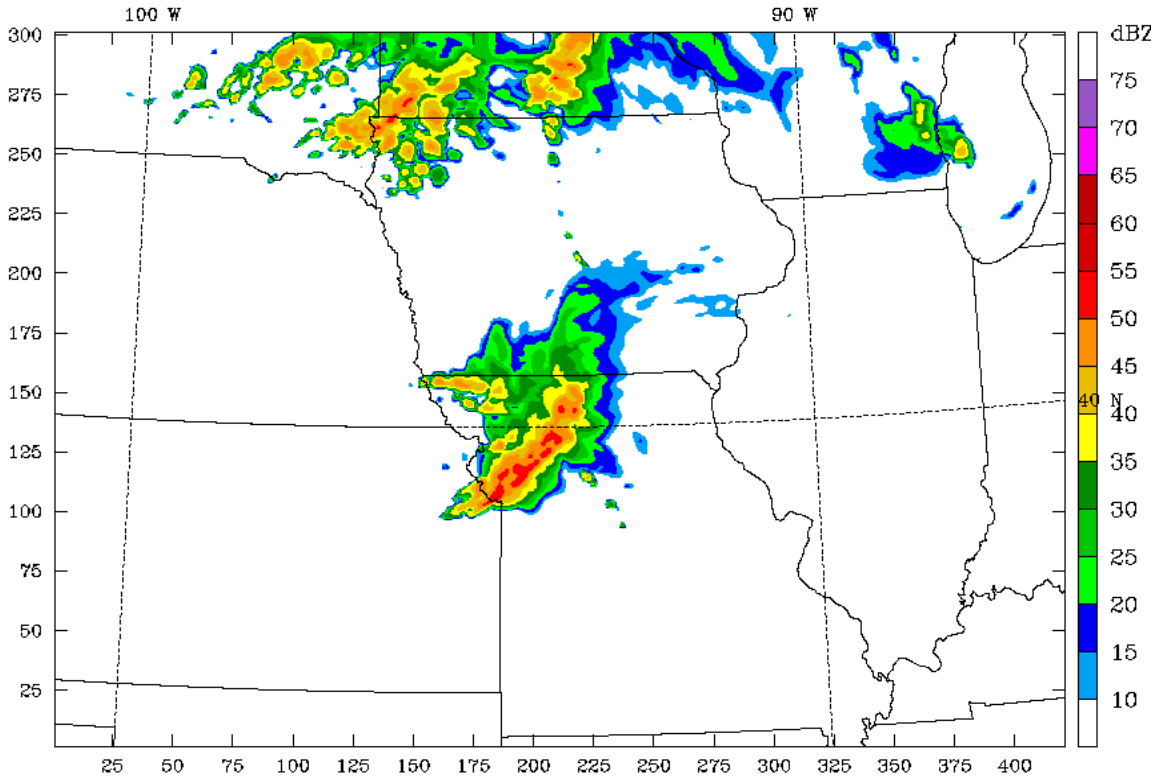


**Fig. 3.4.** Radar image created using the RIP4 program and WRF model output for 1710 UTC 15 September 2010. This plot shows simulated radar imagery on the specified 3 km nested domain, overlaying the US states. Color represents radar reflectivity in decibels (dBZ).

Once a case is determined to be successful, based on viewing simulated radar imagery, it is important to diagnose the environmental conditions in place prior to the development of the arrow behind the bow. Several plots at various pressure levels are analyzed for wind direction and strength, as well as horizontal temperature variations over the domain. This also gives information regarding any

convergence of wind that may be responsible for initiating the arrow, as well as any wind shear that may play a role in the linear orientation of the arrow's convection.

Calculating backward trajectories will help to determine where air parcels (that are part of the inflow into the convective arrow) are originating. It is important to determine exactly where the primary updrafts are occurring within the arrow region so that the trajectories can be plotted from these areas. The typical level for the strongest updrafts is near the 500- hectopascal (hPa) level. This level may differ slightly with different cases. The region of strongest updrafts is determined, to pinpoint the exact location to begin the backward trajectories.

Viewing the backward trajectories in the X-Y plane gives representation of an air parcel's horizontal flow over several hours leading up to the initiation of convection in the arrow region. Fig. 3.5 shows an example of a horizontal trajectory from the 08 May 2009 case. The plot shows the area in the high-resolution domain, where the x-axis represents longitudinal distance and the y-axis represents latitudinal distance.

Looking at the trajectories in the X-Z plane is useful for determining the time, as well as the level in the atmosphere, at which lifting occurs. This helps to decide which pressure level plots should be investigated for lifting mechanisms, as well as the path that air parcels take as they enter the arrow. Fig. 3.6 is an example of a vertical backward trajectory (also from 08 May 2009). Distance is shown along the x-axis, while pressure decreases upward along the y-axis.

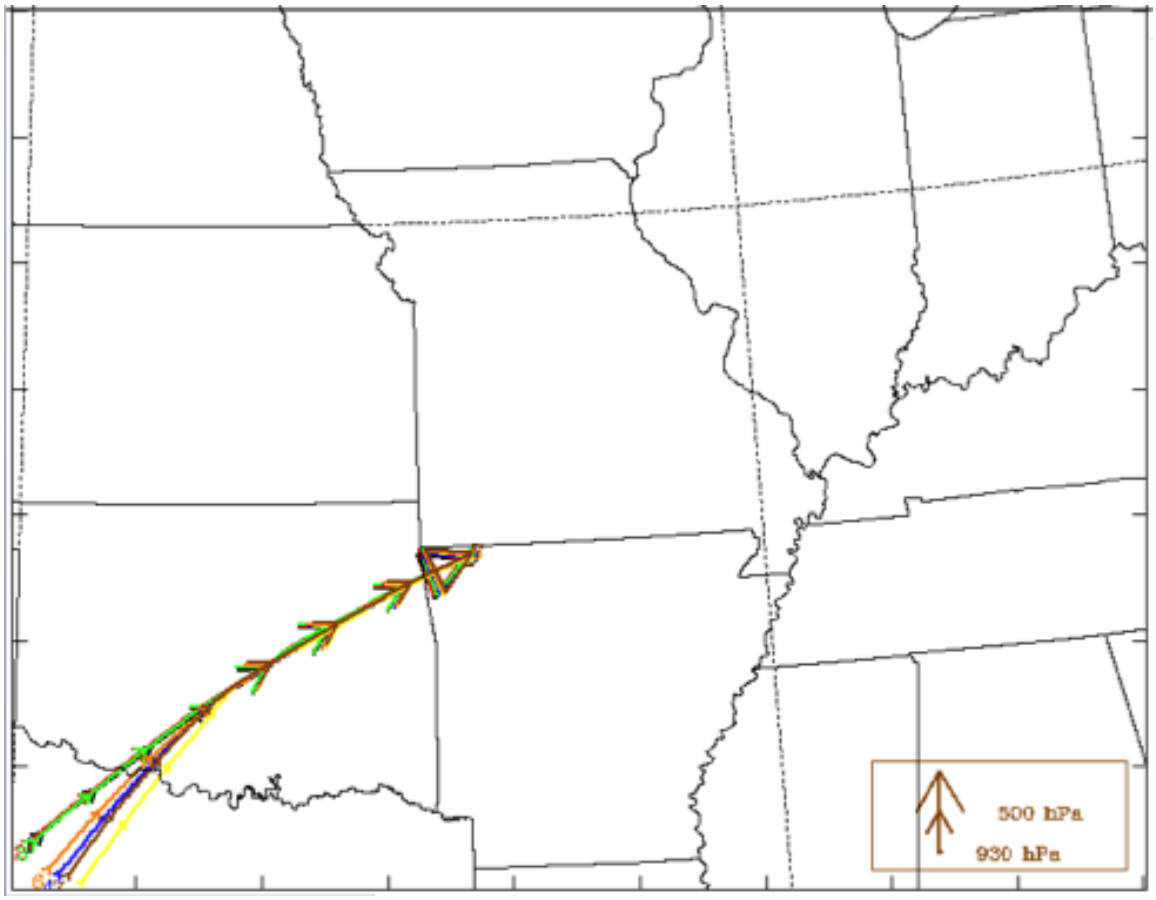


**Fig. 3.5.** Horizontal backward trajectory from 08 May 2009 (1445 UTC). The x-axis represents longitudinal distance, while the y-axis represents latitudinal distance. Arrows plotted along the path represent hourly increments. The size of the arrows increases as the vertical height in the atmosphere increases, or the pressure decreases.

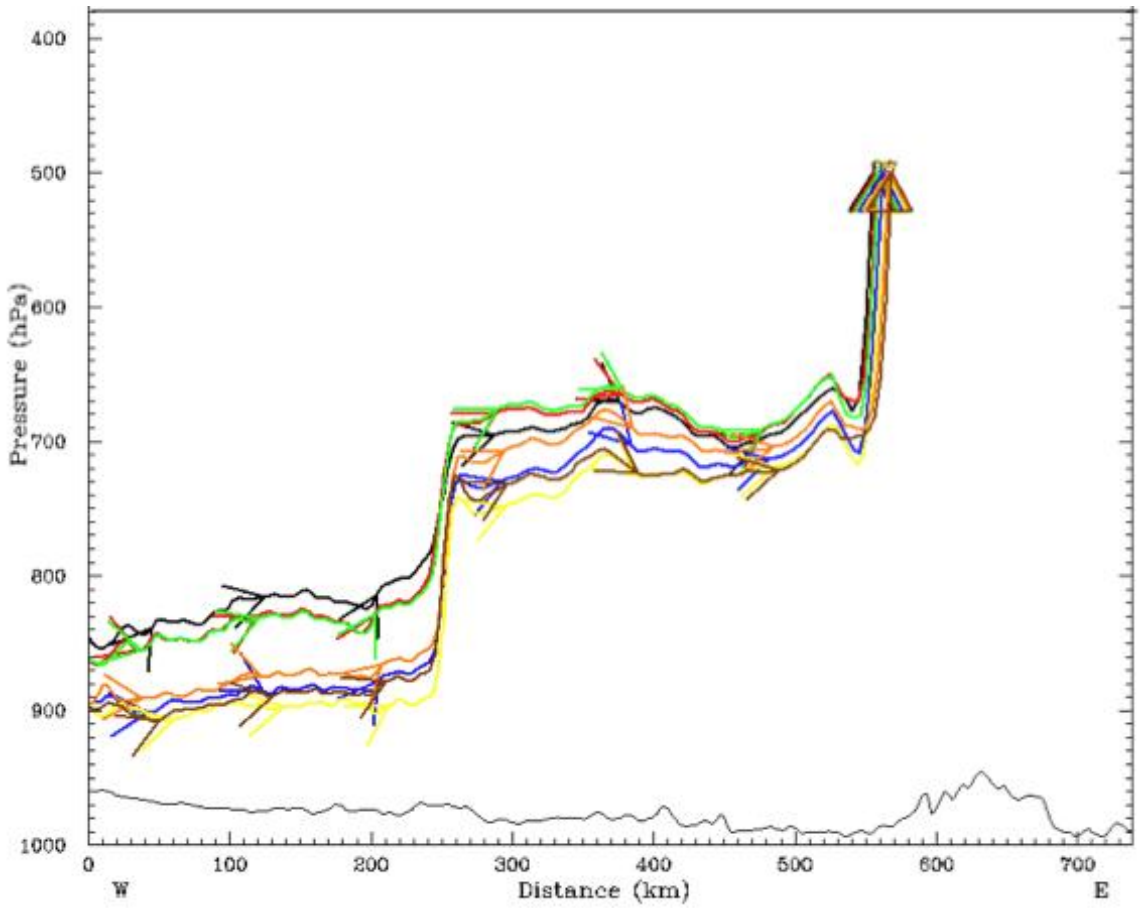


**Fig. 3.6.** Vertical backward trajectory from 08 May 2009 (1445 UTC). The x-axis represents distance, while the y-axis shows pressure decreasing upward. Arrows plotted along the trajectory path represent hourly increments.

Following analysis of trajectories, several other pressure-level plots can be studied to determine various environmental conditions leading up to initiation of convection within the arrow region, as well as for the duration of the arrow. These plots show the wind direction and speed, showing the entire flow around the system. This helps to determine where all air parcels in and around the system are originating, as well as whether any convergence is occurring. This can help to diagnose the cause of lifting, and the orientation of the convection. Additionally, temperature gradients are given on these plots. This indicates any temperature advection in and around the system, which may also be responsible for initiating lifting.

Finally, it is also important to determine the thermodynamic environment of the area prior to initiation of the arrow. Several factors will be considered through analysis of various thermodynamic plots. These plots will provide information regarding stability, which is a necessary ingredient for convection. Additionally, information will be provided regarding isentropic lifting, and whether the convection is occurring at an elevated level, above or behind the cold pool.

# 4. OBSERVATIONAL ANALYSIS

## 4.1 Synoptic and Mesoscale Analysis

Observational analysis is a good starting point for determining the environmental conditions in place prior to, and throughout the duration of each event. This provides a sense of the true environment and can be useful for studying both the synoptic scale and mesoscale environments. As mentioned in the Data and Methods section, upper-air observations and surface analysis from NOAA's HPC are examined. Although these plots are useful in examination of environmental conditions on the synoptic scale, they are relatively coarse, meaning data is sparse. In order to get a closer look at the mesoscale, surface analysis from the Barnes objective analysis method (Koch et al. 1983) is used for creating analyses that show sea-level pressure, temperature, and surface station observations, with an overlay of composite radar reflectivity. Four different cases are used for observational analysis. These cases include the three cases used in model simulation (discussed in the Introduction), as well as a case from 5 July 2003. Although the July 2003 case cannot be satisfactorily reproduced through model simulation (as is also found by Metz and Bosart 2010), it is used for observational discussion because it displays exemplary conditions for the interest of this study.

### *4.1.1 5 July 2003 Event*

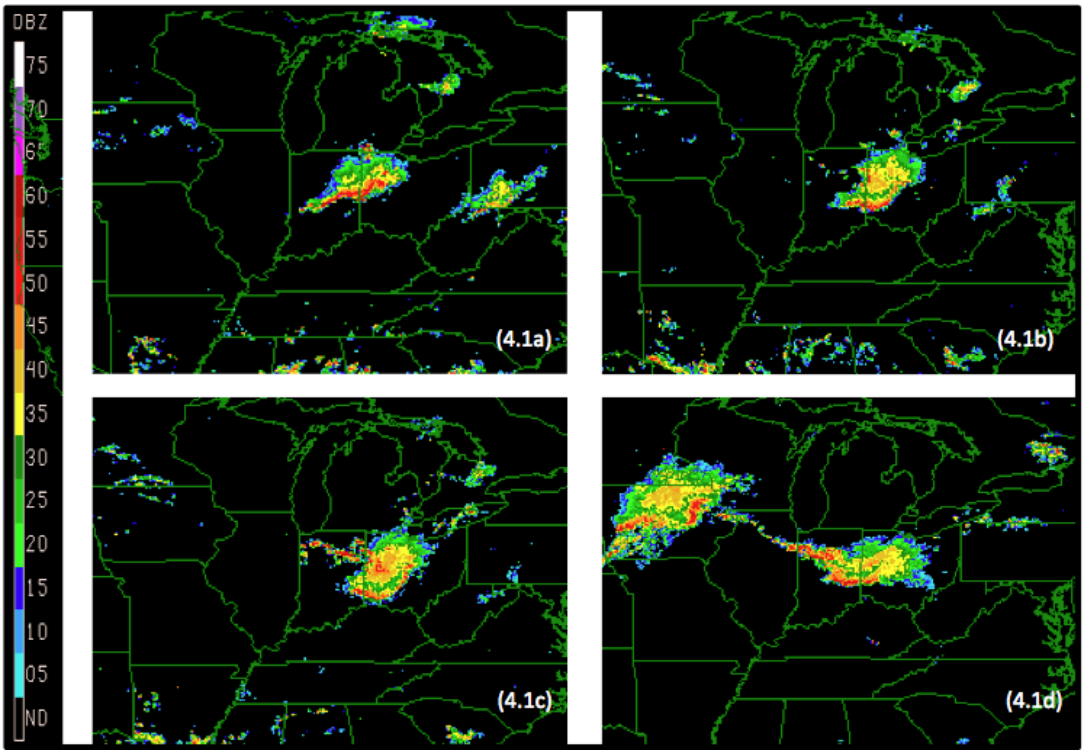


**Fig. 4.1:** Composite radar reflectivity progression from 5 July 2003. (a) 0000 UTC, (b) 0115 UTC, (c) 0200 UTC, (d) 0645 UTC. From NCAR's MMM Image Archive.

On the late afternoon of 4 July 2003, and into the early morning hours of 5 July, convection that began over northwest Illinois propagated eastward, eventually organizing into a well-structured MCS. The leading line of convection progressed into a bow echo formation over northeastern Indiana around 0000 UTC (Fig. 4.1a). Around 0115 UTC, as the bow moved toward the southeast, and into western Ohio, convective cells appeared in northwest Indiana (Fig. 4.1b). By 0200 UTC, an organized line of convective cells had formed an arrow in, and behind, the initial MCS (Fig. 4.1c). By 0645 UTC, the leading bow echo had lost organization, and the arrow region propagated eastward, forming the new leading line, and bow echo. At this time, more convection formed somewhat behind and to the west side of this bow. This is shown in Fig. 4.1d, which also includes another MCS over much of Iowa. The original bow and arrow system then remained stationary, while losing organization, as the second MCS swept through the area, merging with the original system, before they both (as one system) moved off toward the northeast.

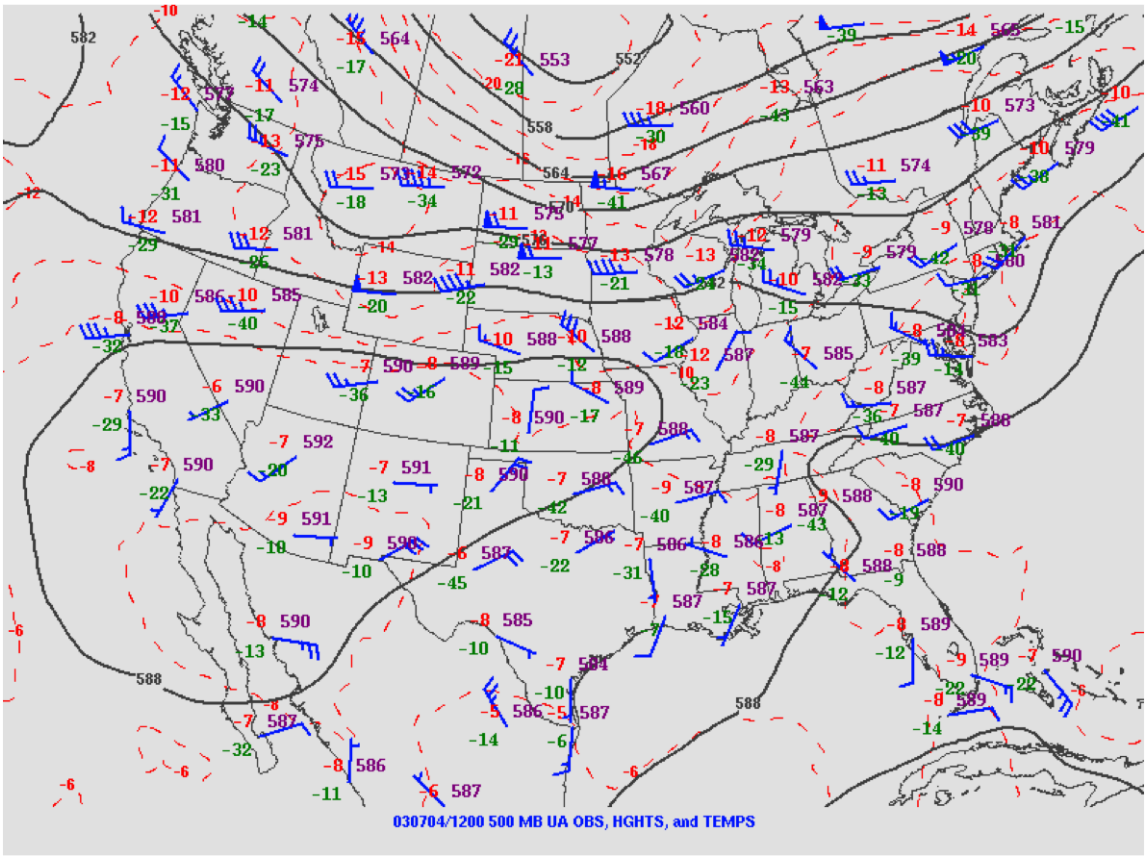


**Fig. 4.2.** 500-hPa analysis for 1200 UTC 4 July 2003, showing geopotential height (solid black contours every 3 decameters), temperature (dashed red contours every 2 degrees C). Upper-air station data is also shown, giving data for temperature (C), dewpoint (C), pressure (hPa), and wind direction and speed. From NOAA'S HPC.

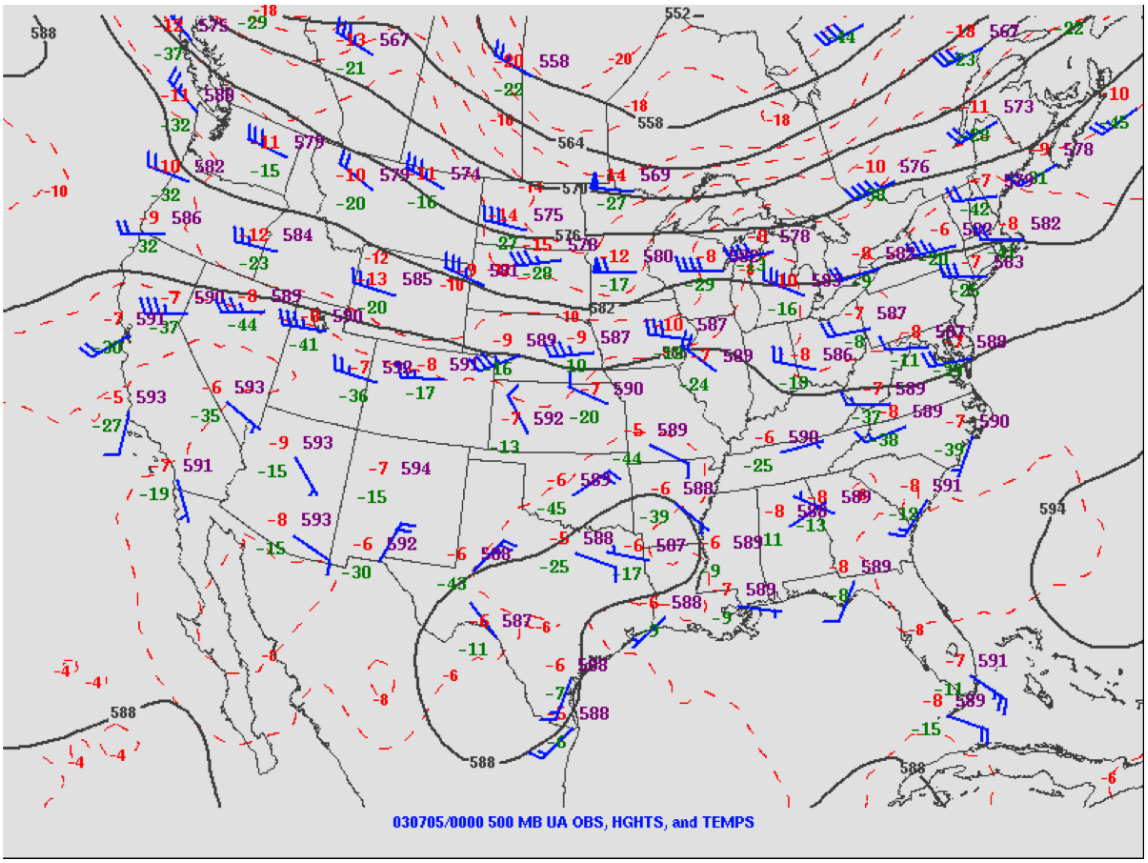


**Fig. 4.3.** As in Fig. 4.2, but for 0000 UTC 5 July 2003.

A 500-hPa ridge was located over much of the southwestern United States on 4 July (Fig. 4.2). Much of the northern part of the country was experiencing primarily zonal flow at the midlevels. A shallow trough is located over central Canada, while a short wave is evident over Idaho and Montana (Fig. 4.2). Comparing the analysis from 0000 UTC 5 July to the analysis 12 hours prior, it appears the short wave had progressed toward the east, causing a disturbance over the upper Midwest and Great Lakes regions (Fig. 4.3).

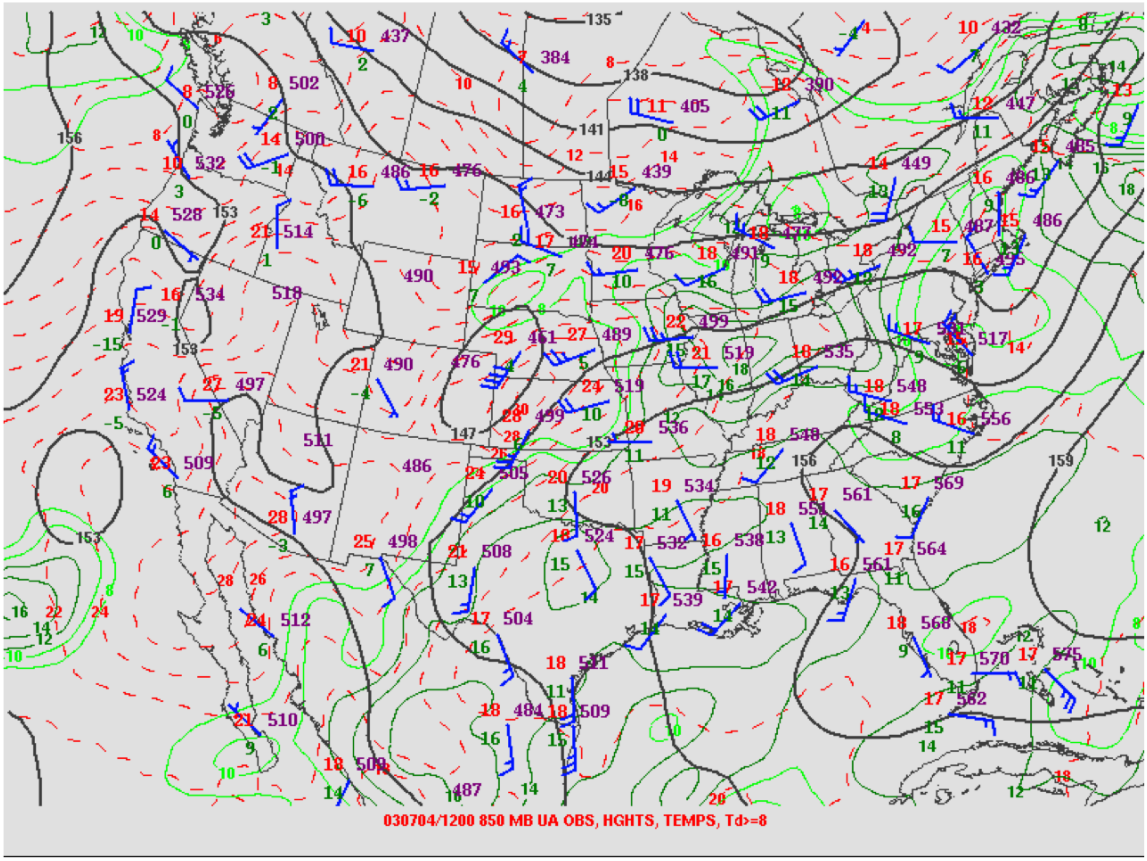


**Fig. 4.4.** As in Fig. 4.2, but 850-hPa level analysis. Additionally, dewpoint temperature ≥ 8 degrees C is shown (solid green contours).

850-hPa analyses for 1200 UTC 4 July (Fig. 4.4) and 0000 UTC 5 July (Fig. 4.5) show a nocturnal low-level wind maximum with wind speeds up to 20 m $s^{-1}$ flowing from the Gulf of Mexico (Gulf) into the central United States. The pattern of the jet essentially remains the same over the 12-hour time period, maintaining a southerly flow in from the Gulf, into the central United States, and then veering to become a southwesterly, then westerly flow over the upper Midwest region. This brings warmer, moist air into this region, creating a more-unstable environment.

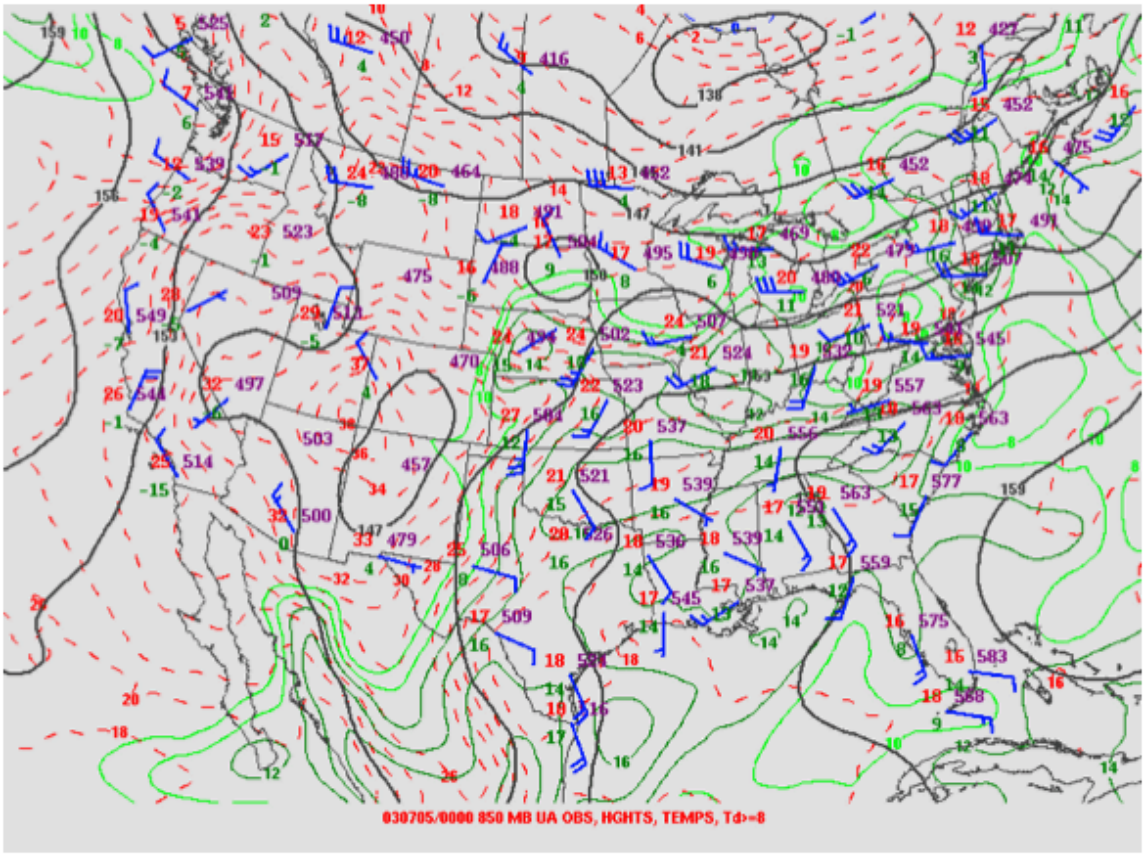


**Fig. 4.5.** As in Fig. 4.4, but for 0000 UTC 5 July 2003.

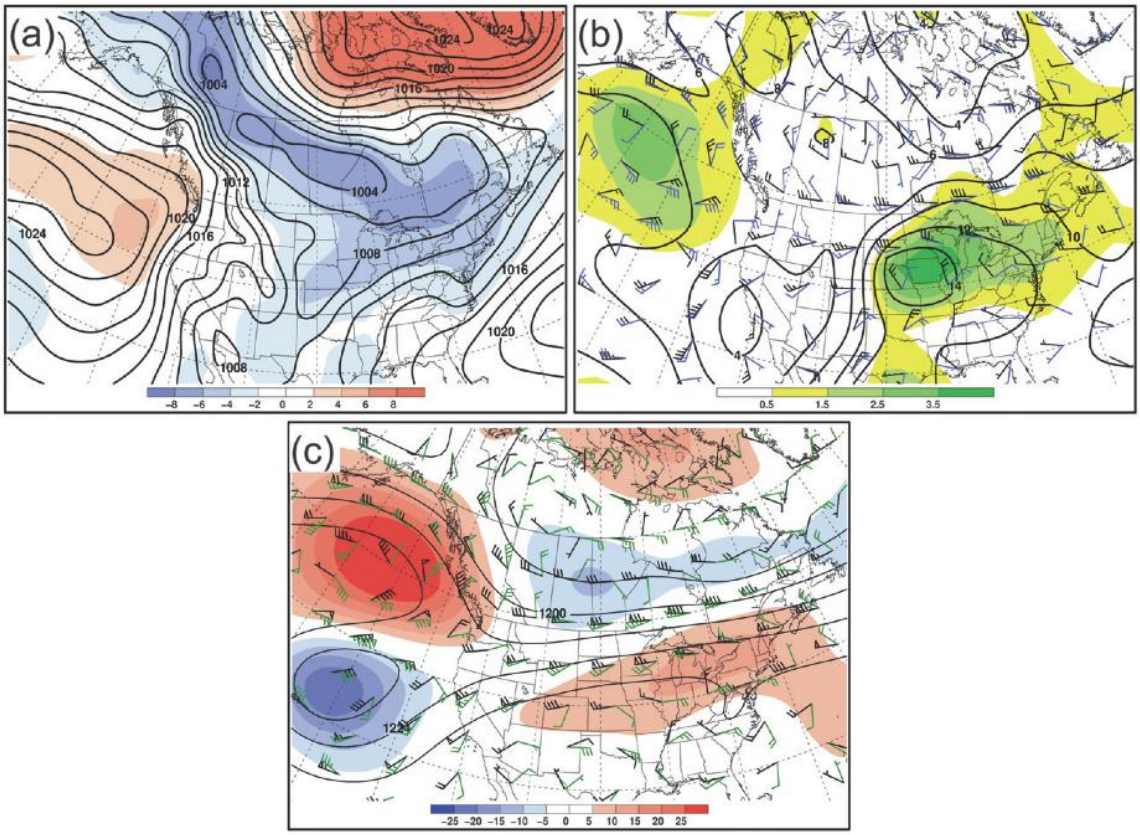


**Fig. 4.6.** Composite mean over 6 hourly analyses from 3 to 5 July 2003. (a) mean SLP (black lines every 2 hPa) and anomalous SLP (shaded in hPa); (b) mean 935-hPa mixing ratio (black lines every 2 g kg$^{-1}$), anomalous 925-hPa mixing ratio (shaded in g kg$^{-1}$), mean 0-6-km shear (black barbs in m s$^{-1}$), and anomalous 0-6-km shear (blue barbs in m s$^{-1}$ where one pennant is 25 m s$^{-1}$); and (c) mean 200-hPa geopotential heights (black lines every 12 dam), anomalous 200-hPa geopotential heights (shaded in dam), mean 200-hPa wind (black barbs in m s$^{-1}$ where one pennant is 25 m s$^{-1}$), and anomalous 200-hPa wind (green barbs in m s$^{-1}$ where one pennant is 25 m s$^{-1}$). (Source: 2.5° NCEP-NCAR reanalysis). From Metz and Bosart (2010).

Metz and Bosart (2010) conducted a study of the two MCSs, and the five derechos that were produced during the time period of 3-5 July 2003. They provided a synoptic overview, using three different time-mean analyses to show that the pattern was favorable for MCS development. Time-mean sea-level pressure (SLP) and anomalous SLP (Fig. 4.6a) shows a large trough to the east of the Rocky Mountains. Cyclonic flow is associated with this trough, in which negative SLP anomalies of 2-6 hPa extended toward the upper Midwest. Fig. 4.5b shows that mixing ratios in excess of 14 g $kg^{-1}$ were centered over Iowa, while anomalously high mixing ratios (1.5-3.5 g $kg^{-1}$ above normal) were found to extend from Kansas, into the northeast United States. These anomalously high mixing ratios also coincide with the region of anomalously low SLP. This is the area in which both MCS events occurred over this time period. Also illustrated (Fig. 4.6b) are anomalously high (5-10 m $s^{-1}$ above normal) 0-6-km shear values. 200-hPa-analysis (Fig. 4.6c) reveals a jet entrance region located along the western United States and Canadian border, which is the origin for much of the convection during this event. This jet stream core contained anomalously high-speed winds (up to 20 m $s^{-1}$ above normal) throughout the duration of the time-mean analysis.

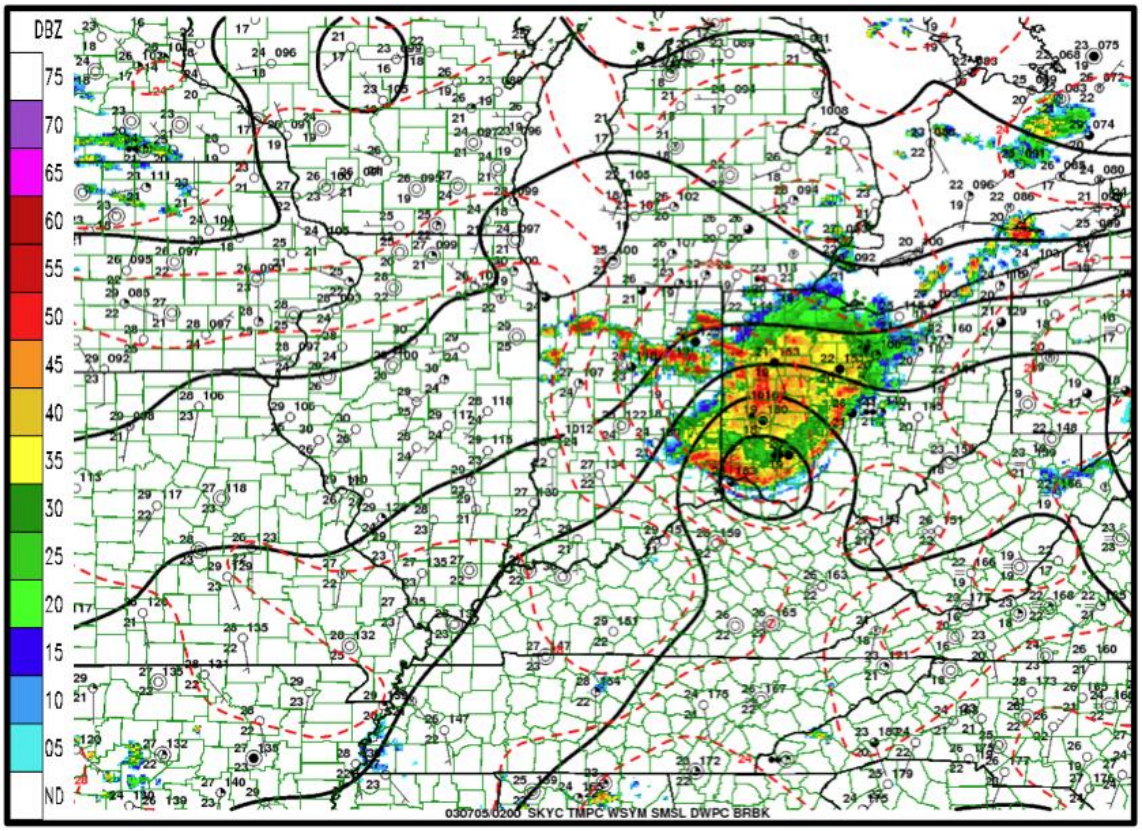


**Fig. 4.7.** Surface analysis for 0200 UTC 5 July 2003. Shows an overlay of composite radar reflectivity, mean SLP (solid black lines, every 2 hPa), temperature contours (dashed red lines every 2°C), and surface stations that show temperature (°C), dewpoint temperature (°C), pressure (hPa), and wind direction and speed (kts).

To try to obtain a better understanding of the mesoscale environment in which the bow and arrow occurred, surface analysis, with an overlay of composite radar reflectivity, are analyzed. The bow and arrow phenomenon occurred in two separate phases during this event (recall Figs. 4.1c and 4.1d). There was a prominent arrow evident around 0200 UTC, as well as 0700 UTC. Analysis for 0200 UTC (Fig. 4.7) displays a strong bow echo, located over western Ohio, while an organized arrow region was extending in a northwestern direction, from the cold

pool region in western Ohio, across Indiana, to the northeast Illinois border. Isobars reveal a meso-high (1018 hPa; Fujita 1955) located near the leading edge of the convective line. It appears that the area of high pressure actually crosses the leading edge into the area ahead of the bow; however, this is most likely due to the lack of surface observations, and the objective analysis method. The meso-high is assumably contained behind the leading edge, as has been previously exemplified (Hamilton, 1970) as a characteristic for bow echo environments. Isotherms reveal an intense cold pool region the bow echo, with temperature near 22°C. The temperature gradient is strong, as temperatures increase rapidly in directions outward from the cold pool. Wind barbs show that surface winds are southerly as they move toward northern Indiana, and toward the convective arrow region. Based on this analysis, because winds were moving in a direction parallel to the isotherms, and furthermore, the arrow develops perpendicular to the isotherms, it can be assumed that there, most likely, was no lifting associated with temperature advection, at the surface. Due to the fact that the resolution is coarse, however, this is not a definite conclusion.

By 0700 UTC, the original bow echo had lost organization and was replaced by the former convective arrow (Fig. 4.8). That arrow became the new bow echo, which was oriented from west to east. The new MCS had more of an asymmetrical appearance, with the strongest cells along its western side. The new arrow, at this time, was still located behind the cold pool, but extended back toward the west (less perpendicular to the bow). It stretched toward the northwest, from north-

central Indiana to north-central Illinois, meeting convection ahead of the upstream MCS, located over Iowa. Again, isobars indicate a meso-high still in place near the leading edge of the bow, while the temperature contours still show the cold pool. The wind direction is still southerly, and parallel to isotherms. Because the arrow is still oriented in the same direction and location in this phase, there is, again, no evident surface lifting due to temperature advection in northwest Indiana and northeast Illinois. At this time, however, there is convection that is parallel to isotherms in northwest Illinois.

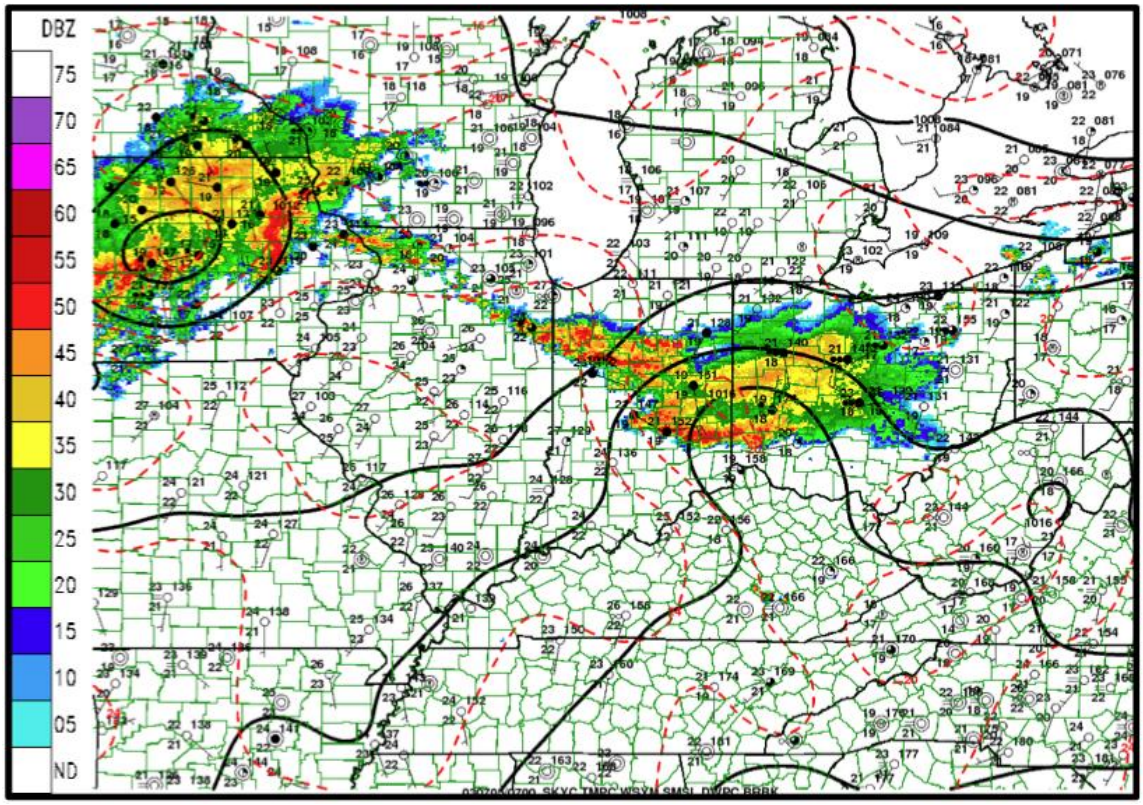


**Fig. 4.8.** As in Fig. 4.7, but at 0700 UTC.

From the observational analysis for this case, several aspects of the environment are identified that help to formulate hypotheses regarding explanation for the development and maintenance of the system, as a whole, from a synoptic standpoint. For the purpose of diagnosing the mesoscale environment, however, data is limited and the analysis that is available does not answer key questions regarding the mechanisms responsible for initiating and maintaining the convective arrow behind the bow echo, nor the reason for the orientation of the arrow. This is why it is necessary to perform numerical simulation to have the opportunity to examine the environment, using model output for detailed analysis. Unfortunately, although several attempts were made, the model was unable to recreate this event; however, the next three cases that will be discussed, had successful simulations, which made more in-depth mesoscale analysis possible.

### *4.1.2 18 June 2006 Event*

On the afternoon of 17 June 2006 (around 2000 UTC), as an MCS moved out of Texas, toward the east, another strong line of convection formed along the south-central Oklahoma and north-central Texas border (Fig. 4.9a). By 0300 UTC on 18 June, the convection had moved toward the south, into north-central Texas, organizing and forming a bow echo in north-central Texas (Fig. 4.9b). Around 0500, the first cells of the convective arrow appeared (Fig. 4.9c). Fig. 4.8d displays the arrow, fully organized at 0600 (Fig. 4.9d), before it lost organization by 0700.

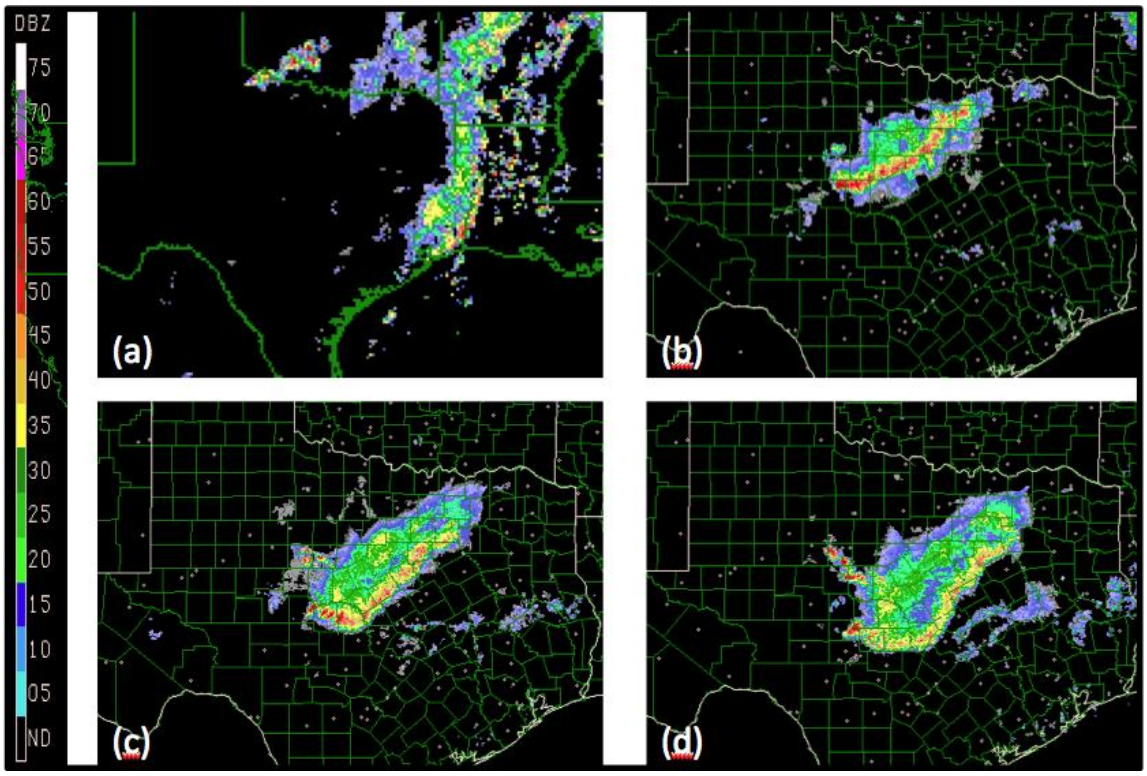


**Fig. 4.9.** Composite radar reflectivity progression from 17 June 2006 and 18 June 2006. (a) 2000 UTC, 17 June, (b) 0300 UTC 18 June, (c) 0500 UTC, (d) 0600 UTC. From NCAR's MMM Image Archive.

500-hPa-analysis from 1200 UTC 17 June 2006 (Fig. 4.10) reveals a low pressure center over central Canada. Cyclonic flow associated with a positively-tilted mid-level trough is located over eastern Colorado and northeastern New Mexico. Additionally, there appears to be a short wave located to the north of Washington. Fig. 4.11 is the same 500-hPa analysis as mentioned above, but at 0000 UTC 18 June 2006. Comparison of Figs. 4.10 and 4.11 shows progression of the upper level system over time. By 0000 UTC (18 June), the shortwave moved toward the east, and is helping the low (located over Canada) to dig southeastward toward the base of the main trough located over the central United States. This

trough had moved toward the east by 0000 UTC, and had taken a slight negative tilt. Due to the movement of the trough, winds in the area of interest for this case changed from south-southwesterly to westerly, at this level.

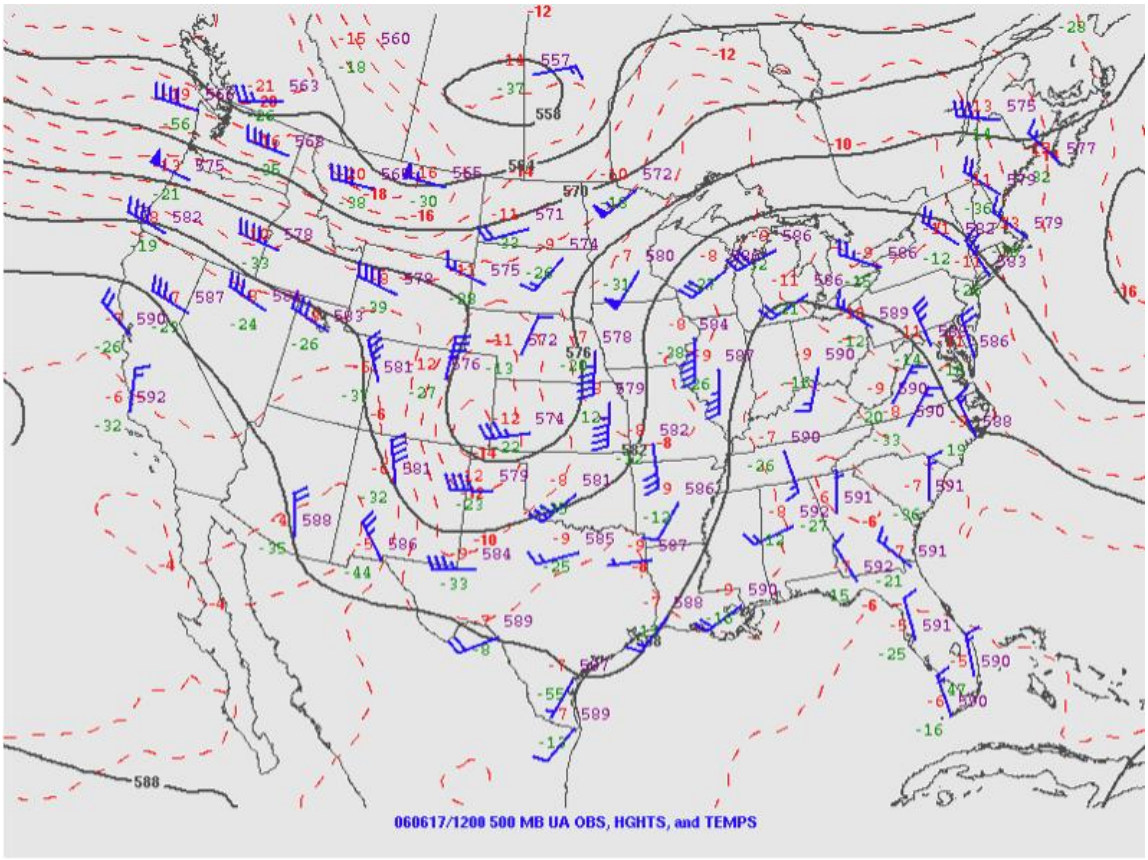


**Fig. 4.10.** As in Fig. 4.2, but analysis for 1200 UTC 17 June 2006.

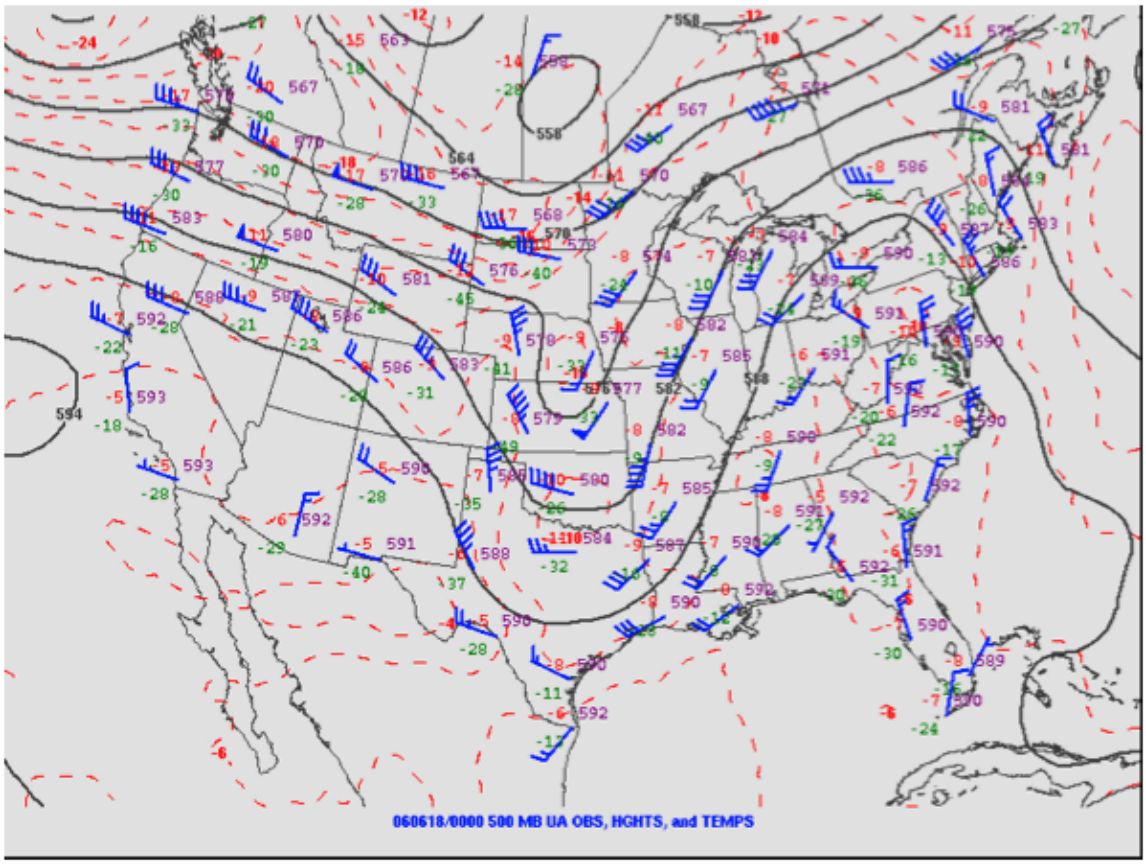


**Fig 4.11.** As in Fig. 4.2, but 0000 UTC 18 June 2006.

850-hPa-analysis from 0000 UTC 18 June (Fig. 4.12) portrays evidence of a strong (20 m $s^{-1}$) nocturnal low-level wind maximum to the east of the a mid-level trough. This means that conditions in the central United States (including Texas) were, most likely, becoming more unstable, due to strong winds advecting warmer, moist air from the Gulf, into these areas. This is confirmed by relatively high dewpoint temperatures.

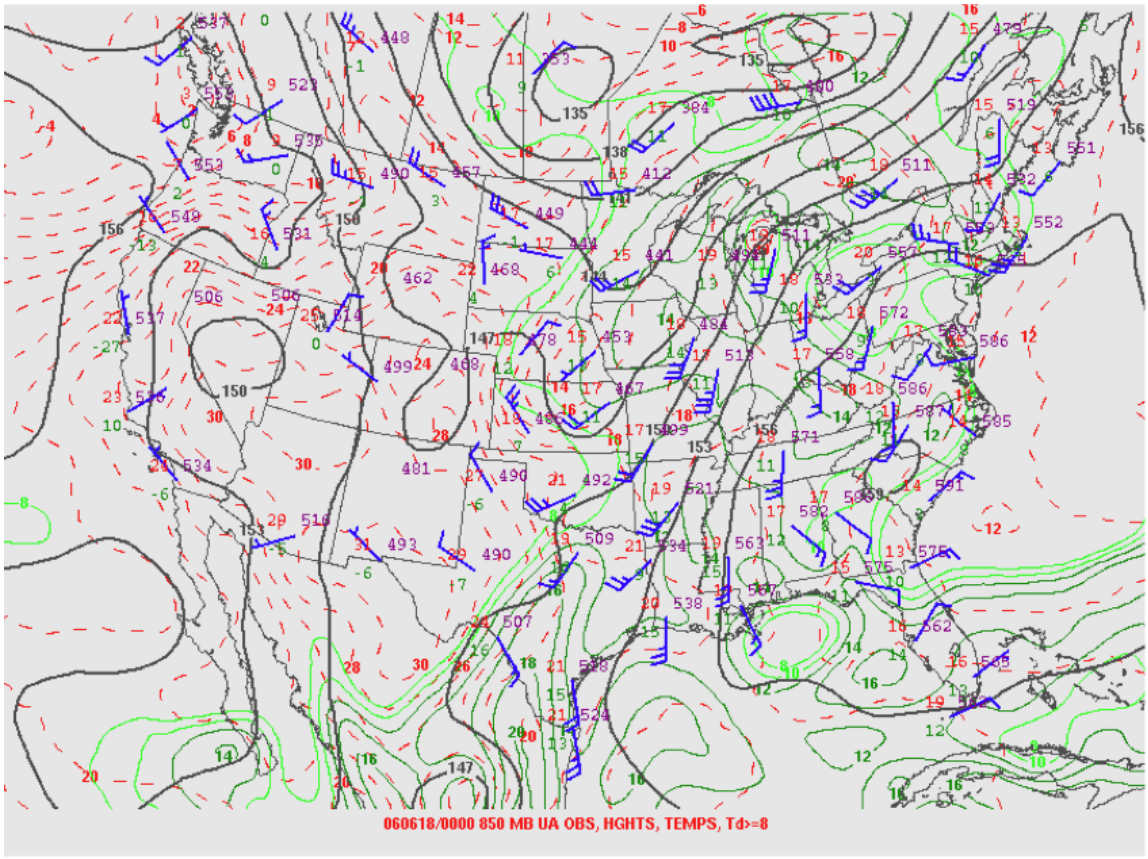


**Fig. 4.12.** As in Fig. 4.4, but analysis for 0000 UTC 18 June 2006.

Surface analysis from 0300 UTC is shown in Fig. 4.13. Recall, from Fig. 4.8b, that there was a strong convective bow in north-central Texas at this time. The surface plot shows a low-pressure area in west Texas, and another one in the southeast corner of Nebraska. A warm front extended from the low-pressure area in west Texas, through central Oklahoma, into central Kansas, where it connected to a small cold front attached to the surface low in Nebraska. A dryline was evident south of the low-pressure in west Texas, and an outflow boundary is displayed in the location in which the bow echo was located. Surface winds were southerly,

bringing warm, moist air into Texas, off of the Gulf. Temperatures were in the lower 80's (degrees Fahrenheit (F)), while dewpoint temperatures were in the 70's (F). The temperature and dewpoint temperature taken at the MAF (Midland, TX) station (located in west-central Texas), however, were 66 and 64 F, respectively, which is expected, as the cold pool behind the bow echo was located in that general area.

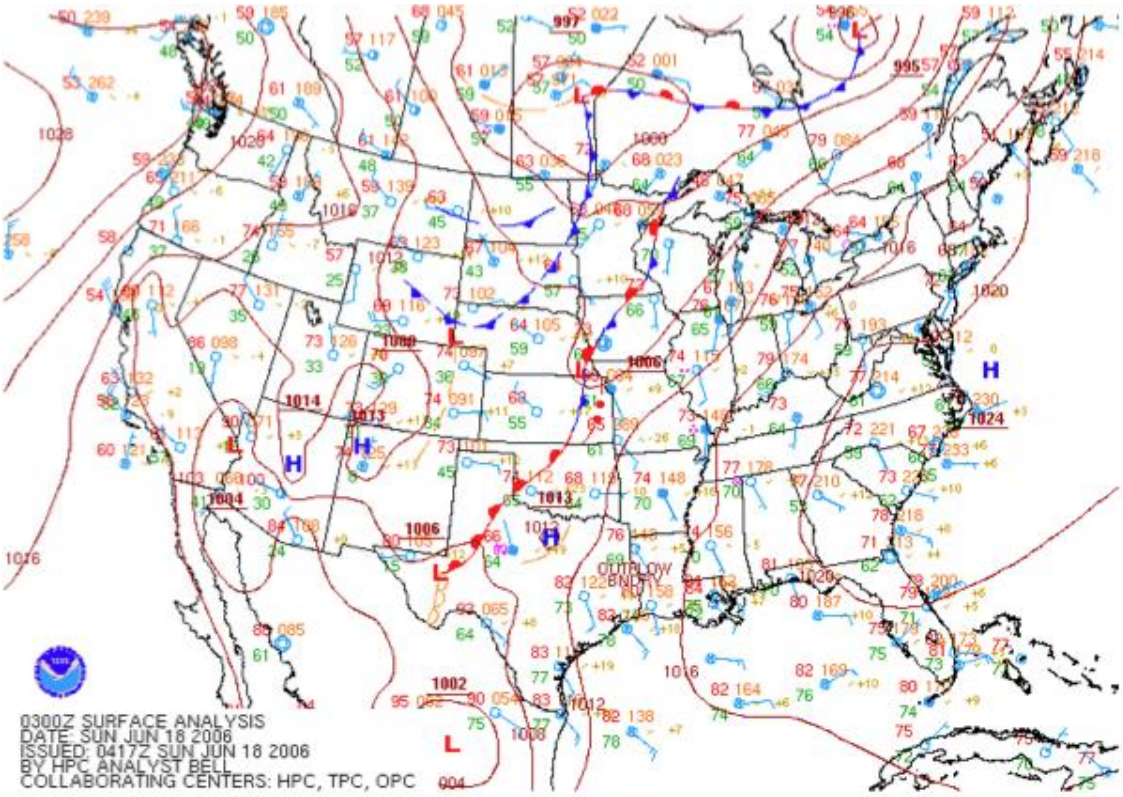


**Fig. 4.13.** Surface analysis from 0300 UTC 18 June 2006. Shows pressure (solid dark brown contours every 4 hPa), areas of high pressure (blue H), areas of low pressure (red L), and frontal boundaries (red for warm, blue for cold). Surface station data is also shown, giving data for temperature (F), dewpoint (F), pressure (hPa), wind direction and speed, and cloud cover information. From NOAA's HPC.

According to the Storm Prediction Center's Archived Convective Outlook for this particular day, a slight risk was predicted for the area. They gave a 30 percent chance for large hail (≥ 1 inch) and severe winds (gusts ≥ 50 knots) within 25 miles of the area around where the bow echo developed. Their discussion states that mid-level lapse rates were relatively steep, and that the mixed layer CAPE was between 2000 and 3000 J $kg^{-1}$, which is moderately unstable (SPC 2011). Additionally, convective inhibition was substantially low in the area (with a value of -185 J $kg^{-1}$ at the MAP Midland station at 1200 UTC). These conditions, in conjunction with the high temperatures and dewpoints, can collaborate to create an unstable environment in which any type of lifting mechanism would be quick to create convection.

Based on the synoptic-scale observational analysis, it seems that several criteria for producing deep convection were met. A large area of divergence at upper levels (not shown) was associated with lower-level convergence over north central Texas at 0000 UTC, 18 June. A short wave disturbance is evident at midlevels, while a strong LLJ was advecting warm, moist air into the area, causing dewpoint depressions to be low, and increasing instability. Finally, there was a prominent dryline at the surface just west of the area in which convection was initiated and maintained.

Fig. 4.14 shows surface analysis for 0600 UTC 18 June. The duration of the actual convective arrow is only a couple of hours for this case; therefore, only one hour is shown, and should be representative of the full time period for this event.

At this time, radar reflectivity shows a mature bow echo, with a well-organized convective arrow region behind and perpendicular to the bow (in and behind the cold pool region). Temperature gradients were tight in and around the entire system, with warm air surrounding the cold pool. The coolest temperature contour (20°C) is located behind the bow echo. This is indicative of the cold pool. Overall pressure was decreasing from east to west, but there was an obvious meso-low (1010 hPa) located near the wake of the cold pool (Johnson and Hamilton 1988). Wind direction near the convective arrow was southeasterly, moving out from the outflow region.

Based on observational analysis, there are no obvious implications for the rationale behind convection initiation or orientation in the arrow region of the system. Similar to the previous case, the arrow does not form along the surface outflow boundary, or any other apparent surface boundary. Again, this is why model simulation is useful for deeper analysis. Fortunately, this case was able to be reproduced, and examination of the model output analysis will be discussed in section 5.1.

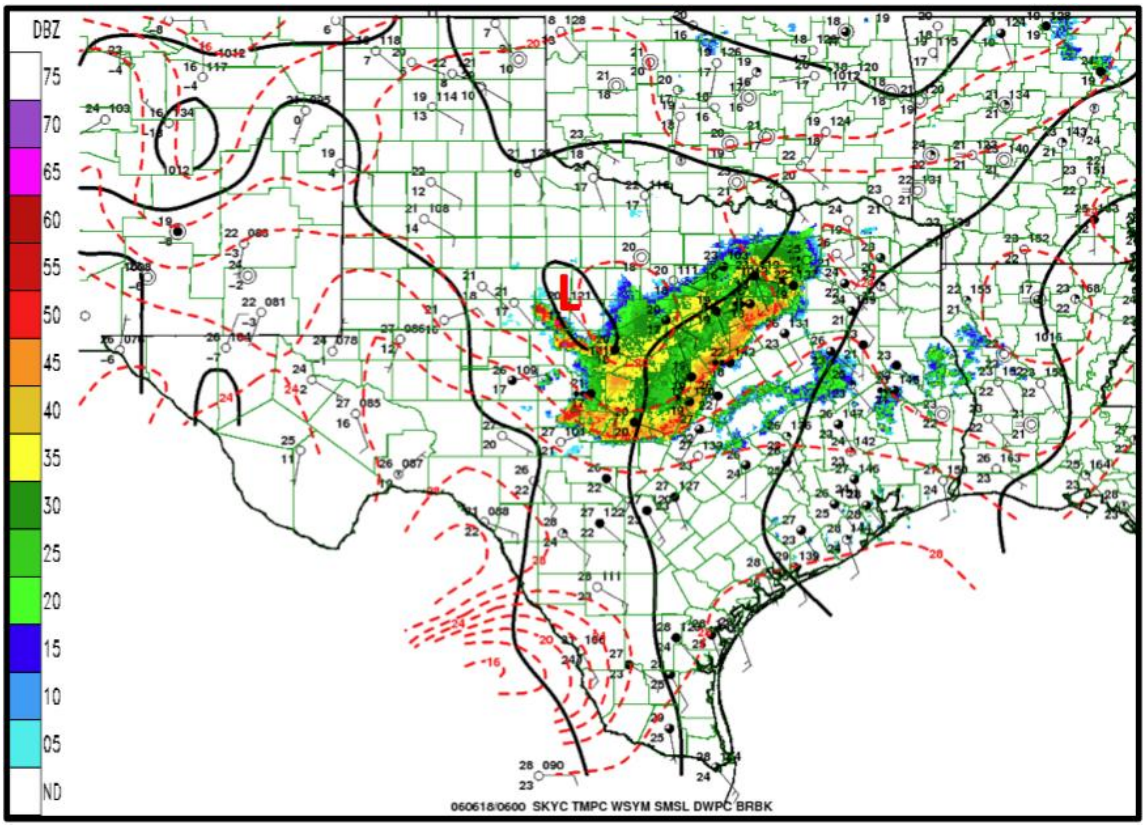


**Fig. 4.14.** As in Fig. 4.7, but 0600 UTC 18 June 2006.

### *4.1.3 08 May 2009 Event*

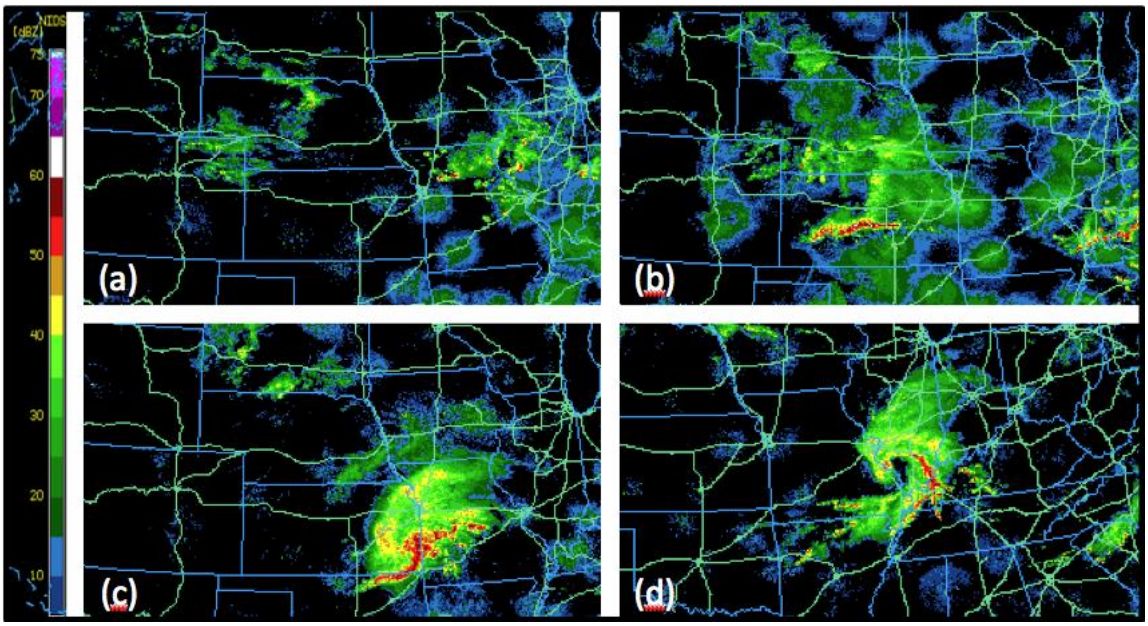


**Fig. 4.15.** Composite radar reflectivity progression from 08 May 2009. (a) 0154 UTC, (b) 0754 UTC, (c) 1155 UTC, (d) 1725 UTC. From NCAR's MMM Image Archive.

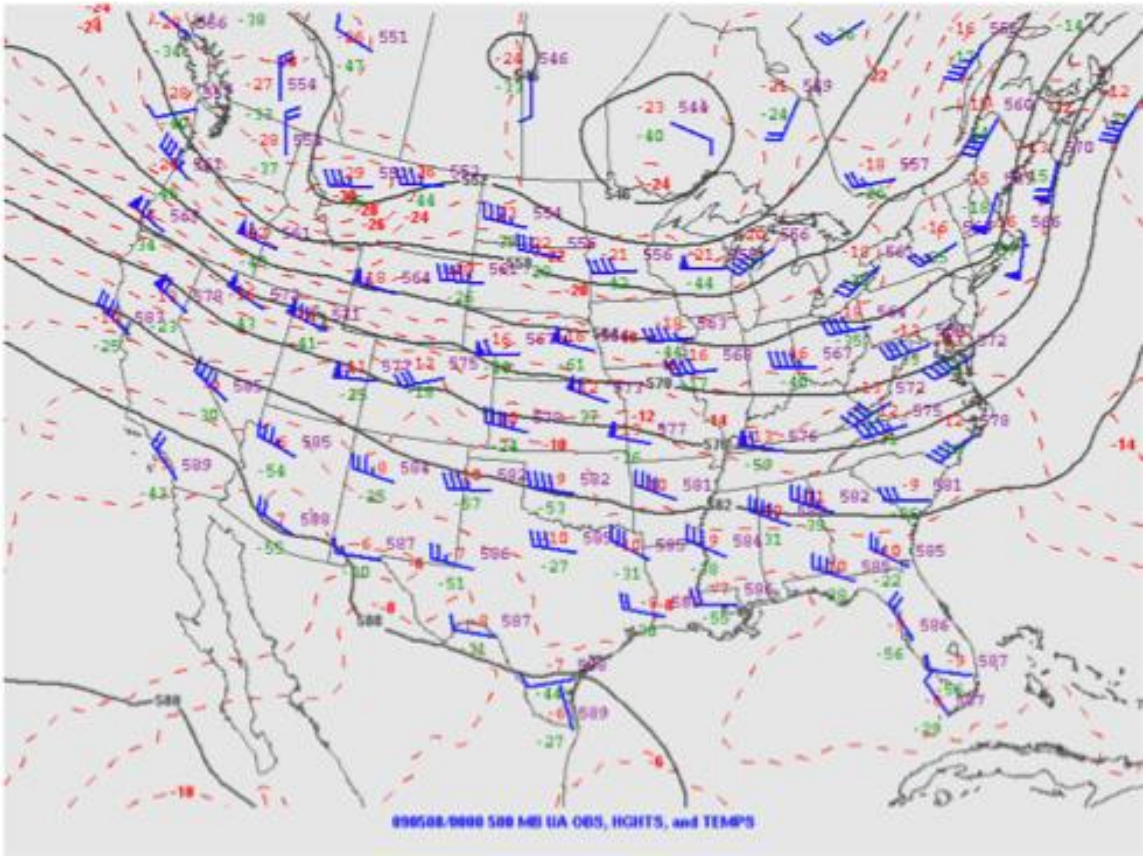

**Fig. 4.16.** As in Fig. 4.2, but 0000 UTC 08 May 2009.

Near 0154 UTC 08 May 2009, scattered weak convection began to form over northeastern Colorado (Fig. 4.15a). Over the next several hours, the system propagated toward the southeast, and began to slowly organize. By 0754 UTC, an organized line of convection had gathered over central Kansas (Fig. 4.15b). By 1155 UTC the leading line of convection had become progressed into a strong bow echo, near the border between southeastern Kansas and central Missouri, extending into northeastern Oklahoma (Fig. 4.15c). Around 1527 UTC, convection began to form behind the bow echo, in the cold pool region (not shown). As it swept through

southern Missouri and northern Arkansas, toward the east, it continued to organize, and by 1725 UTC had formed a fairly organized arrow region (Fig. 4.15d).

A fairly zonal flow pattern is evident over much of the country at both 0000 UTC and 1200 UTC 08 May (Figs. 4.16 and 4.17). A mid-level short wave, however, is evident over Montana at 0000 UTC. By 1200 UTC the short wave had intensified and began to dig southeastward, toward the north-central Rocky Mountain region.

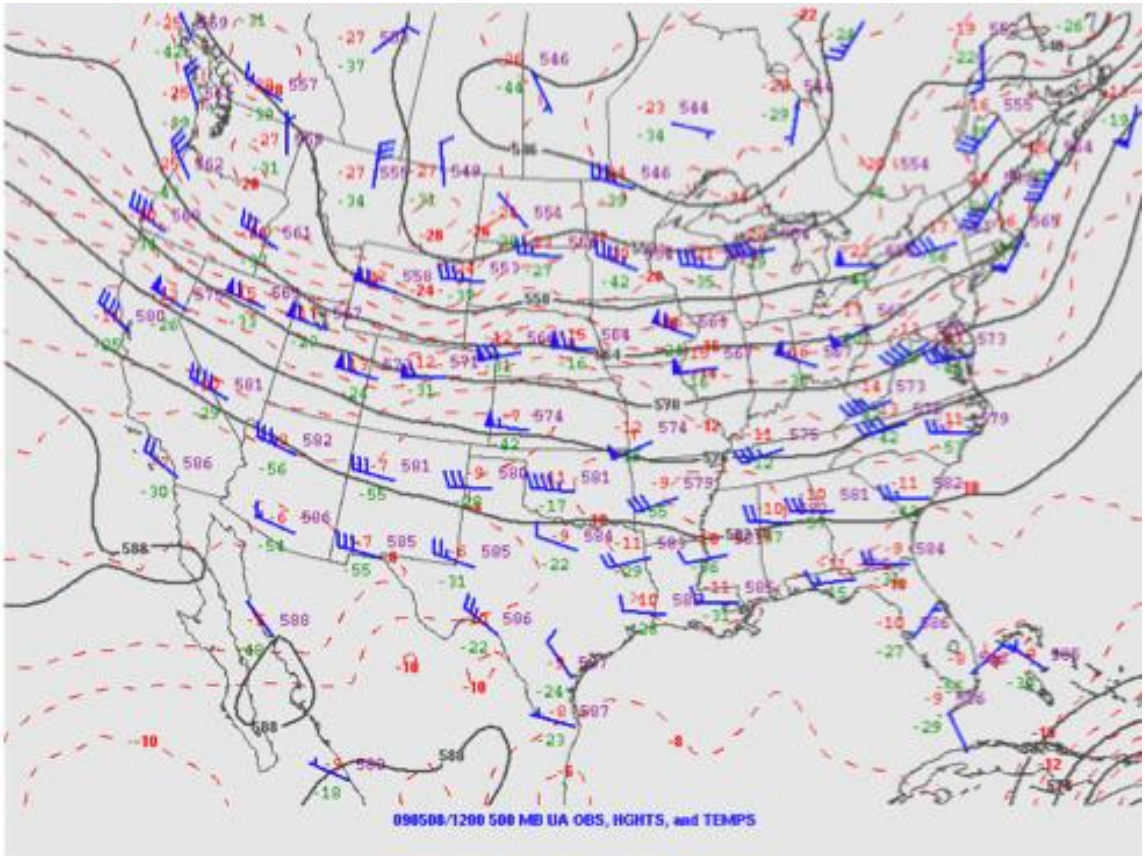


**Fig. 4.17.** As in Fig. 4.2, but 1200 UTC 08 May 2009.

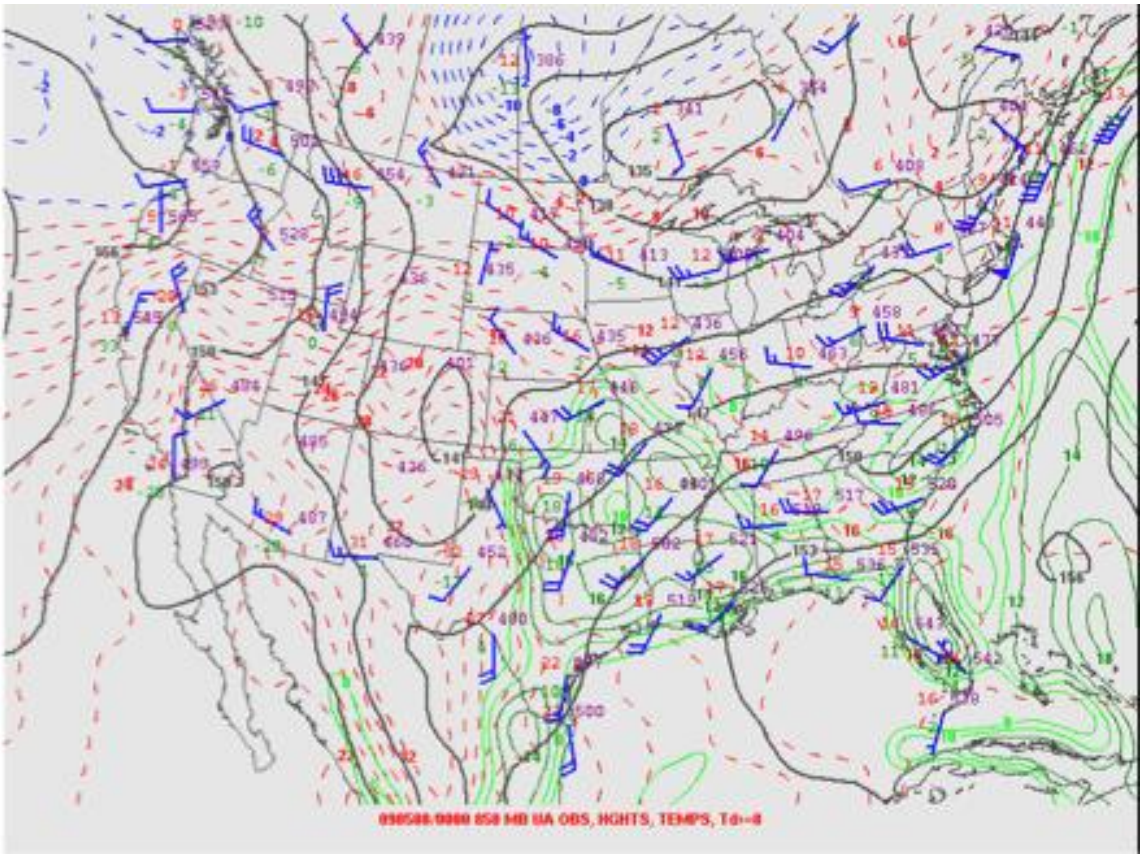

**Fig. 4.18.** As in Fig. 4.4, but 0000 UTC 08 May 2009.

The 850-hPa analyses for these same times (Figs. 4.18 and 4.19) indicate a strengthening low-level jet, as the wind across the southern plains essentially doubles in speed (from 20 knots to 40 knots). The LLJ begins to veer from a southerly flow to a southwesterly flow over the 12-hour period. Warm, moist air from the Gulf is being advected into the southern plains, further destabilizing the environment.

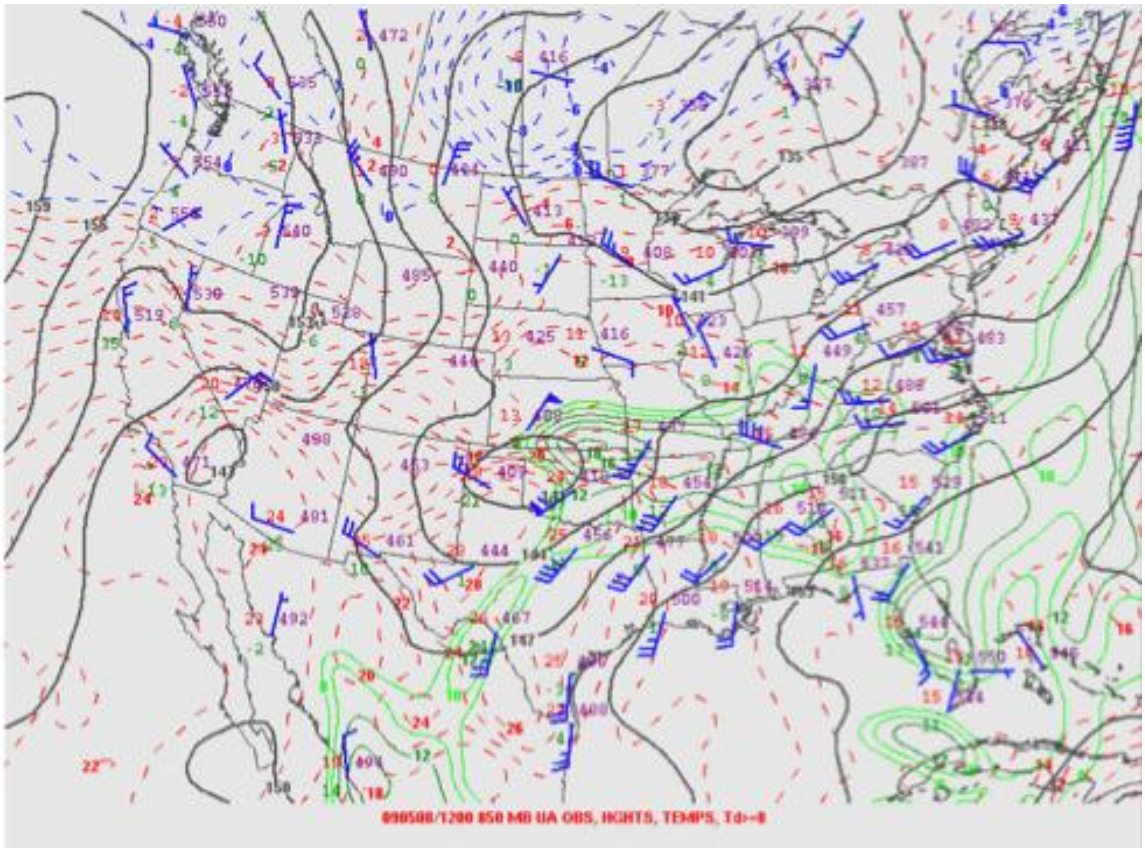


**Fig. 4.19.** As in Fig. 4.4, but 1200 UTC 08 May 2009.

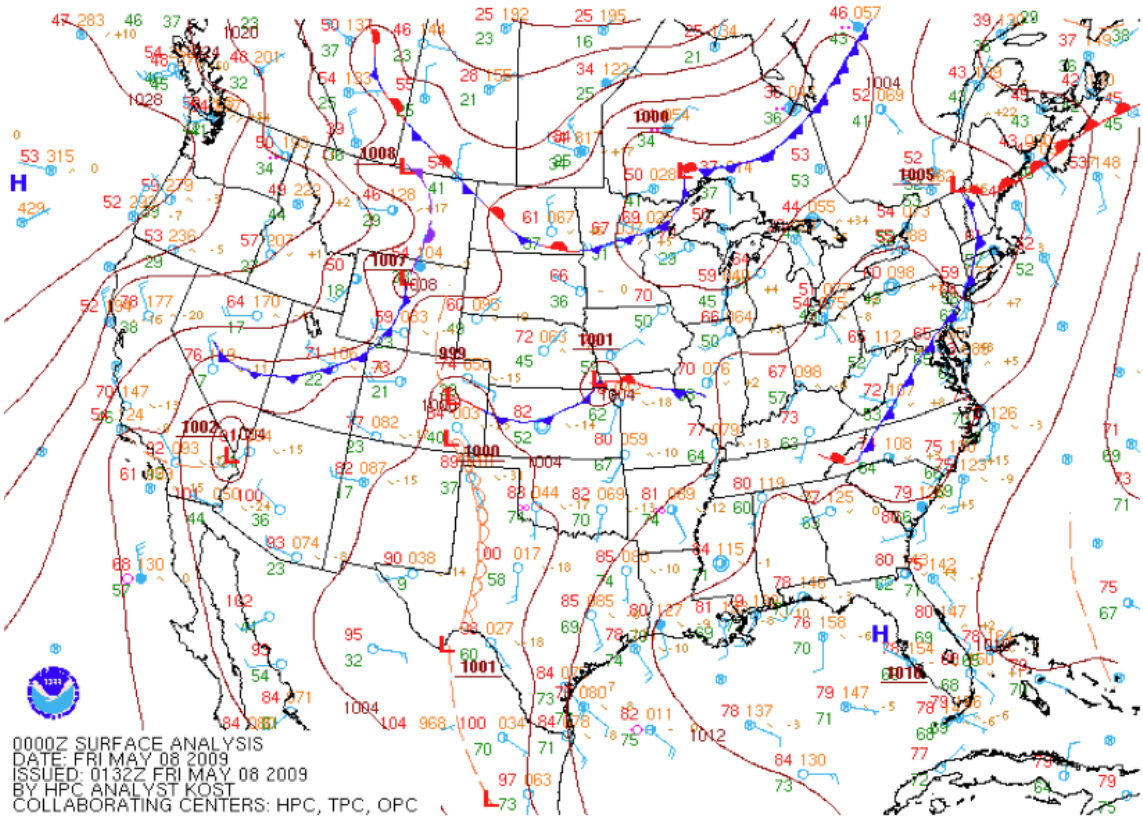


**Fig. 4.20.** As in Fig. 4.13, but 0000 UTC 08 May 2009.

Surface analyses for the same time periods (Figs 4.20 and 4.21) reveal a surface low that moves eastward from north-central Wyoming, into central Nebraska, along with a cold front that progresses eastward. At 0000 UTC, two other areas of low pressure are located in east-central and southeastern Colorado, with a dryline associated with the southern low. Additionally an area of low pressure is located near the intersection of the Kansas, Nebraska, and Missouri borders. By 1200 UTC, these lows have been forced (possibly by propagation of the upstream cold air mass) toward the southeast, into western and north-central Oklahoma, and southeast Illinois, forming a stationary frontal boundary that

extended between them. South of this front, winds were coming out of the south, from the Gulf, bringing the warmer, moist air with them. By the end of the period, temperatures in the southern plains were in the middle-to-upper 70's (F), while dewpoint temperatures were in the upper 60's (F), indicating high humidity in the area.

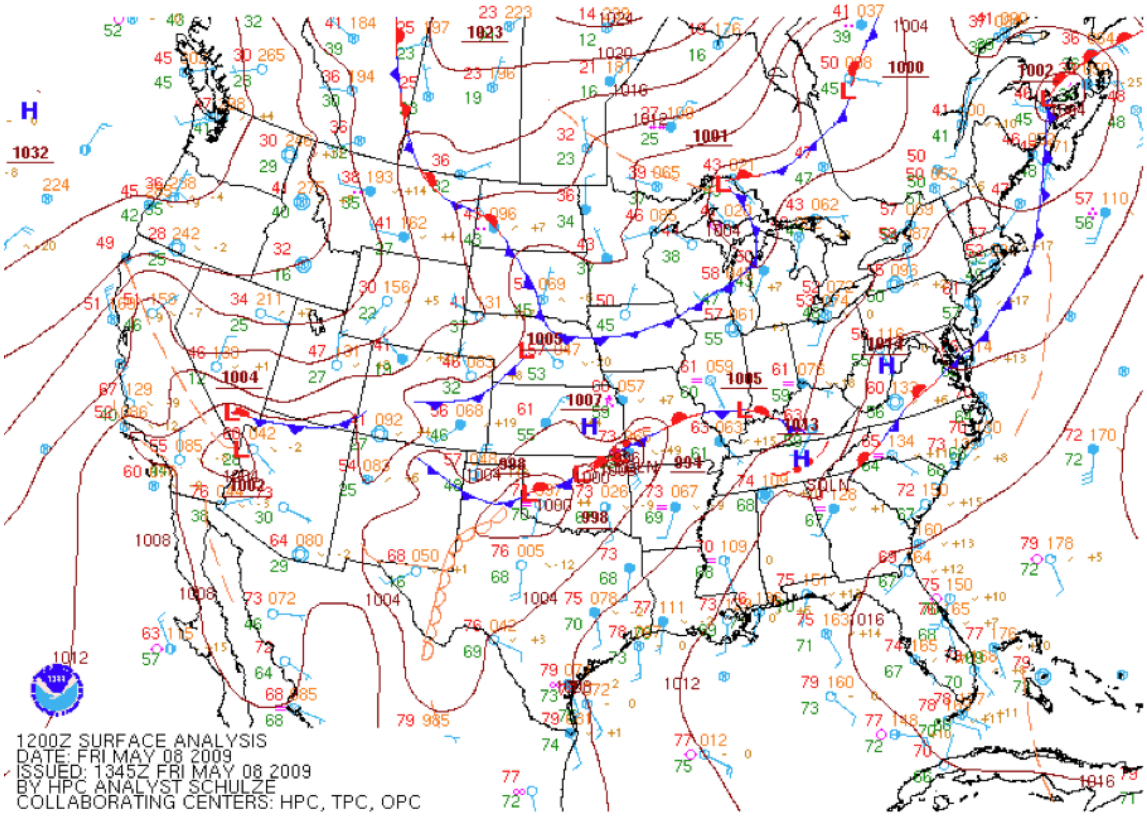


**Fig. 4.21.** As in Fig. 4.13, but 1200 UTC 08 May 2009.

The synoptic overview provides indication that several necessary ingredients for severe weather were available during this time period. The 300-hPa-analysis (not shown) shows strong upper-level divergence in the vicinity of a

strong jet stream. A mid-level shortwave trough was evident, and began digging deeper, creating more of a disturbance, over time. At lower levels, there was a strengthening LLJ, bringing warm, moist air into the area, providing an unstable environment for which a convective system can be maintained. At the surface, there were high temperatures and dewpoint temperatures, indicating high levels of moisture in the environment.

Coniglio et al. (2011) conducted a study of the large-scale system that produced the severe bow echo on this day. Their study focused on the environment and evolution of the convective system that caused what is commonly referred to now as the "Super Derecho." They state that they are unsure as to why the convection, coming from northeast Colorado intensifies, but there is evidence that the environmental conditions were quickly becoming more conducive for strong convection. They indicate that the instability was fairly low at 0300 UTC 07 May (prior to the development of the MCS), but that there was strong westerly flow aloft that created a significant amount of vertical wind shear. This would support strong, organized thunderstorm development.

Composite radar reflectivity data is unavailable for this event, and therefore, the entire convective system is not seen on this analysis. Radar reflectivity from the Springfield, Missouri radar site is used since it displays the arrow region of the storm, which is the interest for this study. The chosen time for the surface analysis (Fig. 4.22) is 1600 UTC. At this time, the bow echo had a south-to-north orientation, as the entire system was moving from west to east. Although reflectivity for the

arrow region was fairly low, as compared to other events, there was still an evident arrow located behind (and perpendicular to) the bow echo. There is an additional area of perpendicular (to the bow) area of convection that is located along the outflow boundary (in northern Arkansas). The only one of interest for this study, however, is the one farther north, in southern Missouri, because it is not along the outflow boundary (or any other obvious boundary). A distinct meso-low (1004 hPa) was located near the wake of cold pool region. Temperature contours show temperatures decreasing toward the middle of the system, with the coldest contour (16°C) located just behind the bow echo, in the cold pool region. Unfortunately, there is a lack of surface observations in and around the outflow of the system and, therefore it is difficult to determine wind direction near the arrow region.

Once again, the analysis clearly illustrates common patterns for MCSs and bow echoes, but does not provide any possible explanation for the existence of the convective arrow. This case is also recreated in model simulation, so that more definitive examination can be conducted. The results of that analysis will be discussed later, in section 5.2.

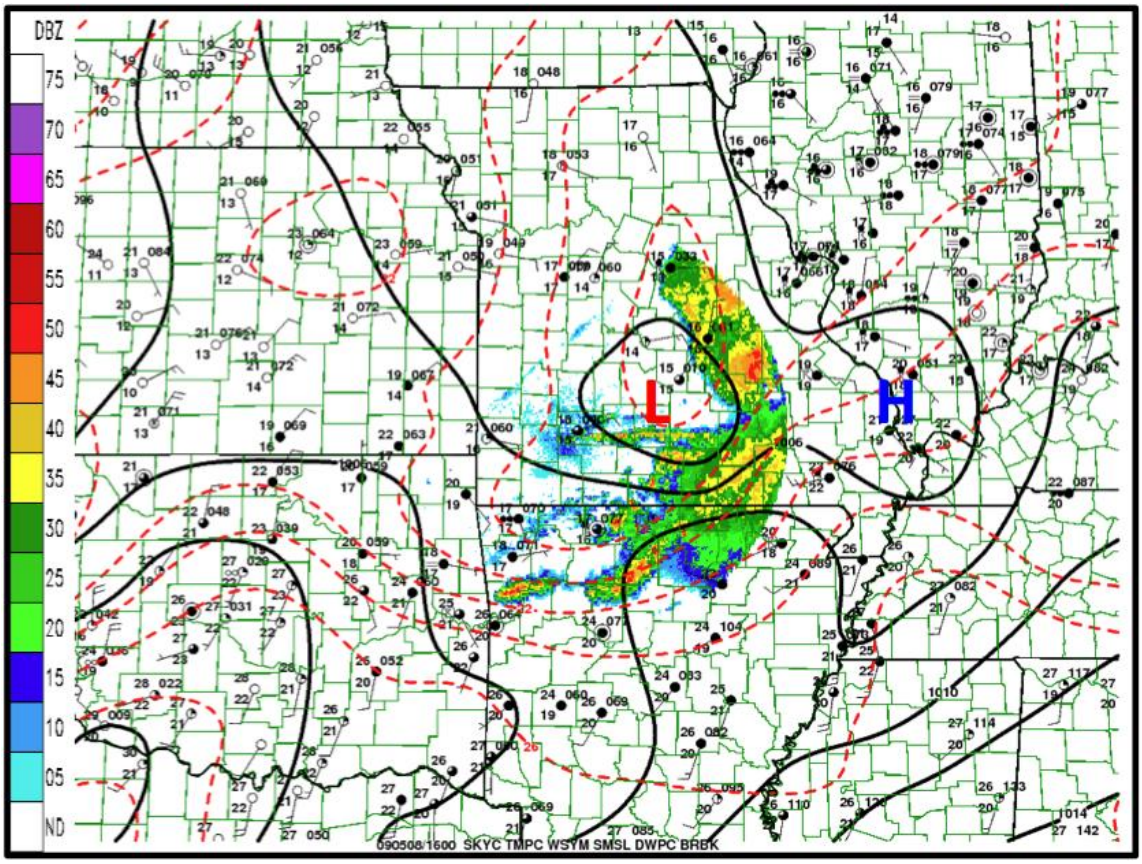


**Fig. 4.22.** As in Fig. 4.7, but 1600 UTC 08 May 2009.

### *4.1.4 15 September 2010 Event*

Around 2200 UTC 14 September, a small area of convective cells was evident, as seen on radar reflectivity over northeast Colorado. By 0330 UTC 15 September, the system had moved toward the east, into the very northwest corner of Kansas, and had strengthened, becoming more organized into a convective line. At this point the first convective arrow was evident on radar reflectivity, and strengthened by 0355 UTC (Fig. 4.23a). By 0430 UTC, the organized line began to appear bowed. By 0625 UTC, the arrow was still clearly evident on radar, and

extended in a southeast to northwest orientation behind the bow, into southwest Nebraska (Fig. 4.23b). The entire system continued to propagate toward the east-southeast over the next several hours. The bow strengthened while the arrow was maintained, until the system lost organization around 1000 UTC.

At 1257 UTC the system reorganized in northeast Kansas, and formed another well-defined convective arrow (Fig. 4.23c). Over the next few hours, the bow strengthened, moving toward the south into east-central Kansas, and finally dissipated by 1630 UTC. By this time, the lingering arrow had rotated to have a west-to-east orientation, and became the replacement bow, with a new arrow behind it. This new system strengthened, maintaining the arrow, and moved into central Missouri (Fig. 4.23d), before losing organization around 2230 UTC.

300-hPa-analysis for 0000 UTC 15 September (just after the convection began over northeast Colorado) shows a jet streak located in this general area, over the Colorado-Wyoming border (Fig. 4.24). The LBF sounding indicates wind speed at this level is $\geq$ 75 knots. Upper-level divergence is also evident in this area, meaning there was lower-level convergence, and upward motion.

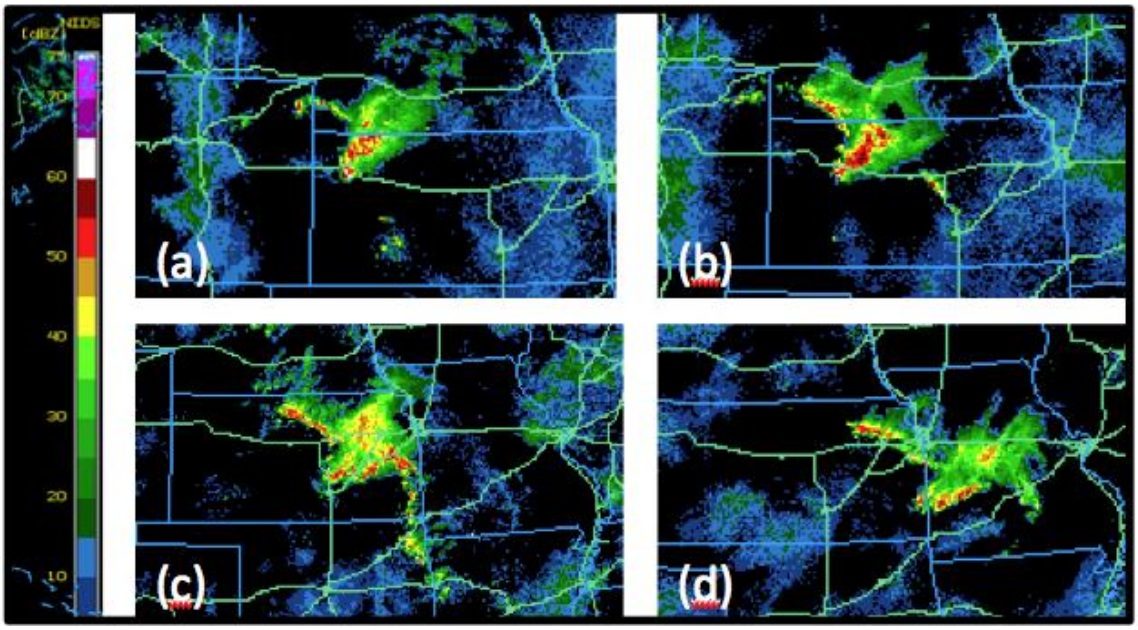


**Fig. 4.23.** Composite radar reflectivity progression from 15 September 2010. (a) 0355 UTC, (b) 0625 UTC, (c) 1257 UTC, (d) 1926 UTC. From NCAR's MMM Image Archive.

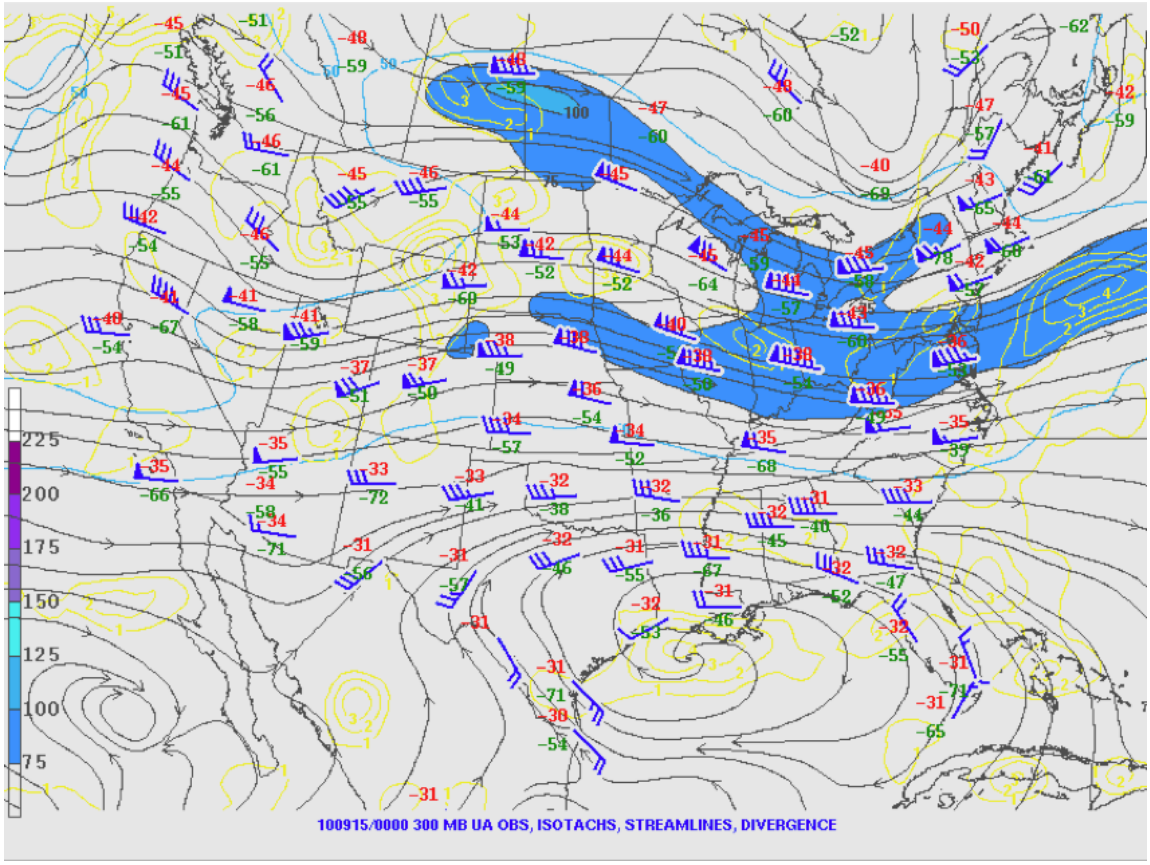


**Fig. 4.24.** 300-hPa analysis for 0000 UTC on 15 September 2010. Shows wind speed (shaded blue contours every 25 knots), streamlines (solid black lines with arrows showing direction), divergence (solid yellow contours with a contour interval of 1 $s^{-1}$), and upper-air observations, which include temperature, dewpoint temperature, and wind speed and direction. From NOAA's HPC.

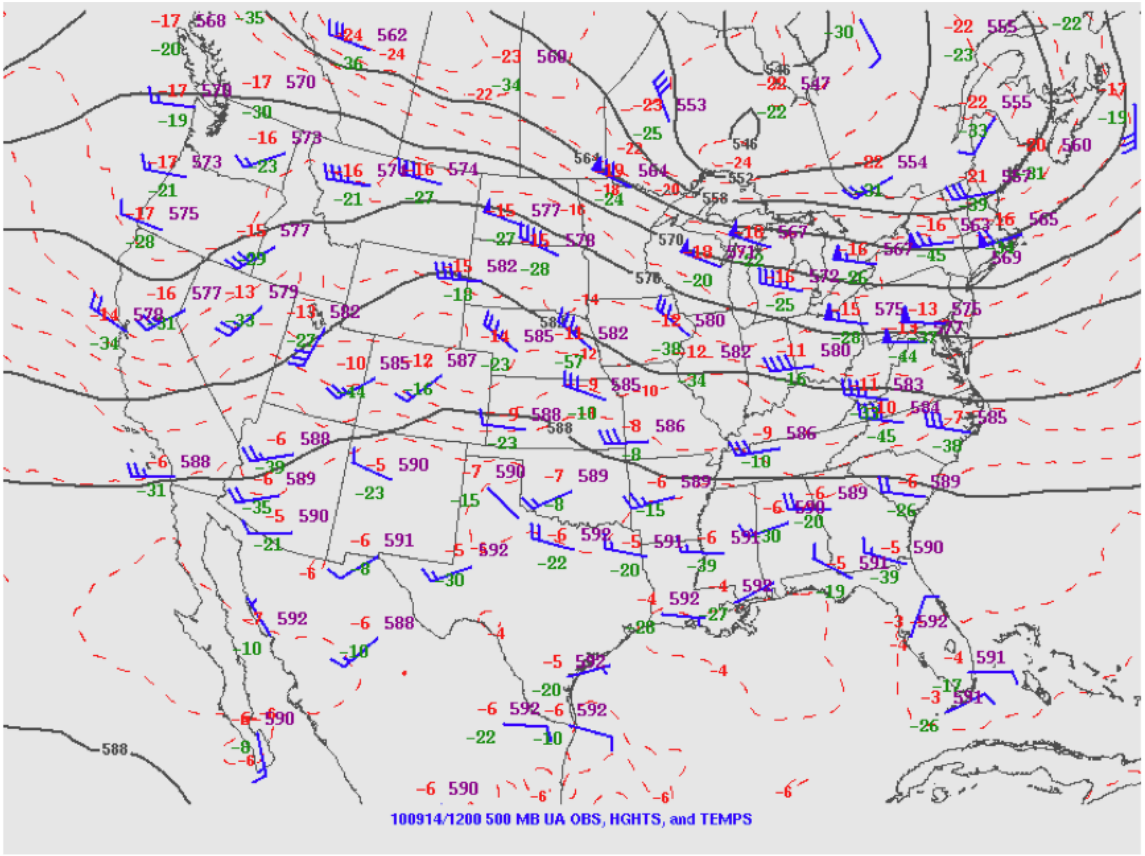


**Fig. 4.25.** As in Fig. 4.2, but 1200 UTC on 14 September 2010.

500-hPa-analysis for 1200 UTC 14 September (Fig, 4.25) reveals a weakly amplified ridge over much of the west-central United States (from Montana, southward through Oklahoma). There is also evidence of a short wave over northern California. 500-hPa-analysis for 0000 UTC 15 September (which was just a few hours prior to the time convection over northeast Colorado moved into northwest Kansas and organizes, forming a bow echo) reveals slight amplification of the aforementioned shortwave, which had now moved into Idaho and Montana (Fig. 4.26). It began propagating eastward, moving into central Idaho, through

Nevada, Utah, and the 4 Corners, pushing the ridge off to the east. Additionally, the large-scale flow became quasi-zonal at this point. By 1200 UTC, the shortwave disturbance moved into the central United States, while flow remained primarily zonal (not shown).

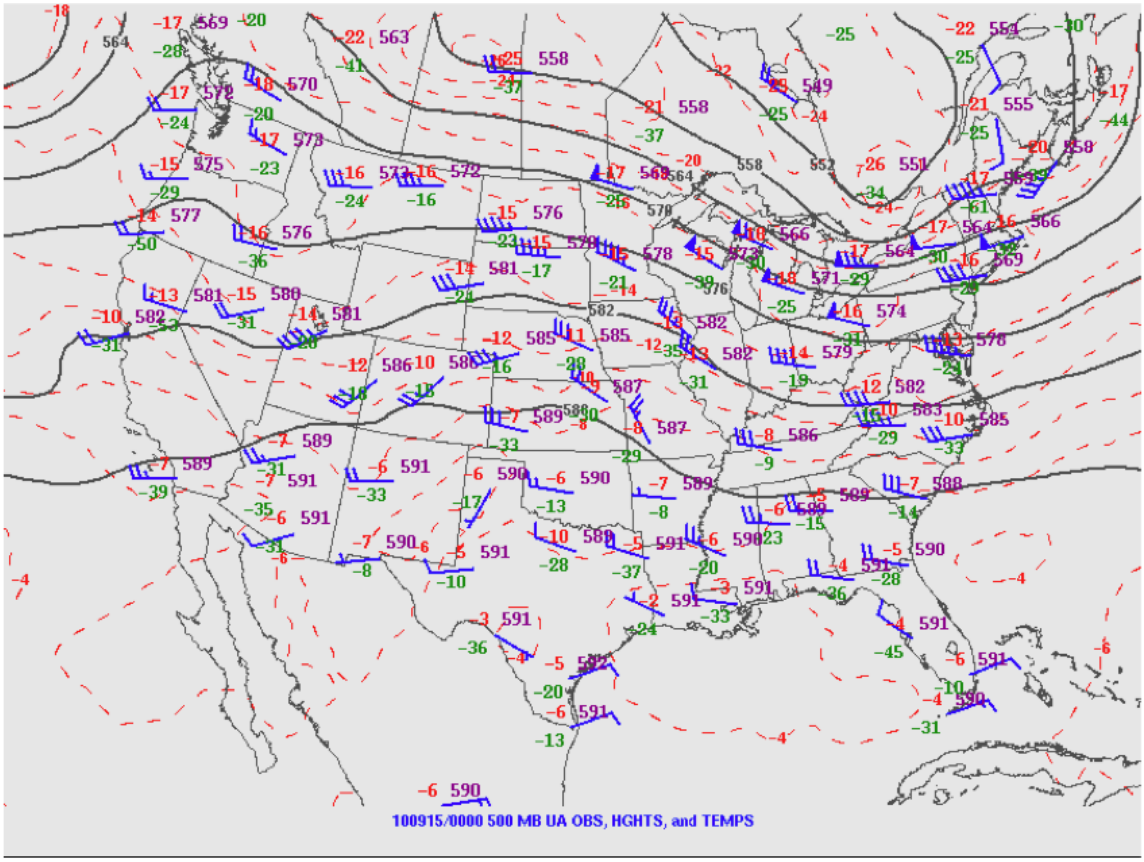


**Fig. 4.26.** As in Fig. 4.2, but 0000 UTC on 14 September 2010.

850-hPa-analysis at 0000 UTC 15 September (Fig. 4.27) shows existence of a weak nocturnal low-level wind maximum, as winds in the south-central United States were southerly, moving in from the Gulf, and increasing humidity, as is

portrayed in the low dewpoint depressions. This same analysis for 1200 UTC (Fig. 4.28), which is a couple of hours before the third phase of the bow and arrow event on this day, reveals intensification of the LLJ, with winds up to 40 knots, and out of the south-southwest. Warm air advection was taking place, as winds are crossing tight temperature gradients over Kansas, initiating ascent in this area.

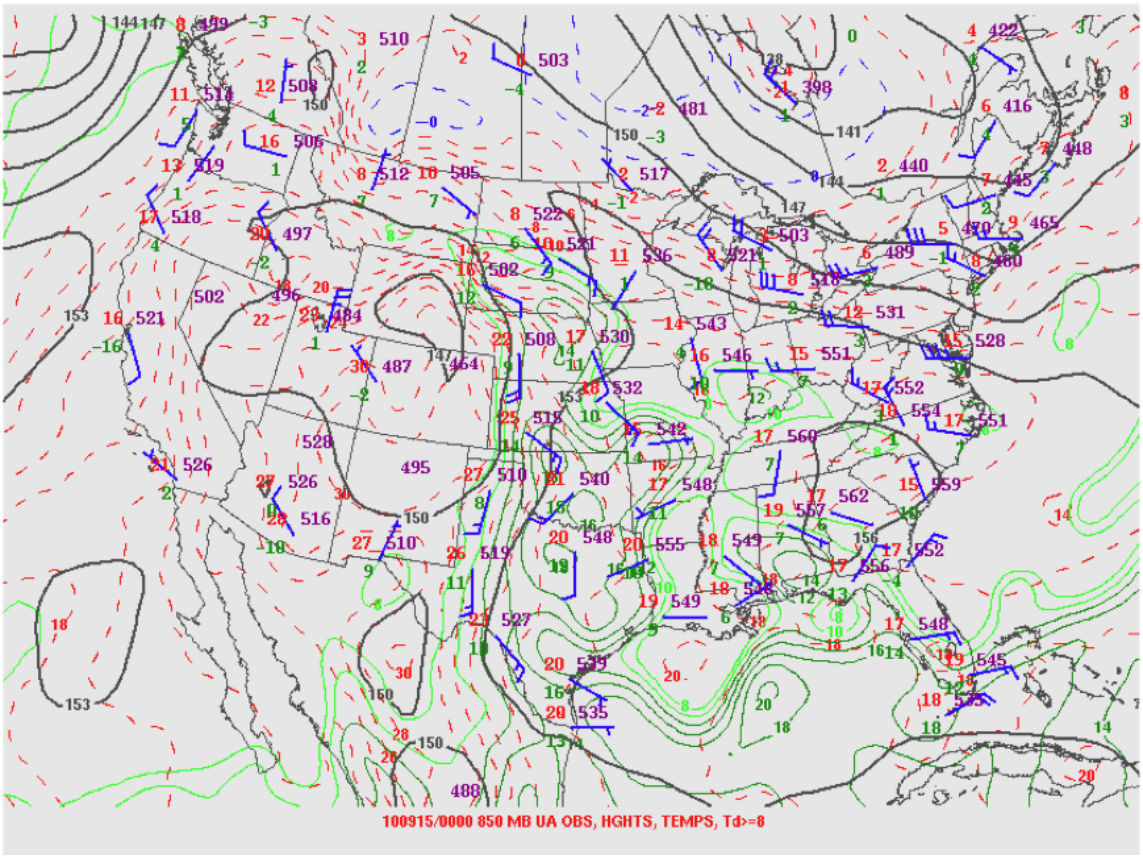


**Fig. 4.27.** As in Fig. 4.4, but 0000 UTC on 15 September 2010.

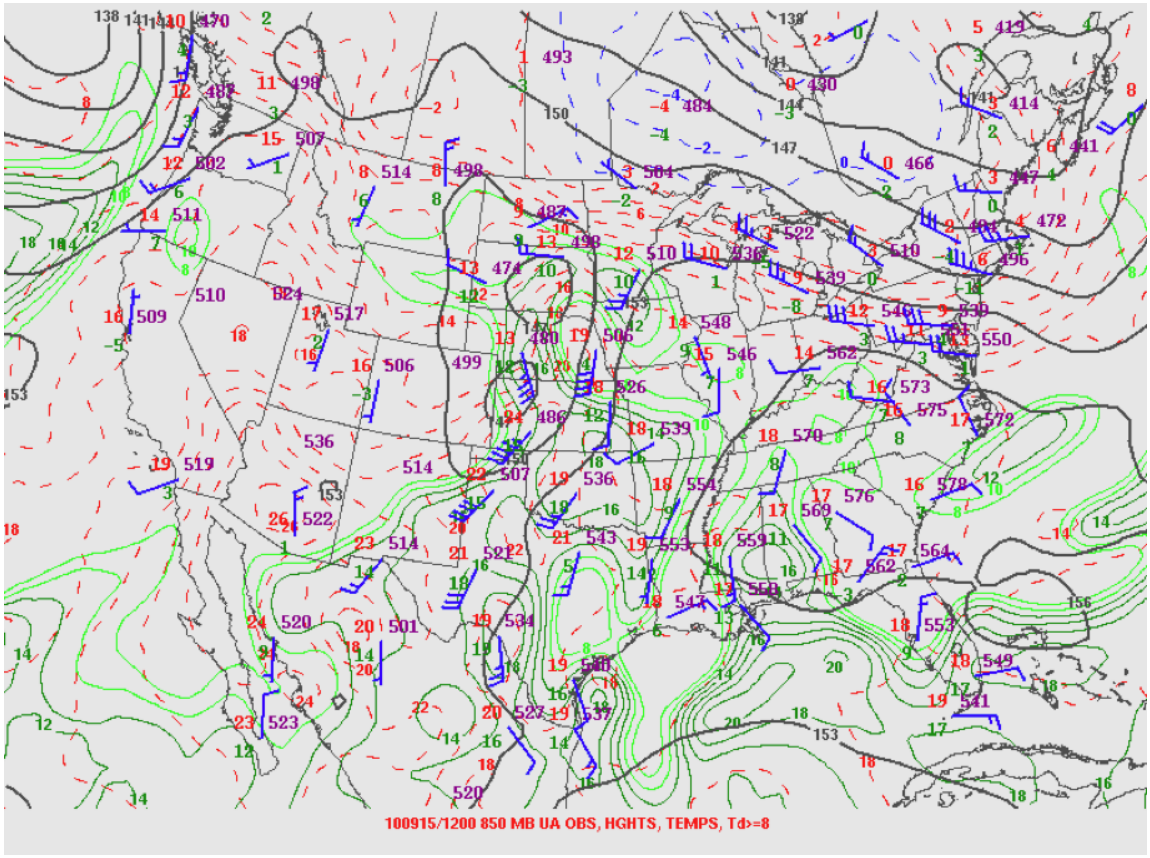


**Fig. 4.28.** As in Fig. 4.4, but 1200 UTC on 15 September 2010.

Surface analysis for 0000 UTC 15 September displays a leeside low in the early stages of cyclogenesis, located in southeast Colorado (Fig. 4.29). At 1200 UTC (Fig. 4.30), the low-pressure center had moved eastward, into west-central Kansas. Associated with the low, was a warm frontal boundary that extended to the southeast, becoming a stationary front through central Oklahoma, and into northeast Texas, and into central Louisiana.

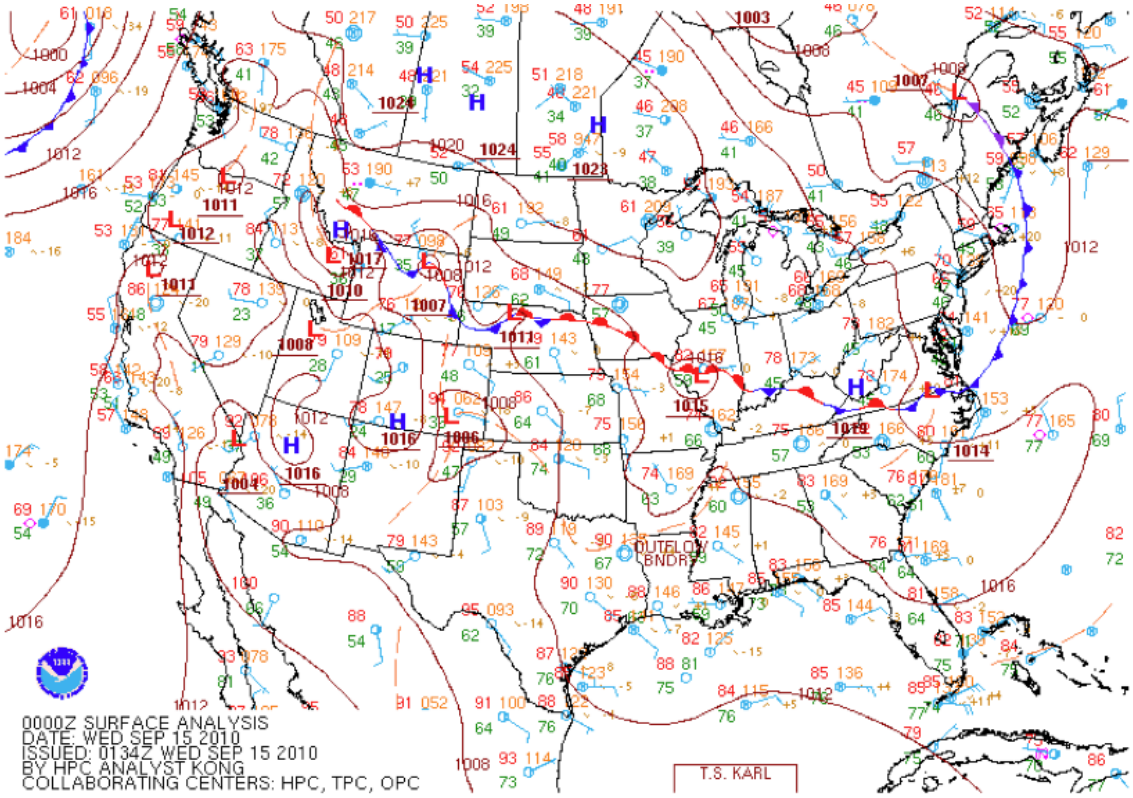


**Fig. 4.29.** As in Fig. 4.13, but 0000 UTC on 15 September 2010.

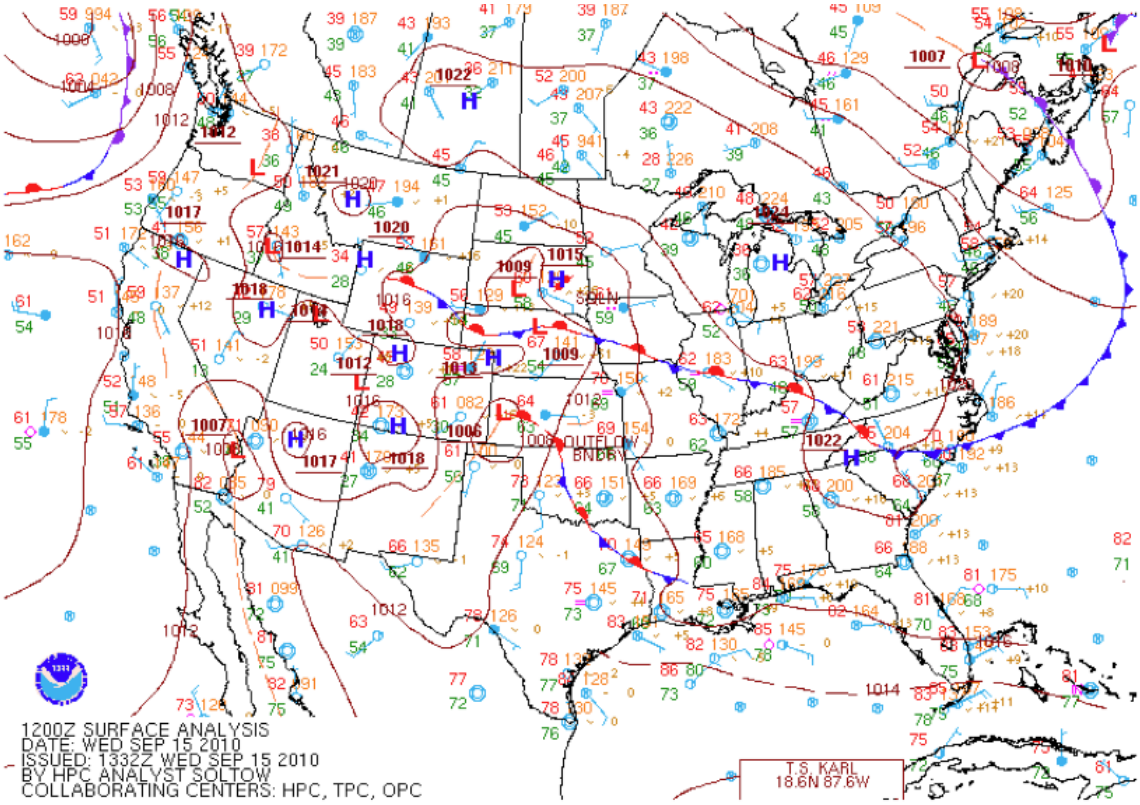


**Fig. 4.30.** As in Fig. 4.13, but 1200 UTC on 15 September 2010.

From a synoptic standpoint, all the ingredients necessary for initiating convection were available in eastern Colorado and western Kansas. At the upper levels, a jet streak was present, as well as a short wave disturbance, at the surface, there was an area of low pressure, causing convergence and lifting, with divergence aloft. At the 850-hPa-level, the presence of a LLJ enhanced the instability in the environment, fueling the system once it was initiated.

To try to obtain a more clear understanding of the environment on the mesoscale, analysis is performed for two different time periods: 0359 UTC and 1902 UTC 15 September. These were two of the times in which the convective

arrows were matured. Although there were three phases of the arrow, these analyses should provide a good representation of the environment, as the 0359 analysis is at the beginning of the duration of this system, and the 1902 UTC analysis is toward the end of the period.

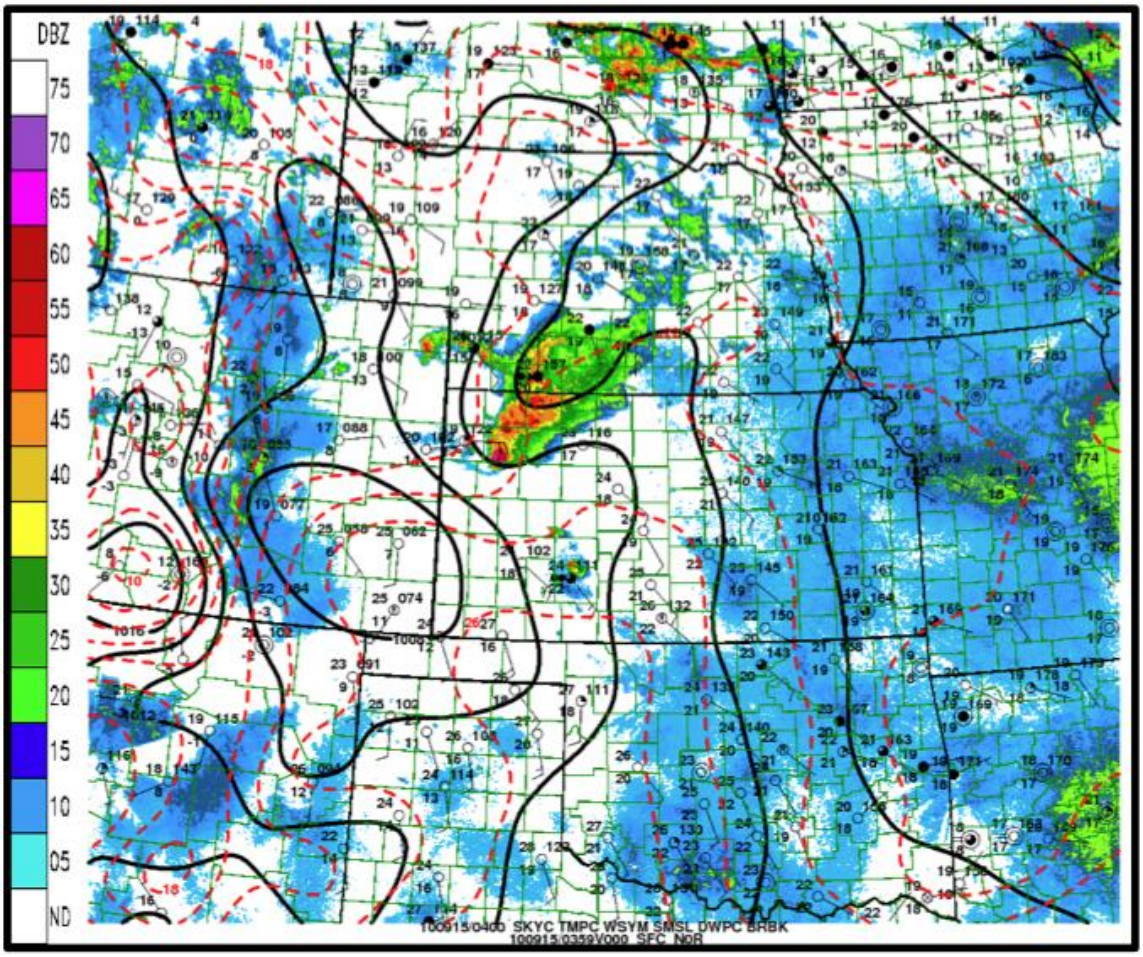


**Fig. 4.31.** As in Fig. 4.7, but 0359 UTC on 15 September 2010.

At 0359 UTC (Fig. 4.31), the presence of a bow echo exists over northwest Kansas and southwest Nebraska. A convective arrow extended northwestward,

into northeast Colorado. The surface analysis shows an area of higher pressure in the cold pool region, most likely associated with the meso-high. Due to coarse representation of surface observations, it is hard to determine any firm conclusions about the temperatures associated with the system; however, a temperature contour of 20°C goes through the area just behind the outflow boundary. The direction of wind near the convective arrow varied, as it was spreading outward in all directions due to the outflow from the system. Again, it appears that the arrow is perpendicular to surface isotherms.

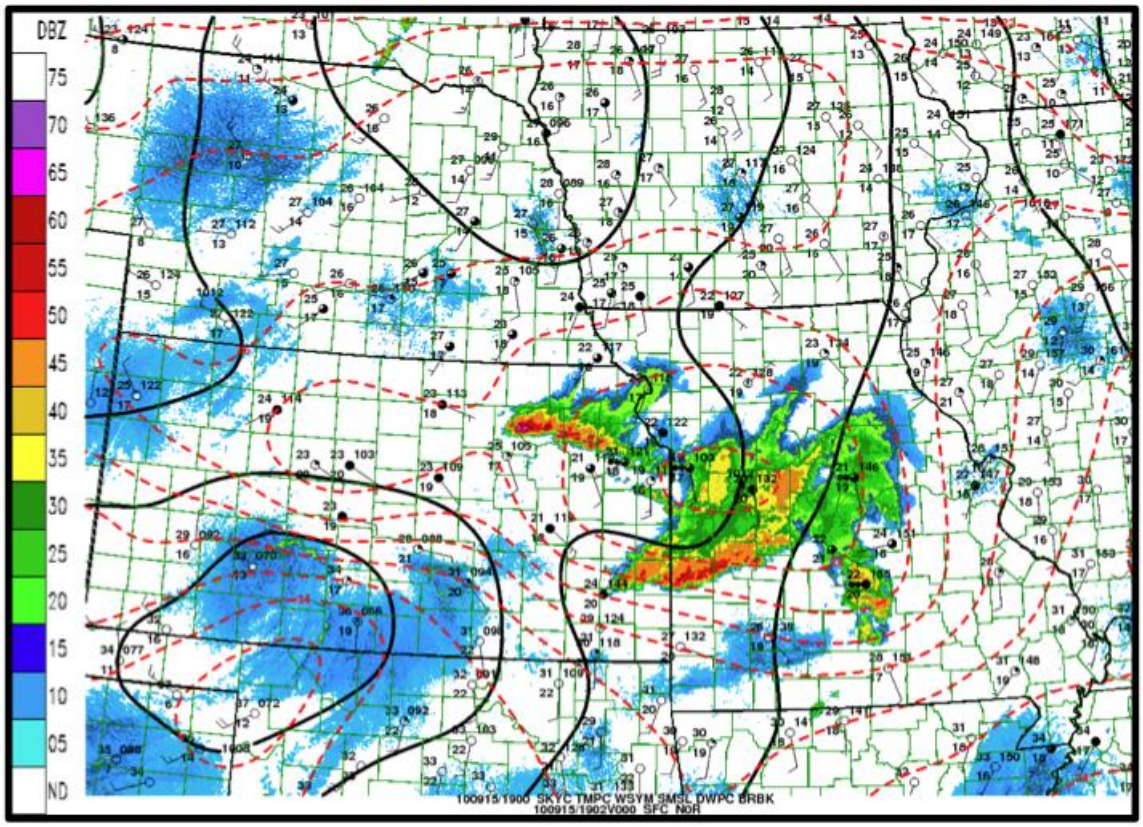


**Fig. 4.32.** As in Fig. 4.7, but 1902 UTC on 15 September 2010.

By 1902 UTC (Fig. 4.32), the system had moved toward the east, into northeast Kansas and west-central Missouri. A strong bow echo was heading toward the southeast, with a deep convective arrow trailing. Again, due to the coarse resolution of surface observations, pressure contours may not be accurate. Overall, pressure was increasing from west to east. There was, however, an evident area of lower temperature located in the cold pool region, as is expected. Temperature gradients were tight around the system, especially to the south. Surface winds were southerly near the convective arrow region, but do not appear to be crossing any isotherms, causing temperature advection that may have created upward motion in the arrow region.

Observational analysis gives little information regarding an explanation for the convective arrow. It is therefore necessary to use model simulations to recreate this event. Numerical simulation for this event was successful, and analysis of model output will be discussed in section 5.3.

## 4.2 Impact Verification

Precipitation estimates are analyzed to verify that the convective arrow regions of these systems are capable of producing heavy precipitation, which can lead to flooding. A combination of rain gauge data (at a 4-km spatial resolution), and hourly estimates from composite radar reflectivity data make up the NWS Office of Hydrology stage IV analyses (Lin and Mitchell 2005). These are used to examine three-hour estimates of rainfall over the area in which the arrow formed

and propagated over. The time periods chosen are those that match the times in which reflectivity was the highest on radar in the arrow region. Additionally, SPC Archived Storm Reports are compared to radar reflectivity to verify wind and hail reports associated with the convective arrow.

### *4.2.1 5 July 2003 Event*

Precipitation estimates for this event are for the 0100 UTC to 0400 UTC time period. The first convective cells in the arrow region were noticed shortly after 0100 UTC, and remained organized until 0430 UTC, when the arrow rotated to become the new bow echo for the next arrow to form behind. Stage IV analysis (Fig. 4.33) show that there was heavy precipitation in Northern Indiana, as is expected, as the arrow was quasi-stationary over this area for the three-hour time period. Rainfall was particularly high in the center of this area (where the arrow remained the entire time), and show 3-hour totals as high as 50 to 100 millimeters (mm).

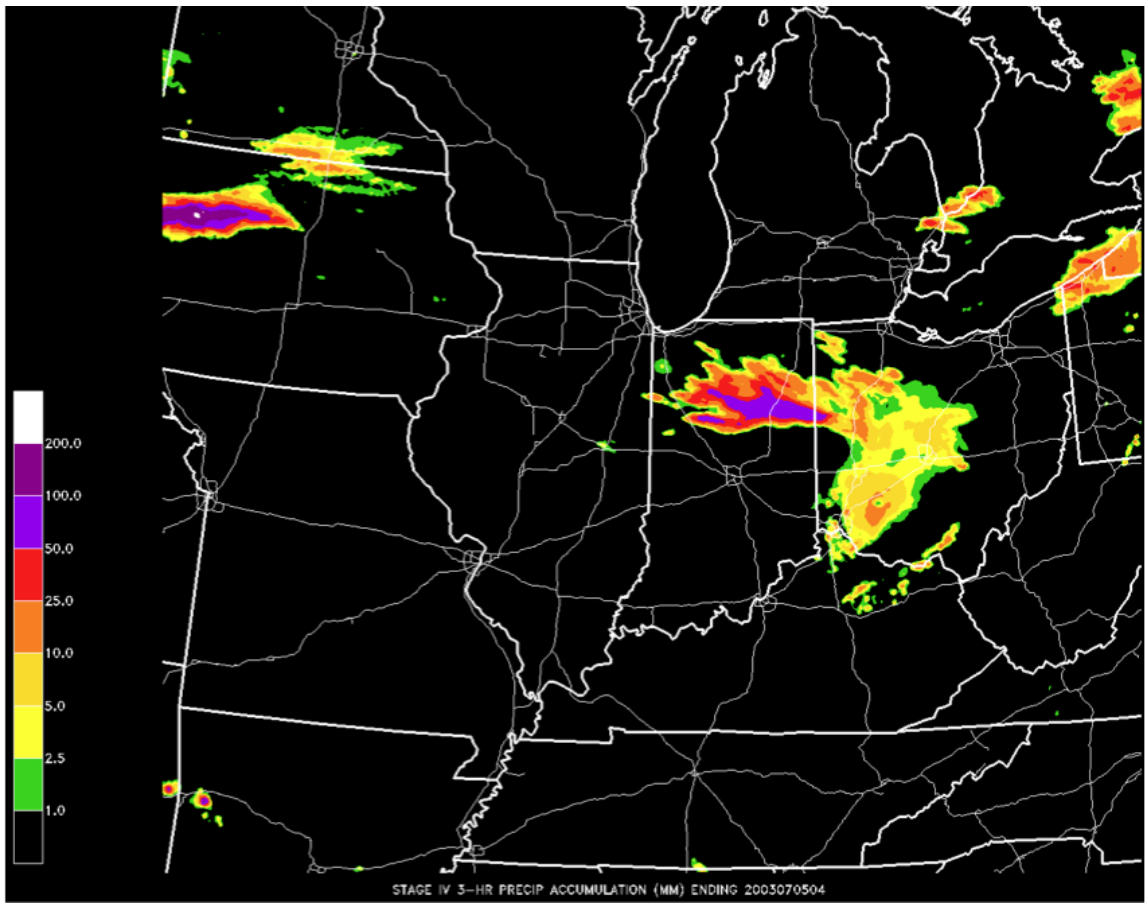


**Fig. 4.33.** Analysis of 3-h estimated precipitation from 5 July 2003 (0100 UTC to 0400 UTC).

### *4.2.2 18 June 2006 Event*

The times in which the convective arrow was most prominent for this case were 0500 UTC through 0800 UTC. The first sign of convection, on radar reflectivity imagery, was around 0500 UTC, and the arrow lost organization after 0800 UTC. Stage IV precipitation analysis (Fig. 4.34) shows that the convective arrow did produce a great amount of rainfall. Although the estimated precipitation

is not as heavy in as widespread of an area as in the July 2003 case, there are still areas that received between 50 and 100 mm.

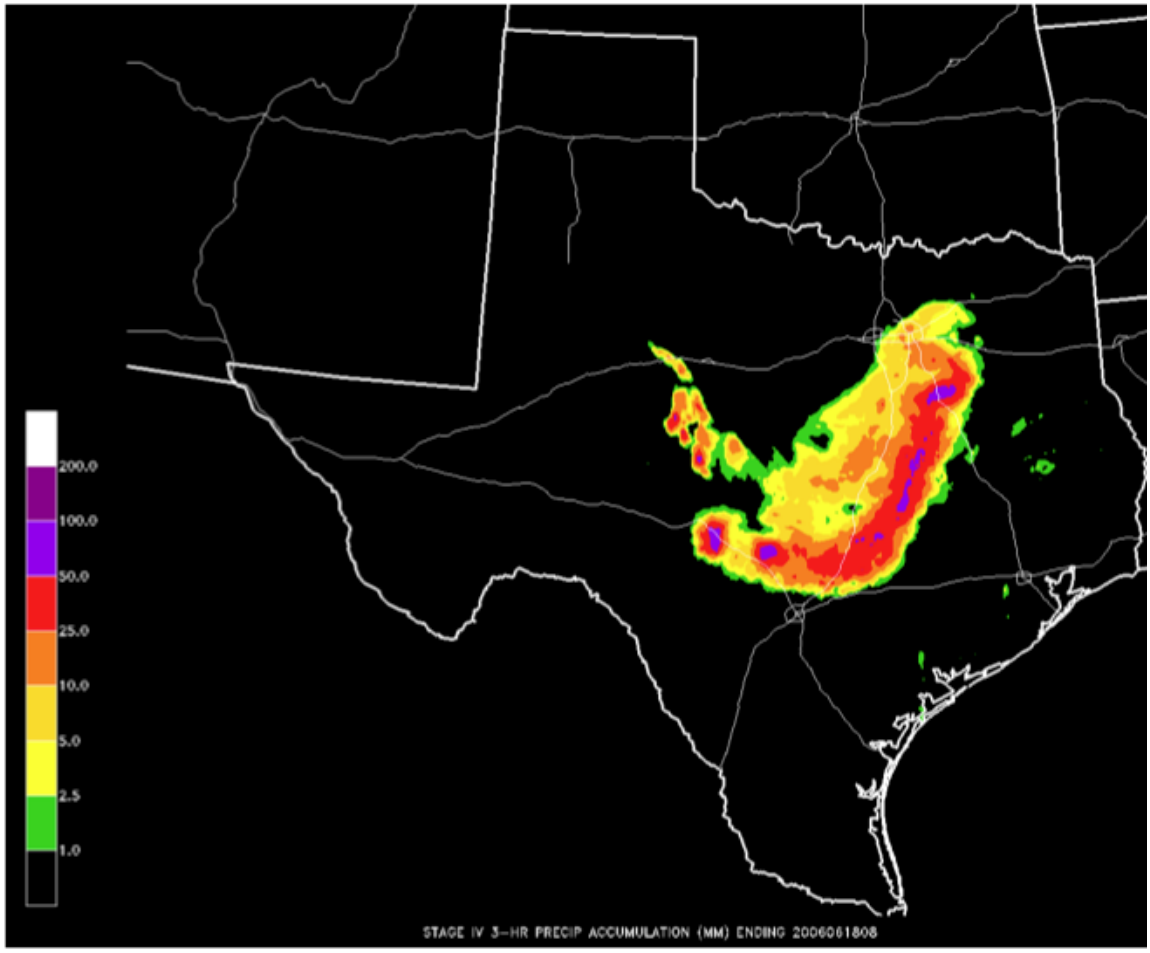


**Fig. 4.34.** Analysis of 3-h estimated precipitation from 18 June 2006 (0500 UTC to 0800 UTC).

### *4.2.3 08 May 2009 Event*

From 1700 UTC to 2000 UTC the convective arrow of this bow and arrow system lingered over the area between south Missouri and near the Arkansas-

Missouri border. These times are chosen for the estimated precipitation analysis. The precipitation analysis for this time period (Fig. 4.35) shows that while there was not nearly as much precipitation resulting from the convective arrow, there was still a fair amount, resulting in a total of 25 to 50 mm in some places.

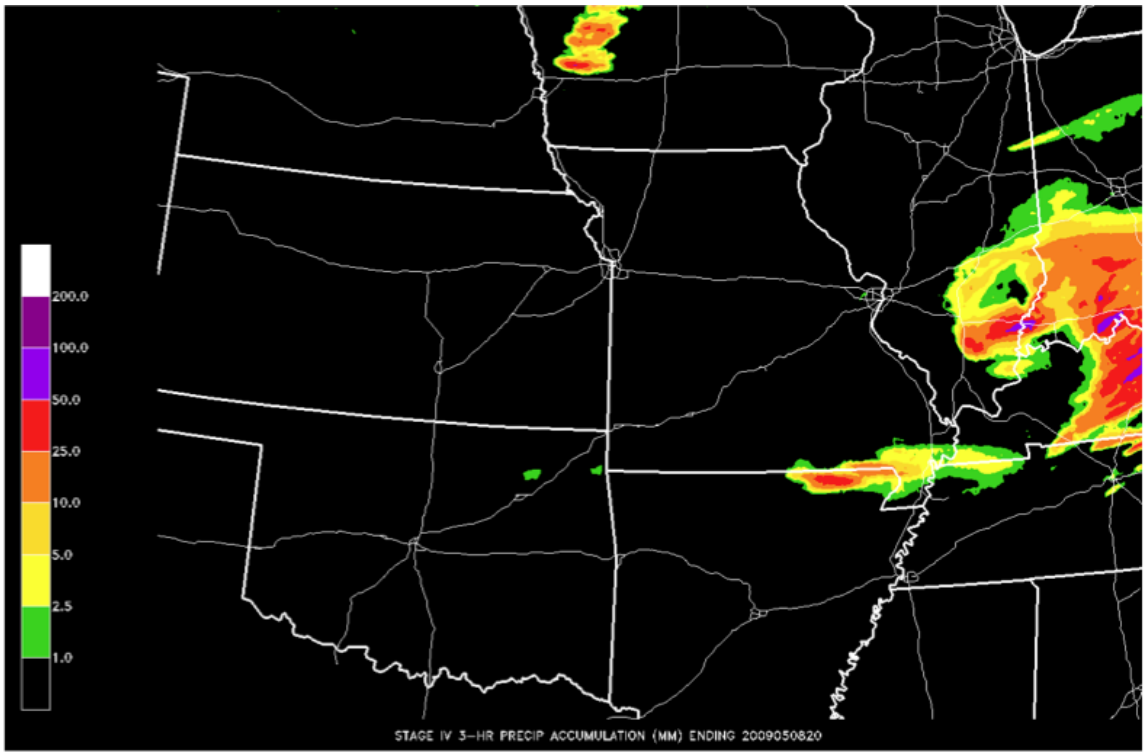


**Fig. 4.35.** Analysis of 3-h estimated precipitation from 08 May 2009 (1700 UTC to 2000 UTC).

### *4.2.4 15 September 2010 Event*

Two different three-hour time frames are chosen for precipitation analysis for this event, since the arrow re-occurred in different phases, over different locations. The first time period chosen is 0400 UTC to 0700 UTC. At this time, the

bow echo was in northwestern to northwest-central Kansas, while the arrow followed, extending from southwest Nebraska, into northwest Kansas. The second three-hour time period is during the final phase of the bow and arrow event on this day, from 1700 UTC to 2000 UTC. At this time, the bow was moving toward the south-southeast, from eastern Kansas, into western Missouri. The arrow was primarily located in northeastern Kansas throughout the duration of the three hours.

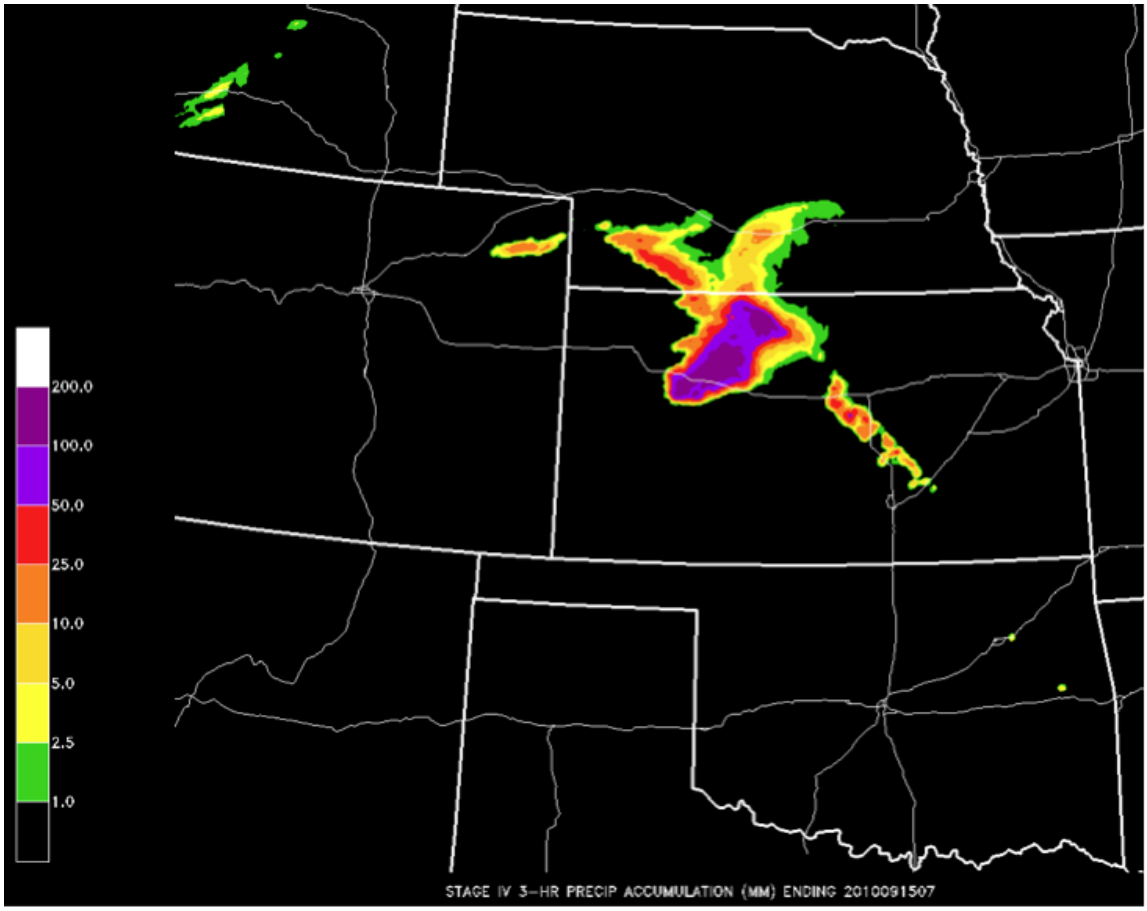


**Fig. 4.36.** Analysis of 3-h estimated precipitation from 15 September 2010 (0400 UTC to 0700 UTC).

The 0400-0700 UTC estimated precipitation (Fig. 4.36) shows that there was heavy precipitation over much of northwest Kansas. While the heaviest precipitation was more widespread in the bow echo region of the system, there is still evidence that a large amount of precipitation fell in the arrow region, producing rainfall from 25 to 50 mm in some areas. Again, the rainfall pattern matches the radar reflectivity pattern in the 1700-2000 UTC time frame, as well (Fig. 4.37). More precipitation fell in the arrow region for this phase of the system, however. There are some places that received an estimate of 50 to 100 mm of precipitation.

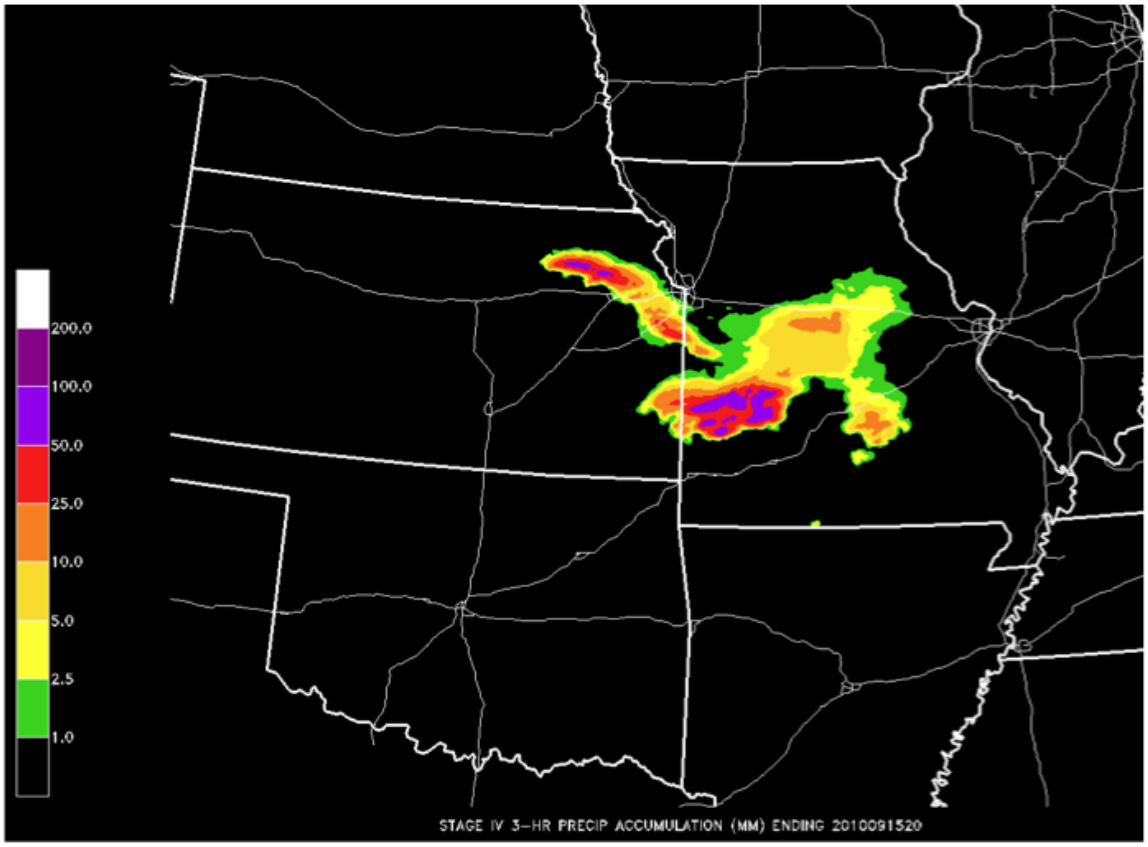


**Fig. 4.37.** Analysis of 3-h estimated precipitation from 15 September 2010 (1700 UTC to 2000 UTC).

### *4.2.5 Verification of Hail and Wind*

Bow and arrow systems are capable of producing more than just extreme rainfall. As discussed in the Introduction, hail and severe winds are also consequences. To show verification of this, a different event is used. The event occurred on 18 June 2010, over Iowa. A cluster of convection that first-appeared in northern Nebraska moved into Iowa and organized into a bow echo, with a significant arrow region behind it (Fig. 4.38). SPC Archived Storm Report data (Fig. 4.39) shows an area in northwestern and north-central Iowa that had several wind and hail reports (circled in red). These reports coincide with the times that the arrow region was over the cities in which reports were made. The reports for wind damage stated that several trees and power lines were down, resulting in power outages. The hail reports estimated golf-ball-sized hail, causing damage to trees and roofs.

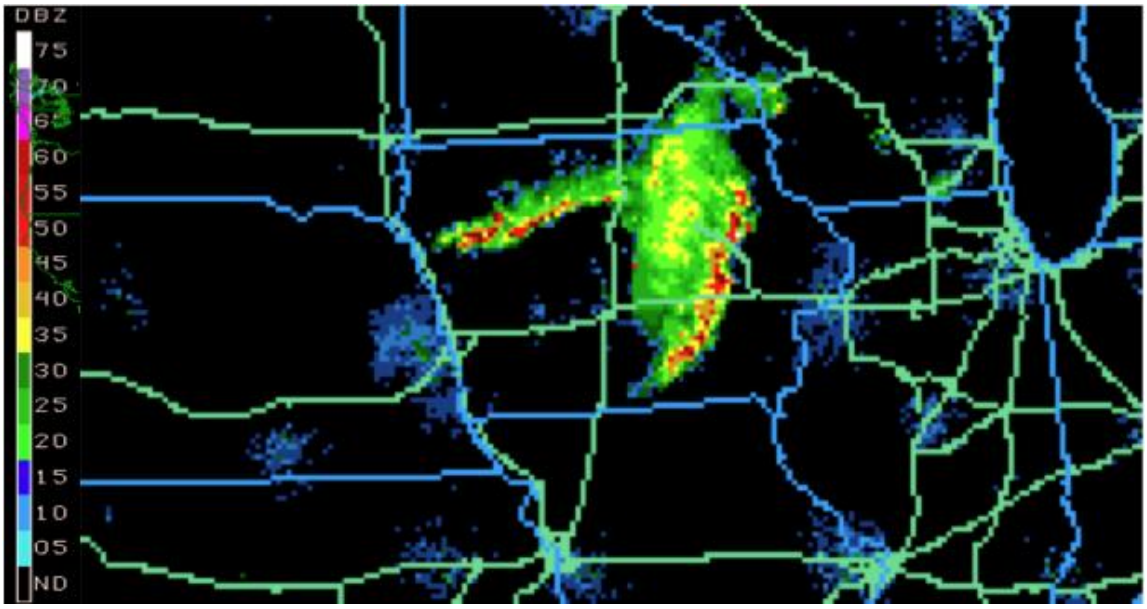


**Fig. 4.38.** Composite radar reflectivity for 18 June 2010 at 1657 UTC. From NCAR's MMM Image Archive.

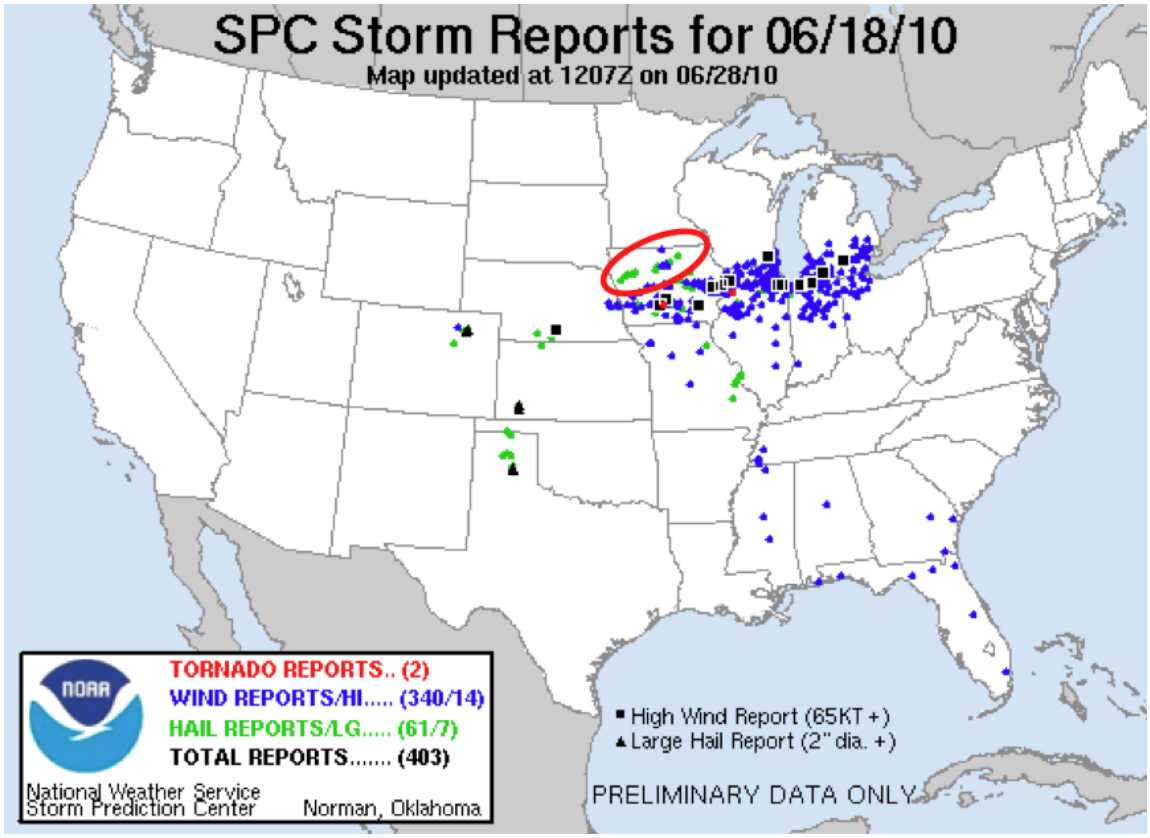


**Fig. 4.39.** SPC Archived Storm Reports for 18 June 2010, showing reports for tornadoes (red bullets), severe winds (blue bullets) and hail reports (green bullets). The red circle depicts the area in which a convective arrow formed on this day. Several of the reports inside the red circle are associated with the arrow. From NOAA's SPC.

# 5. ANALYSIS OF NUMERICAL MODEL SIMULATIONS

As mentioned earlier, while the previously discussed observational analysis is quite useful for determination of the synoptic-scale environment, the resolution is too coarse for a thorough investigation of the environment on the mesoscale. Because the bow and arrow occurs on this smaller scale, it is important to obtain quality analysis of this scale in order to determine a possible explanation for the arrow phenomenon. Using output from the WRF-ARW numerical model simulations, and the RIP program, each case is investigated in detail to determine whether there are any common outstanding characteristics among the cases, leading to a hypothesis for the problem in this study. As mentioned previously, three cases are used, and are most likely representative of the full sample of bow and arrow cases.

## 5.1 18 June 2006 Event

The bow and arrow event for this case took place in central Texas, between 0500-0700 UTC 18 June 2006. A comparison of the observed radar reflectivity (Fig. 5.1a) with simulated radar imagery (Fig. 5.1b) shows a slight difference in the location of the event, as well as the orientation of the system. Observed imagery shows the entire system primarily in central Texas, with the leading line (or the bow) oriented from southwest to northeast, while the arrow is perpendicular to the bow, toward the northwest. The simulated imagery shows the bow echo region in

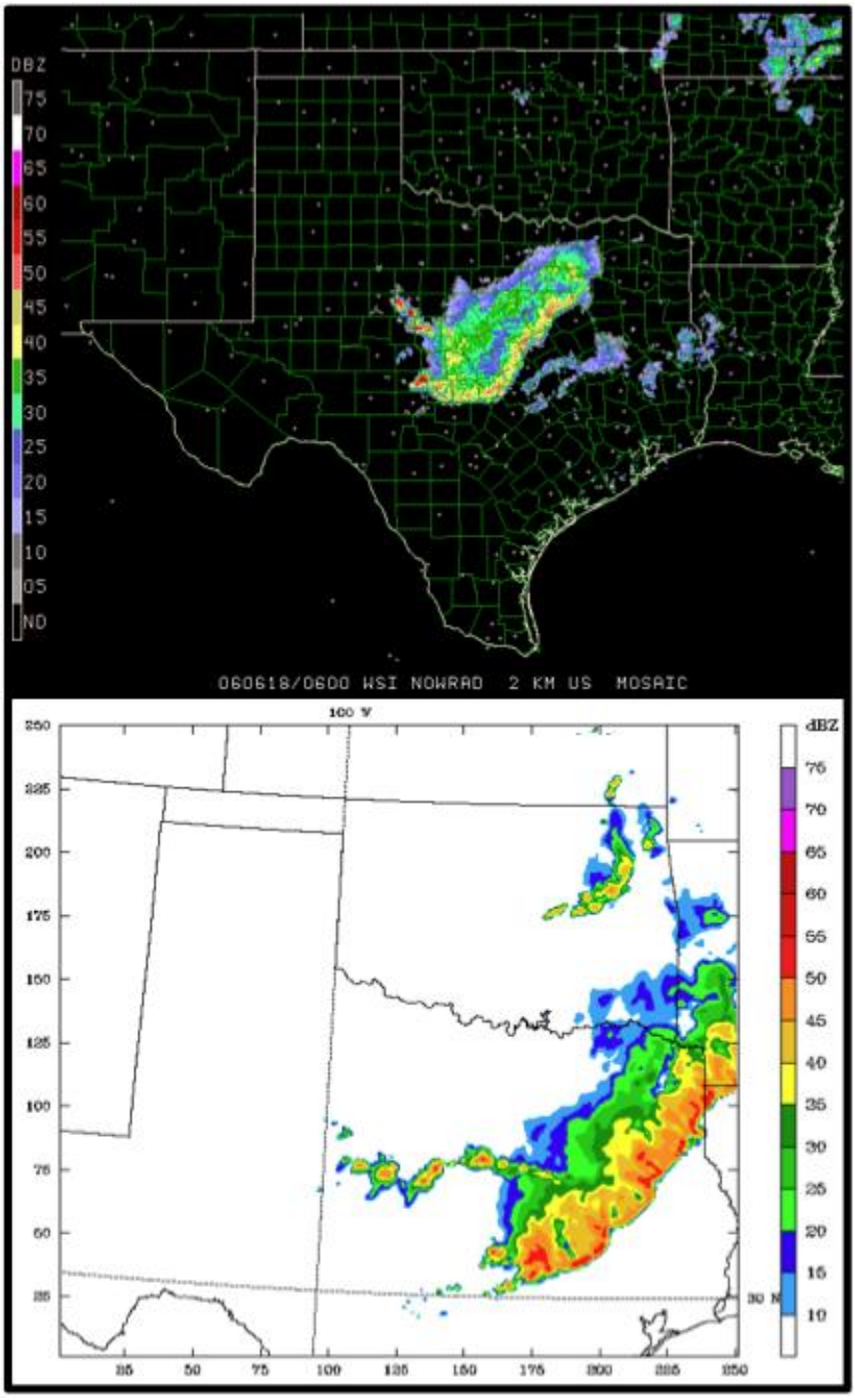


**Fig. 5.1.** Comparison of (a) real-time radar reflectivity 0600 UTC 18 June 2006 (from NCAR's MMM Image Archive), and (b) WRF numerically simulated radar reflectivity 0400 UTC 18 June 2006. Color represents reflectivity in increments of 5 dBZ.

the same southwest to northeast orientation, but the location is further to the east, extending from central Texas, up into southwest Arkansas. The arrow region in this image extends more toward the west, than the northwest, as in the observed case. Another obvious difference is the horizontal thickness of the leading line, which is greater in the simulated image. Additionally, there are more areas of higher reflectivity associated with the bow echo in the simulation. Another difference is in the time of the events. In real time, the arrow existed from 0500 to 0700 UTC, while in the simulation, the arrow begins at 0200 UTC. The end time is not known because data are not available past 0600 UTC, although the arrow region is still evident at that time (not shown). As mentioned in the Data and Methods section, the purpose of this study is to examine the processes leading up to the formation of the arrow, and therefore, regardless of spatial and timing errors, this simulation is still useful.

An important aspect of understanding the ambient environment of the bow and arrow system is to determine the origin of the air parcels associated with the updraft, as well as the path followed to get there. Calculating backward trajectories allows analysis of this in both horizontal and vertical planes. To determine the exact location of updrafts, 500-hPa vertical motion plots are analyzed. Several levels near 500-hPa are tested to see which level shows the highest vertical speeds in the updrafts for the arrow region. For this case, it is determined that the 575-hPa level produces the best results, displaying upward motion at 100-dPa $s^{-1}$ (Fig.

5.2). Using this plot, bullets are then placed in the exact location of the greatest updrafts, and are used as starting points for the backward trajectories.

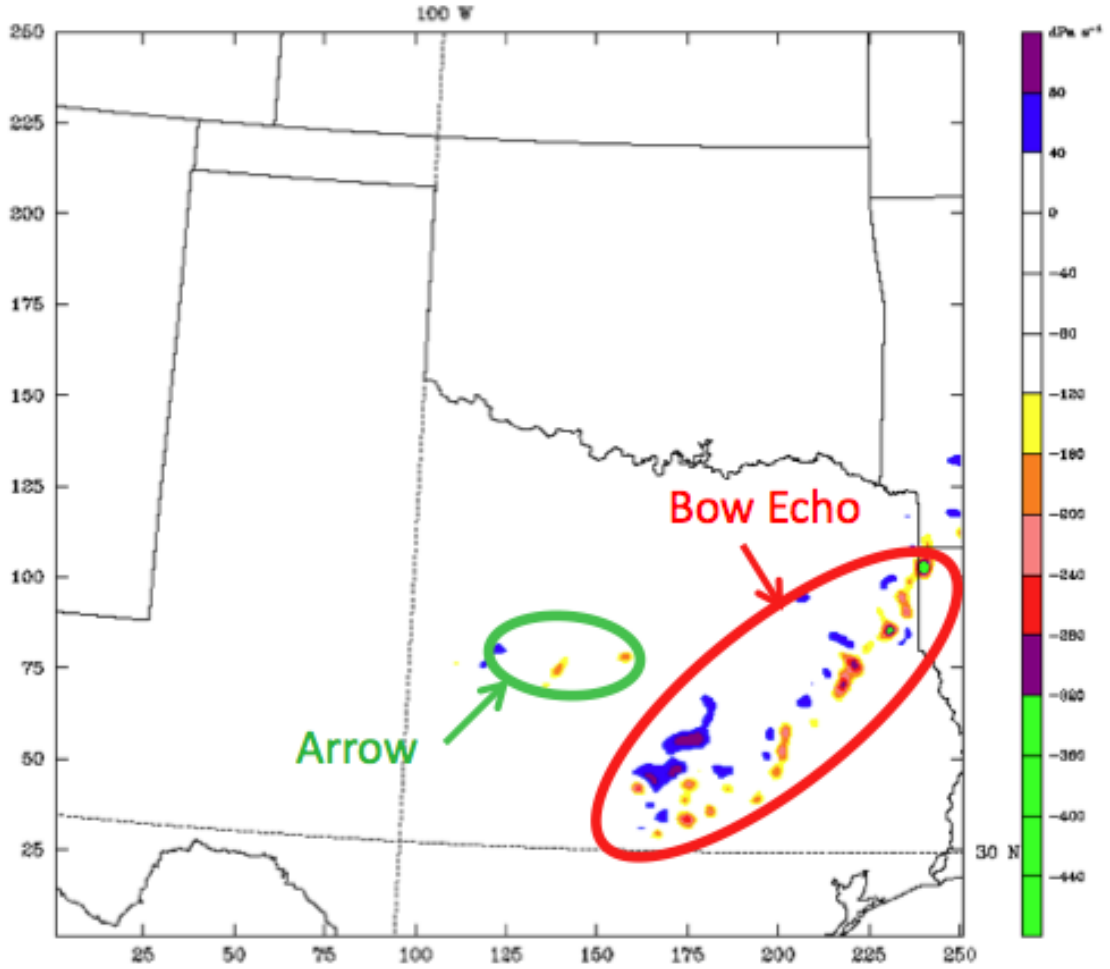


**Fig. 5.2.** Vertical velocity at 575-hPa, 0400 UTC 18 June 2006. This is created using WRF model output and the RIP4 program. Color represents vertical wind speed in increments of 40-dPa $s^{-1}$. The bow echo is circled in red, while the arrow is circled in green.

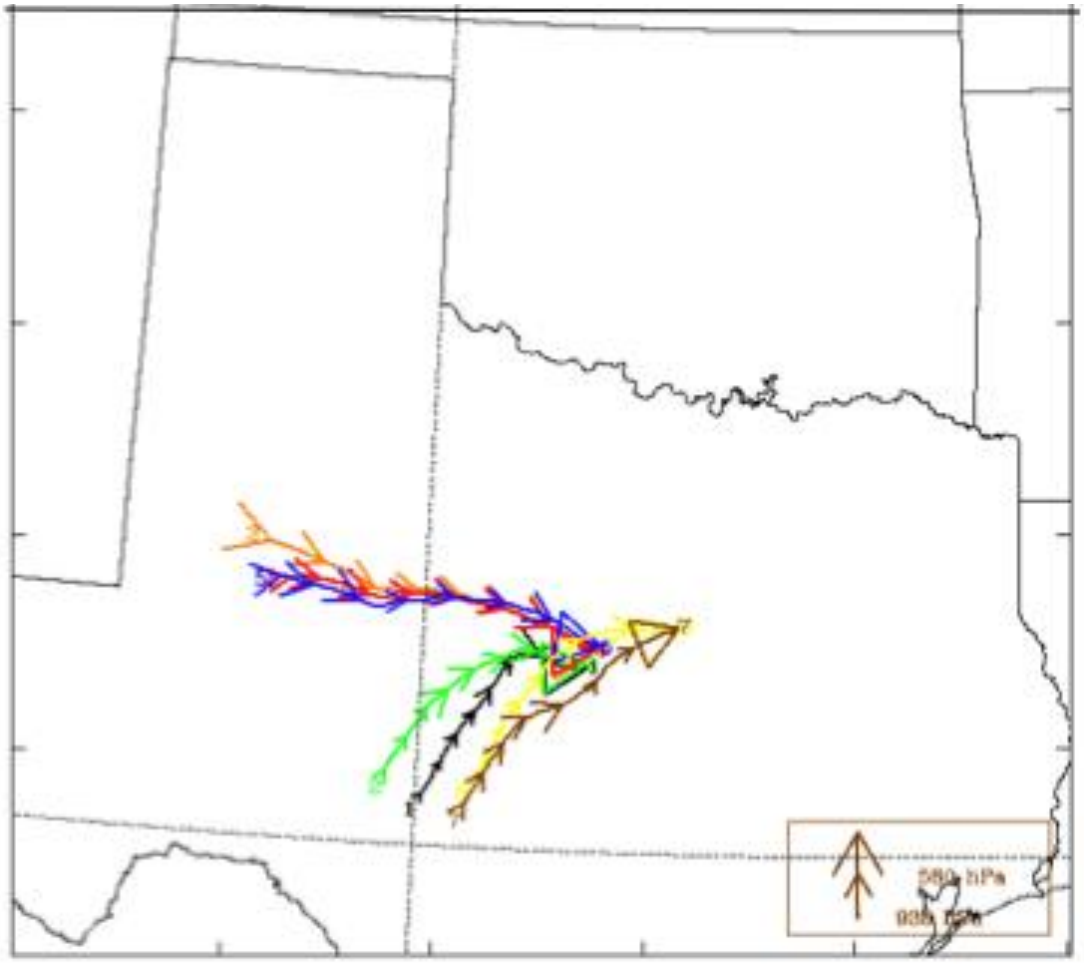

**Fig. 5.3.** Back-trajectories in the XY-plane, from 0400 UTC 18 June 2006, back to 2100 UTC 17 June 2006. This is created using the RIP4 program with WRF model output. Each arrowed notch represents one hour, while the size of the arrows increases with vertical location.

Trajectories for this event are calculated over a 7 hour period, from 0400 UTC 18 June, back to 2100 UTC 17 June. The back-trajectory in the X-Y plane (Fig. 5.3) shows four of the seven trajectories (black, green, yellow, and brown; BGYB) originating out of the southwest, before making a turn for the east in the last couple of hours. The other three (orange, blue, and red; OBR) are coming from the west-northwest. This indicates that there are two primary source regions for parcels ending up in the updrafts within the convective arrow. Each notch on the trajectory arrows represents one hour, starting at 2100 UTC 17 June and ending at the tip of the arrow head at 0400 UTC 18 June. Viewing back-trajectories in the X-Z plane (Fig. 5.4) allows diagnosis for the level and time at which lifting occurs. From this plot, it is evident the air parcels fluctuate vertically throughout time, but most of them make their steepest climb within the last 2-3 hours. Additionally, most of the trajectories appear to gradually rise vertically, and then sharply rise in the last 1-2 hours. The sharp rise takes place at different levels for different trajectories, but they primarily appear to begin their gradual rise between the 850 and 800-hPa levels, and then make their sharp ascent at the 800 or 700-hPa level.

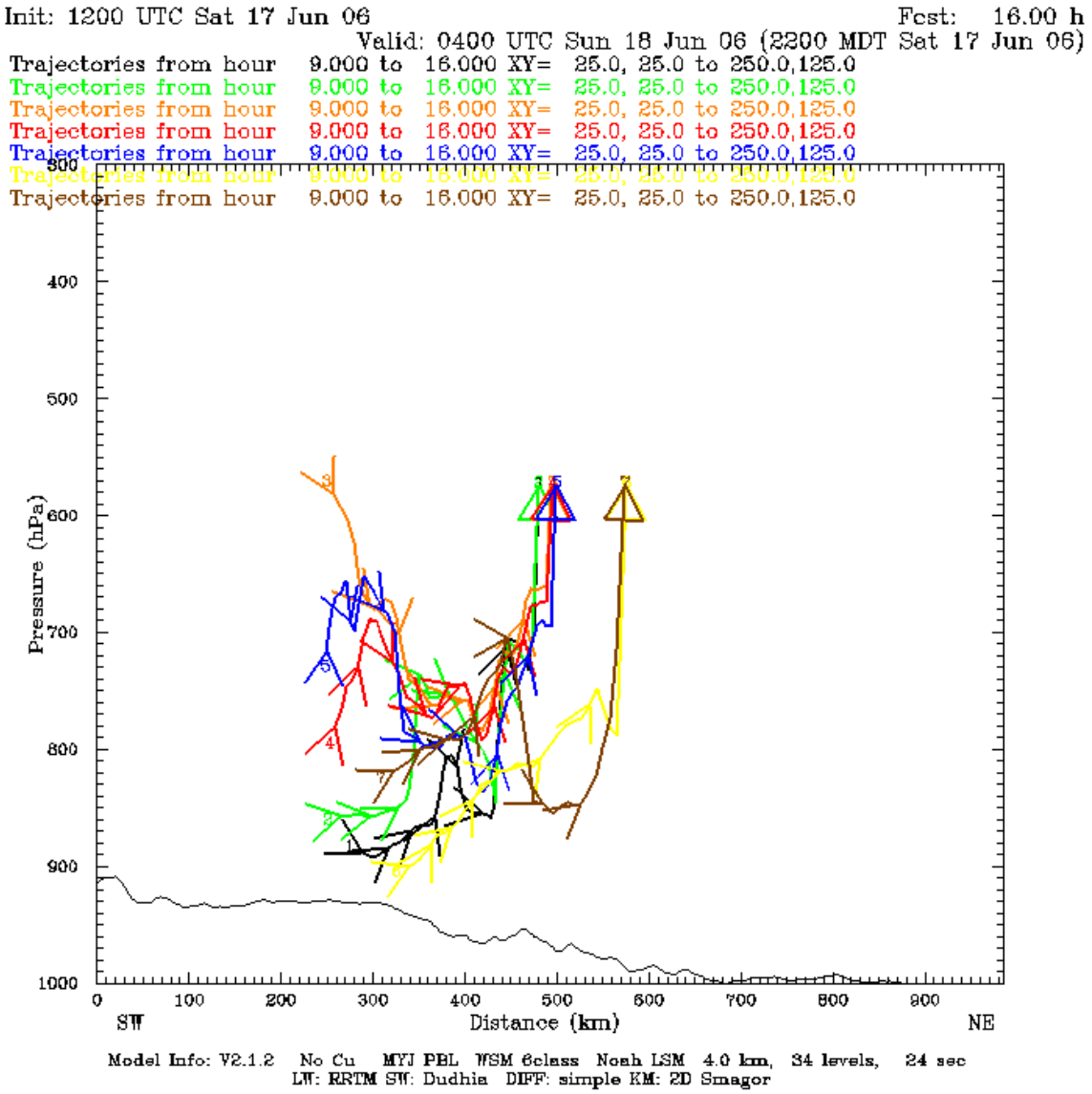


**Fig. 5.4.** Back-trajectories in the XZ-plane, from 0400 UTC 18 June 2006, back to 2100 UTC 17 June 2006. This is created using the RIP4 program with WRF model output. Each arrowed notch represents one hour. The X-axis represents horizontal distance, while the Z-axis represents pressure level (hPa).

Analysis is performed, using plots that show horizontal temperature variations, as well as wind speed and direction for the 850, 800 and 700-hPa pressure levels, as well as the surface. The times 0200 UTC and 0400 UTC are chosen for analysis because at these times, the bow echo has already moved through the area, and by 0200 UTC the first convective cells appears on radar imagery (Fig. 5.5a). By 0400 UTC, the convective arrow is fully organized in a quasi-linear orientation (Fig. 5.5b), and this is the time from which the back-trajectories are calculated. In Fig. 5.5, the black bullets represent the locations of greatest updraft speed (from 0400 UTC).

Because many of the trajectories begin their gradual rise near the 850-hPa level, this pressure level is used to analyze possible lifting mechanisms associated with temperature advection and/or wind variations. Recall from Fig. 5.3, BGYB come from the southwest, taking a turn to become westerly at 0200 UTC, while the OBR parcels are primarily westerly at 0200 UTC. On the 850-hPa plot for this time (Fig. 5.6a), winds in south-central Texas are coming out of the southwest, while winds in north Texas and Oklahoma are from the north. This results in convergence in the vicinity of the convective arrow region. A westerly rear-inflow jet is also apparent behind the bow echo, as wind speeds in this location are slightly increased (from about 15 knots to 25-30 knots), compared to the surrounding winds. Additionally, warm air advection (WAA) is taking place behind the bow in central Texas, as winds are traveling from areas of warmer temperatures, into areas of cooler temperatures.

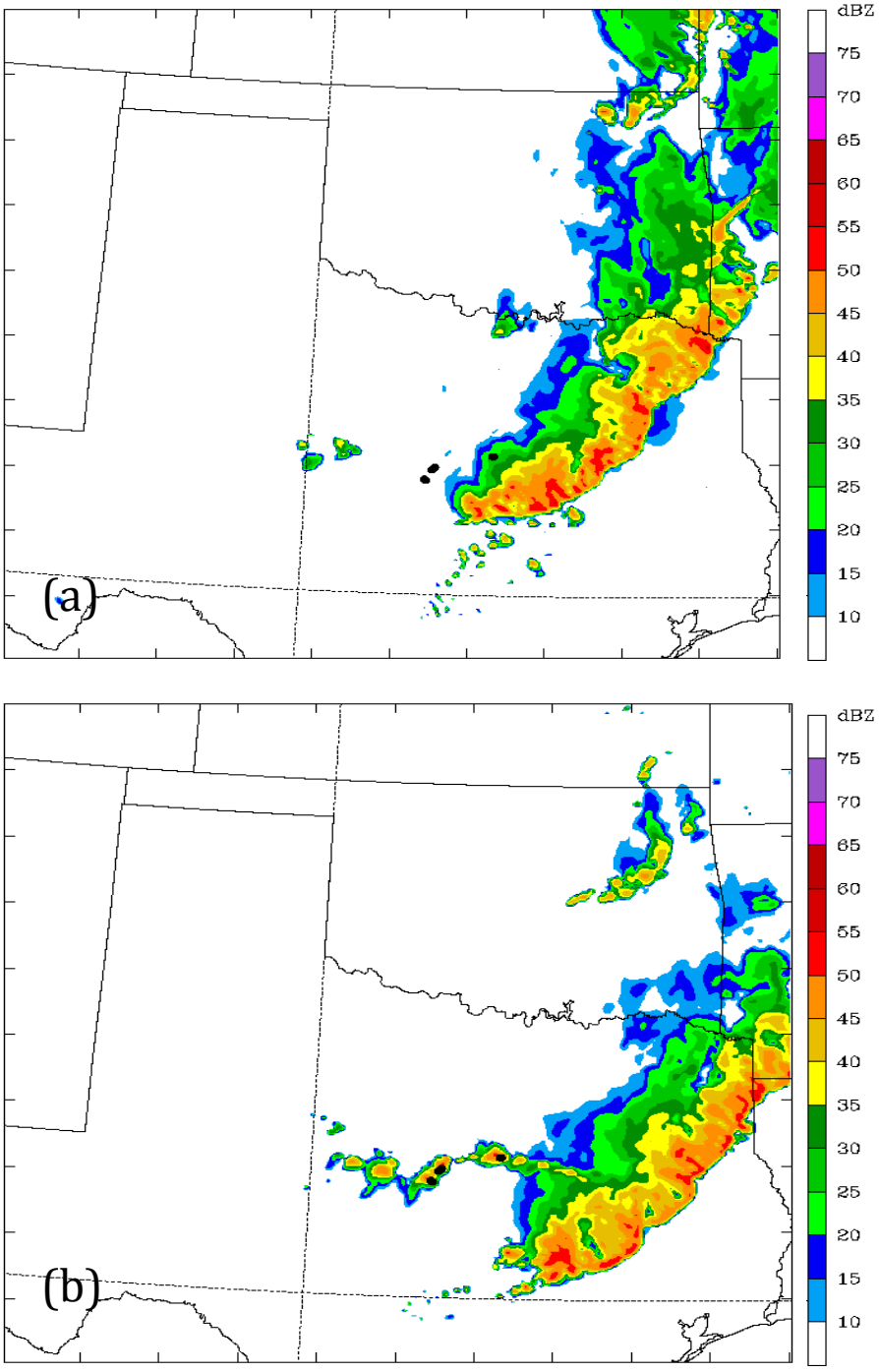


**Fig. 5.5.** Numerically simulated radar reflectivity, using WRF model output and the RIP4 program. (a) 0200 UTC 18 June 2006, and (b) 0400 UTC 18 June 2006. Color represents reflectivity in increments of 5 dBZ, and black bullets represents the location in which the greatest updrafts were found, in the final hour (0400 UTC).

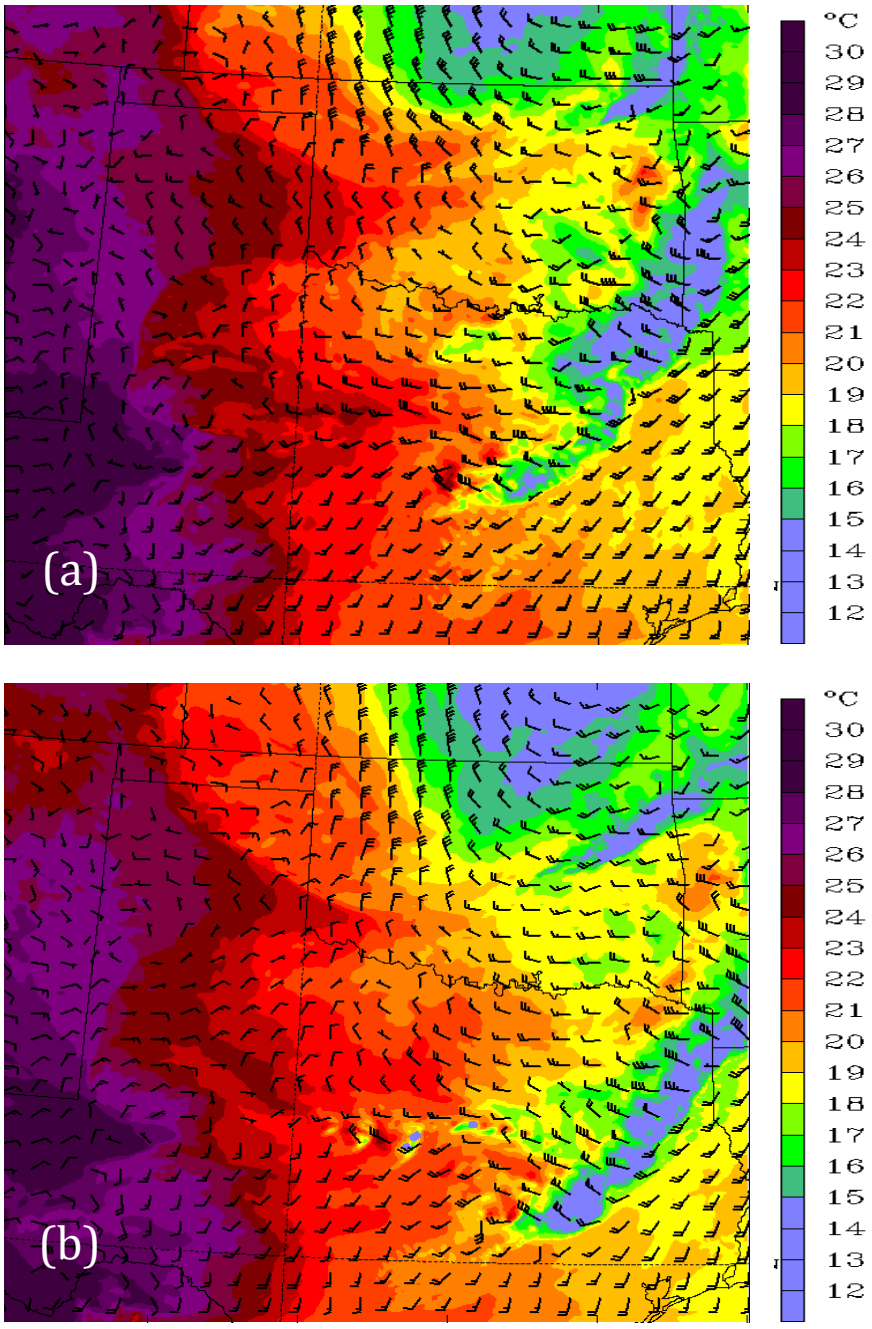


**Fig. 5.6.** Temperature and wind fields at the 850-hPa level. (a) 0200 UTC 18 June 2006, and (b) 0400 UTC 18 June 2006. Plots are created using WRF model output and the RIP4 program. Colors represent temperature (in increments of 1 degree C), while wind speed and direction is represented using wind barbs.

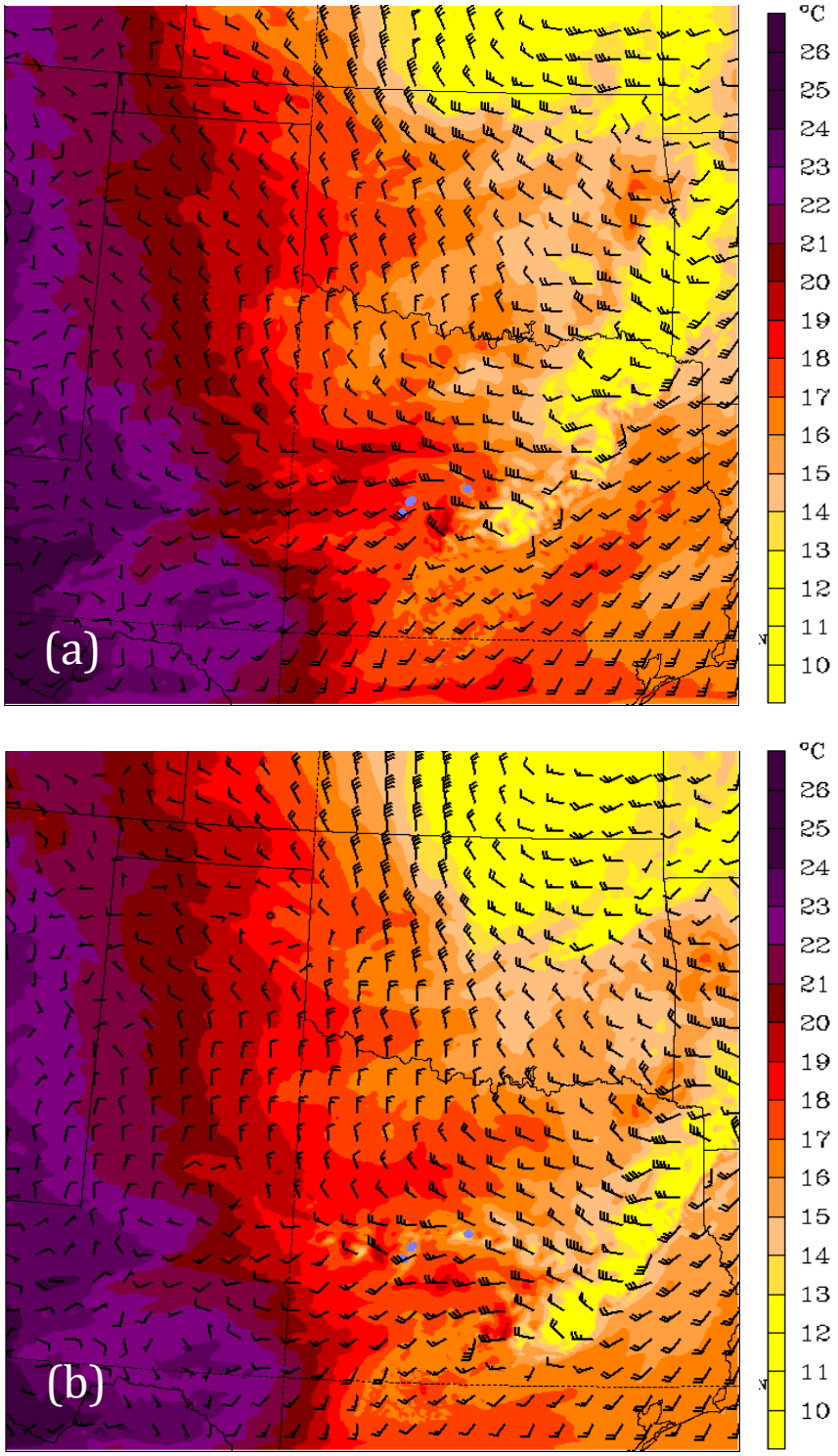


**Fig. 5.7.** Temperature and wind fields at the 800-hPa level. (a) 0200 UTC 18 June 2006, and (b) 0400 UTC 18 June 2006. Plots are created using WRF model output and the RIP4 program. Colors represent temperature (in increments of 1 degree C), while wind speed and direction is represented using wind barbs.

By 0400 UTC, Fig. 5.3 shows that all the parcels have converged into the areas of greatest updraft speed. Plotted on the 850-analysis for this time (Fig. 5.6b) are blue bullets to indicate these areas from which the trajectories are calculated, and where the updrafts are occurring. There are small areas of cooler temperature surrounding each updraft region. This is, most likely, due to the evaporatively-cooled outflow from the convective cells associated with the updrafts. On the eastern end of the convective arrow, winds are converging from the southwest and northwest, while they are converging from the south and north toward the western end of the line. Additionally, WAA is still evident at this time.

As shown in Fig. 5.4, several of the parcels begin their sharp ascent near the 800-hPa level. As mentioned above, at 0200 UTC, BGYB trajectories are southwesterly, turning westerly into the rear-inflow of the bow echo, while OBR parcels are primarily westerly at this point (Fig. 5.3), but also a part of the rear-inflow jet. Wind speeds in this general area are higher (25-30 knots), compared to the winds outside of the arrow region (which are about 10-15 knots). At this time, at the 800-hPa level (Fig. 5.7a) winds are still moving in from the southwest, and north-northwest, converging in the arrow vicinity, inducing WAA into the system. Although convergence is evident, it is not quite as prominent as it is at the 850-hPa level. Again, at 0400 UTC, the 800-hPa plot (Fig. 5.7b) shows the same wind direction, convergence, and WAA as at the 850-hPa level. Cooler temperatures are associated with outflow from the convective cells near the updraft regions;

however, as is expected, the temperatures are not quite as cool, compared to the ambient air, at this level.

As shown in Fig. 5.4, several parcels make a sharp ascent near the 700-hPa level within the final hour of the back-trajectory calculation. Analysis of this level (Fig. 5.8) is shown for only the last hour, since no parcels reach this level before this time. It appears that there is slight convergence of winds coming from the west-southwest, and those from the northwest, in the region of the updrafts. Shown in the top right corner of the figure is a magnified view of the area right around the updrafts. This increases the size of the wind barbs, showing evidence of fairly significant speed shear associated with convergence, where wind speeds from the west vary between 20 and 25-knots, while winds from the northwest are 30 to 35-knots. Temperature gradients in this area are tighter, resulting in stronger temperature advection as the winds cross the gradients.

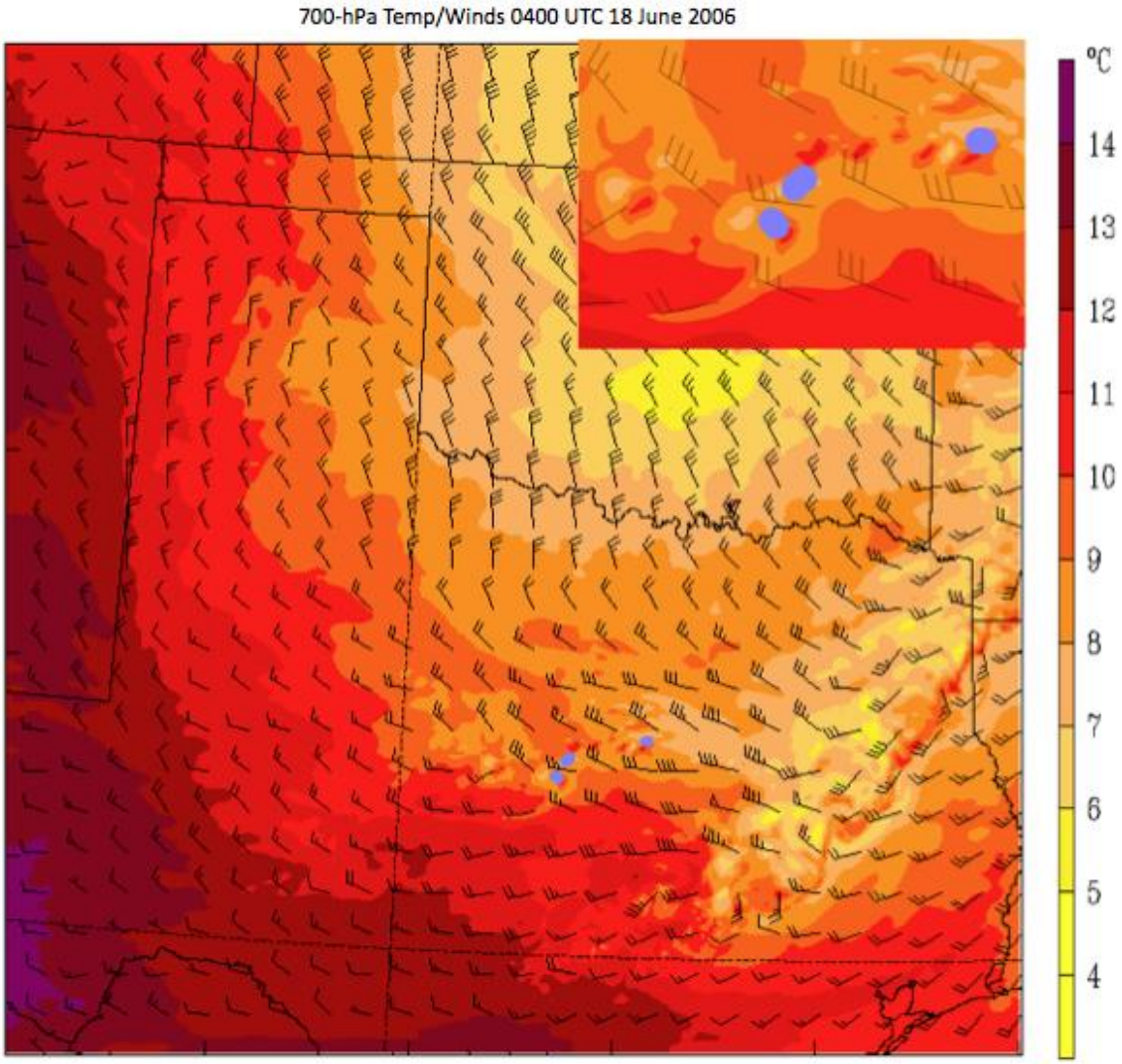


**Fig. 5.8.** Temperature and wind field at the 700-hPa level for 0400 UTC 18 June 2006. Plot is created using WRF model output and the RIP4 program. Colors represent temperature (in increments of 1 degree C), while wind speed and direction are represented by wind barbs. The top right corner shows a magnified image of the area close to the convective arrow region.

To obtain a perspective on the thermodynamic environment, a plot that shows a vertical cross-section of potential temperature, with an overlay of CAPE contours, is analyzed for 0400 UTC (Fig. 5.9b). Fig. 5.9a is the same XY-plane back-trajectory plot as shown previously, but with a solid black line drawn across the plane to indicate the exact location for the cross-section. There is evidence of both surface-based and elevated CAPE (close to 1500 J $kg^{-1}$), indicative of an unstable environment for air approaching from the southwest. Gradual isentropic lifting is illustrated, for parcels moving from the southwest to northeast, just above the surface. A cold pool is revealed near the surface on the right-hand side of Fig. 5.9b, while strong vertical motion is displayed as air approaches this cold pool. This is consistent with the findings of Trier et al. (2010) in which they used similar analyses to study the nocturnal cycle for warm season precipitation. They found that the most intense convection (associated with MCSs) occurred in areas where more gradual isentropic lifting was taking place above the cold pool below. Furthermore, they found sharper lifting that occurred far behind the cold pool edge, in areas where the LLJ and stable air under the frontal surface were contributing to the most intense convection in vertical cross-sections.

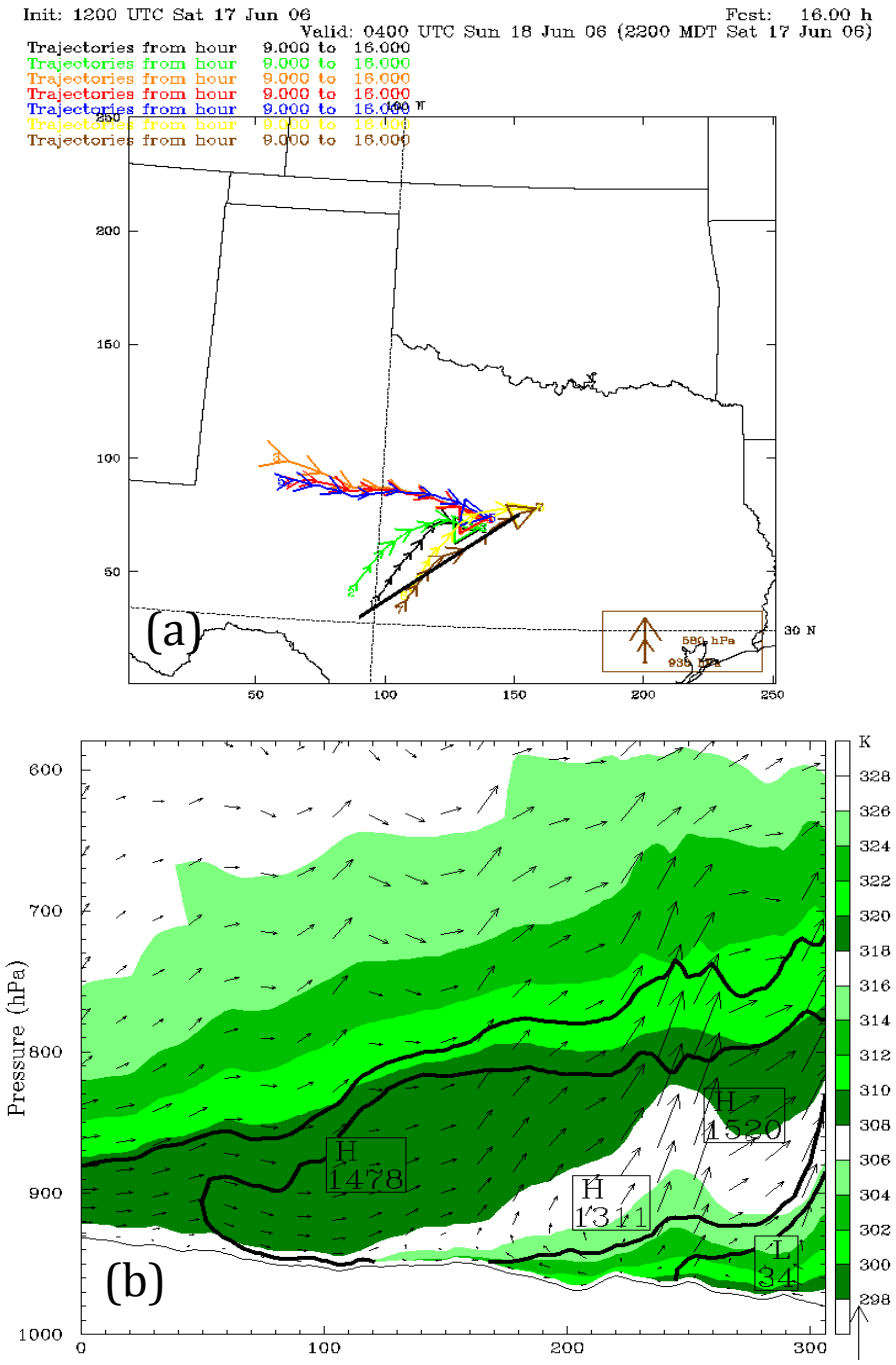


**Fig. 5.9.** (a) As in Fig. 5.3, but with a solid black line drawn over to indicate the location for the cross-section shown in 5.9b. Plots are created using WRF model output and the RIP4 program. (b) Cross-section of potential temperature (shades of green, in increments of 2 K), with an overlay of CAPE contours (solid black contours) 0400 UTC 18 June 2006. Wind speed and direction is given by arrows (the longer the arrow, the greater the wind speed). The X-axis represents horizontal distance, and the Z-axis represents pressure level (hPa).

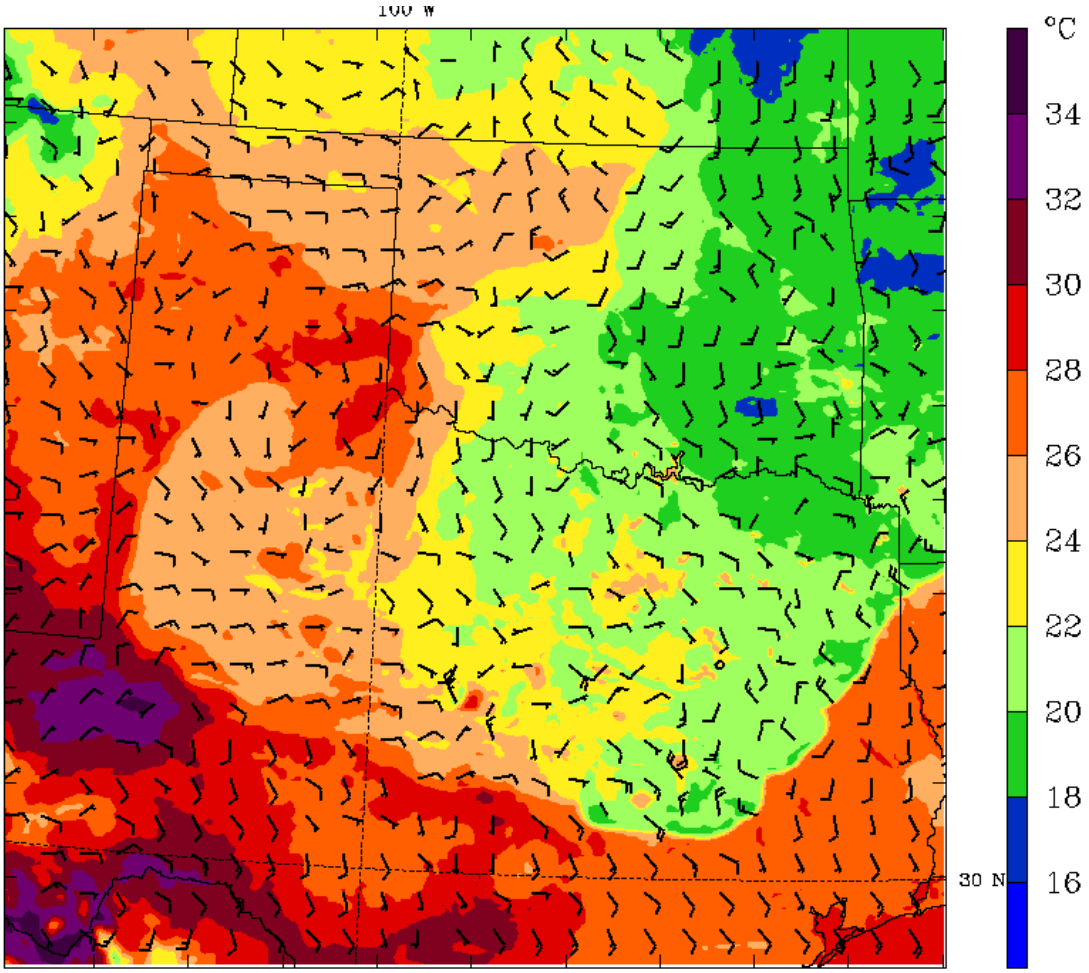


**Fig. 5.10.** Surface analysis for 0400 UTC 18 June 2006, where temperature is represented by colored contours (°C), and wind barbs give wind direction and speed (in knots).

Surface analysis has been provided for 0400 UTC (Fig. 5.10), as well, and clearly reveals the outflow boundary. This is located near the Texas-New Mexico border, and, on the figure, is shown where the light orange meets the dark orange. In addition to the strong temperature gradient, wind direction also changes at this location. Surface winds behind the bow echo are easterly as they approach the outflow boundary, and are northeasterly beyond the edge of the western side of the

boundary. When compared to Fig. 5.1b, it is clear that the convection in the arrow is not a result of lifting associated with that of the outflow boundary, as it is not occurring anywhere near the edge of the cold pool. Comparison of this figure to the observational surface analyses (Fig. 4.13 and Fig. 4.14) shows consistency, as they all show winds out of the south (or southeast) approaching the system, and an outflow region (behind the bow echo) with cooler temperatures (between 20°C and 24°C , as opposed to surrounding air, which is from 26°C to 30°C ), portraying the cold pool. In the observational analyses, as mentioned before, however, the resolution is coarse and, therefore, the boundary is not quite as clear as in the simulated analysis.

MUCAPE is analyzed in an attempt to solidify thermodynamic conclusions. Black bullet points are plotted on top of the figures to show the areas of greatest updraft. At 0100 UTC (Fig. 5.11a), the bow echo has just passed through the region, removing all CAPE due to overturning of air, in addition to evaporative cooling of descending air in the outflow from the bow. By 0200 UTC (Fig. 5.11b), the bow echo is further to the southeast, and MUCAPE has returned, with a value between 1500 and 2000 J $kg^{-1}$ for the two updraft locations farthest west. The third location is still too close to the bow echo outflow to acquire enough instability by this time, but returns just prior to convection initiation (not shown). This CAPE value is comparable to the value given by the potential temperature/CAPE cross-sections, discussed above.

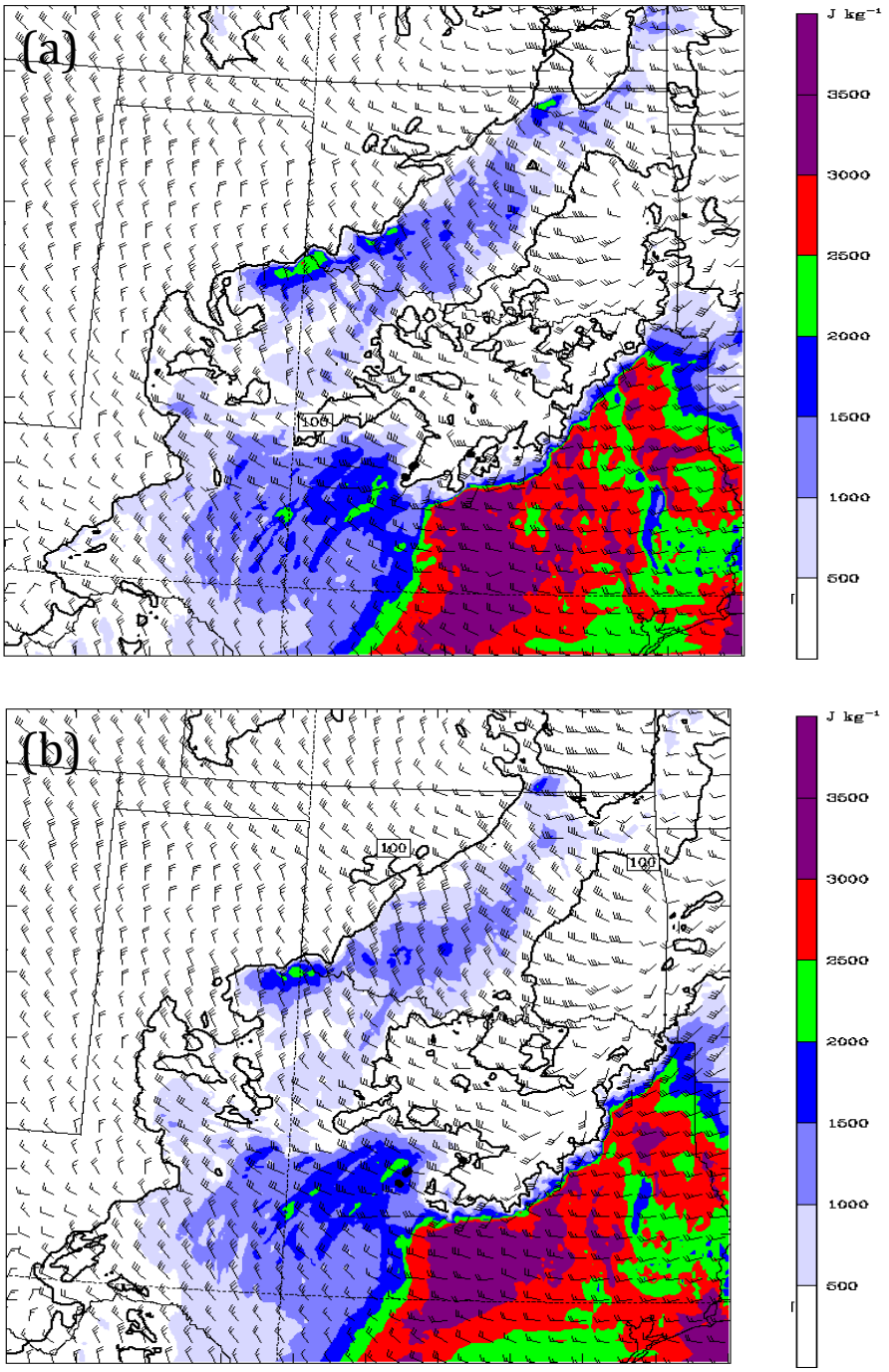


**Fig. 5.11.** Most unstable CAPE shown for (a) 0100 UTC, and (b) 0200 UTC, 18 June 2006. Colors represent values of CAPE in increments of 500 J kg$^{-1}$. Solid black contours represent boundaries for areas with no CAPE. Wind barbs express 0-6-km wind shear. This plot was created using WRF model output and the RIP4 program.

Based on mesoscale analysis from the model output, it seems that several factors may be contributing to the bow and arrow phenomenon in this case. At all the layers studied, there is evidence of convergence of winds coming from both the southwest and northwest, in the area in which the arrow forms. There is also indication of higher winds in the arrow region, possibly resulting from the rear-inflow jet into the bow echo. Furthermore, there appears to be horizontal speed shear, which can cause deformation of the flow. This, combined with the increased rear-inflow jet wind speeds may be contributing to the linear orientation of the arrow. Additionally, although much of the instability is removed from the region, with the passing of the bow echo, CAPE values begin to increase somewhat prior to convection initiation in the arrow region, as winds from the south are bringing moist air into the region, creating moisture advection, and increased instability. Finally, WAA is evident across the region, and into the area of the convective arrow. This creates gradual isentropic lifting, prior to the strong updrafts in the unstable environment.

## 5.2 08 May 2009 Event

The times for which a bow and arrow is evident on observed radar reflectivity for this event are from 1500 UTC until around 1900 UTC, at which point the convective arrow loses its linear organization and detaches from the rest of the system that moves off to the northeast. The timing of the simulation (Fig. 5.12b) is

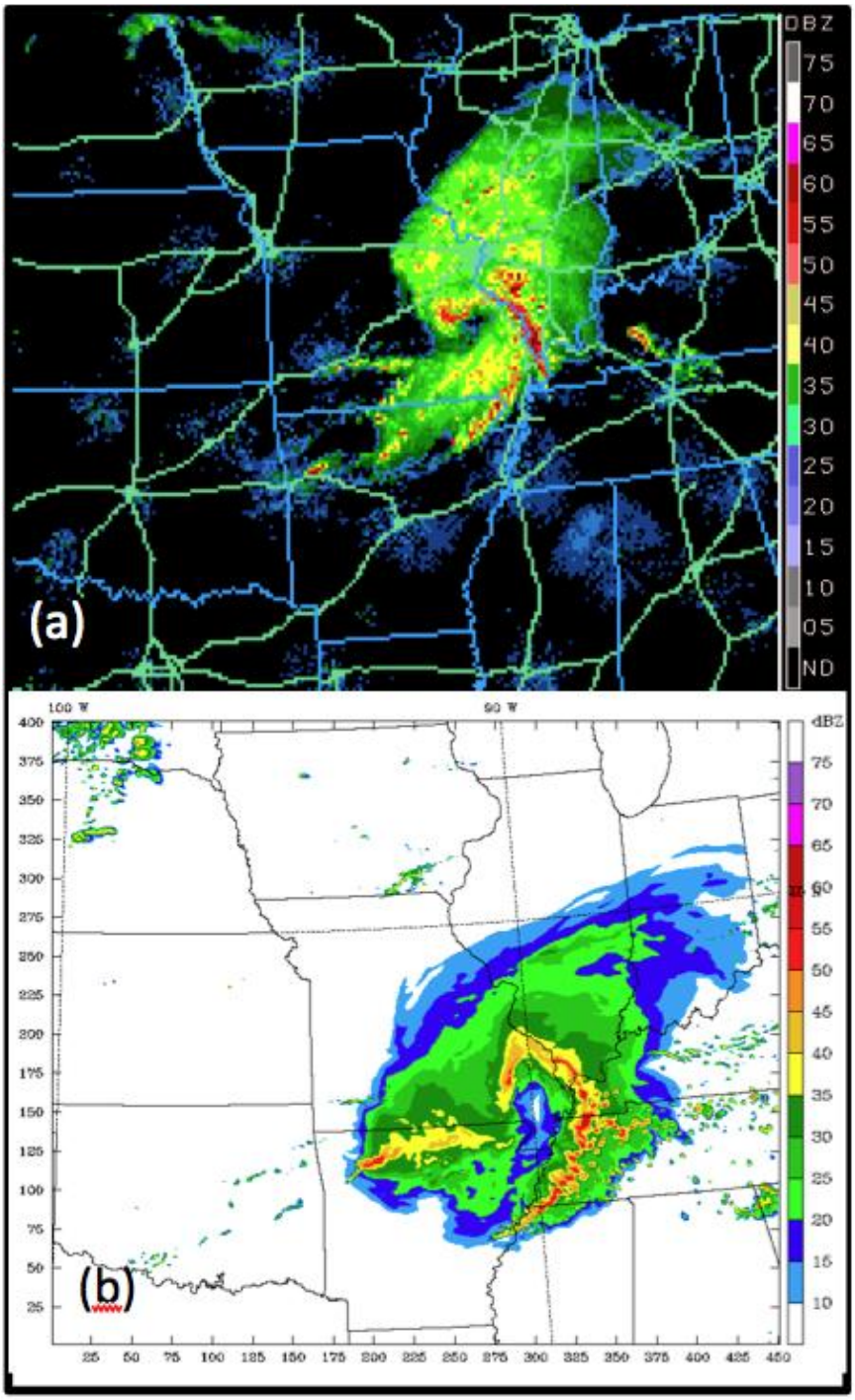


**Fig. 5.12.** Comparison of (a) real-time radar reflectivity 1626 UTC 08 May 2009 (from NCAR's MMM Image Archive), and (b) WRF numerically simulated radar reflectivity 1630 UTC 08 May 2009. Color represents reflectivity in increments of 5 dBZ.

nearly identical to the timing of the actual event (Fig. 5.12a), as is the shape and orientation of the entire system. The primary difference between them is the location of the system, which is shifted slightly to the south in the simulated image. This causes the arrow to take place in northern Arkansas instead of southern Missouri.

As in the previous case, back-trajectories are calculated starting at the location of greatest updraft. The same strategy is used with this case—using a vertical motion plot to find the updraft locations. The strongest updraft for this case is found at the 550-hPa level at 1445 UTC, with vertical velocities in excess of 320 dPa $s^{-1}$. Using this information, back-trajectories are calculated from 1445 UTC back to 0800 UTC.

The back-trajectories in the XY-plane (Fig. 5.13) show that all the parcels originate out of the southwest, moving toward the northeast, into the very northwest region of Arkansas by the end of the period. Arrowed notches on the trajectories increase in size over time, indicating that parcels are rising. The trajectory plot for the XZ-plane (Fig. 5.14) shows that all trajectories essentially take the same vertical path, although some of them begin at a different level. Three of the trajectories start just below the 850-hPa level, gradually rising, before they ascend sharply to a level near the 700-hPa level. This takes place between 1100 UTC and 1200 UTC. The remaining four trajectories start slightly lower, near the 900-hPa level, but rise rapidly at the same time to levels between 750-hPa and 700-hPa. Between 1200 UTC, and shortly after 1400 UTC, they fluctuate very slightly

through pressure levels, but basically maintain their vertical position around 700-hPa, before they make their final sharp ascent, sometime between 1400 UTC and 1445 UTC, into the strong updraft region.

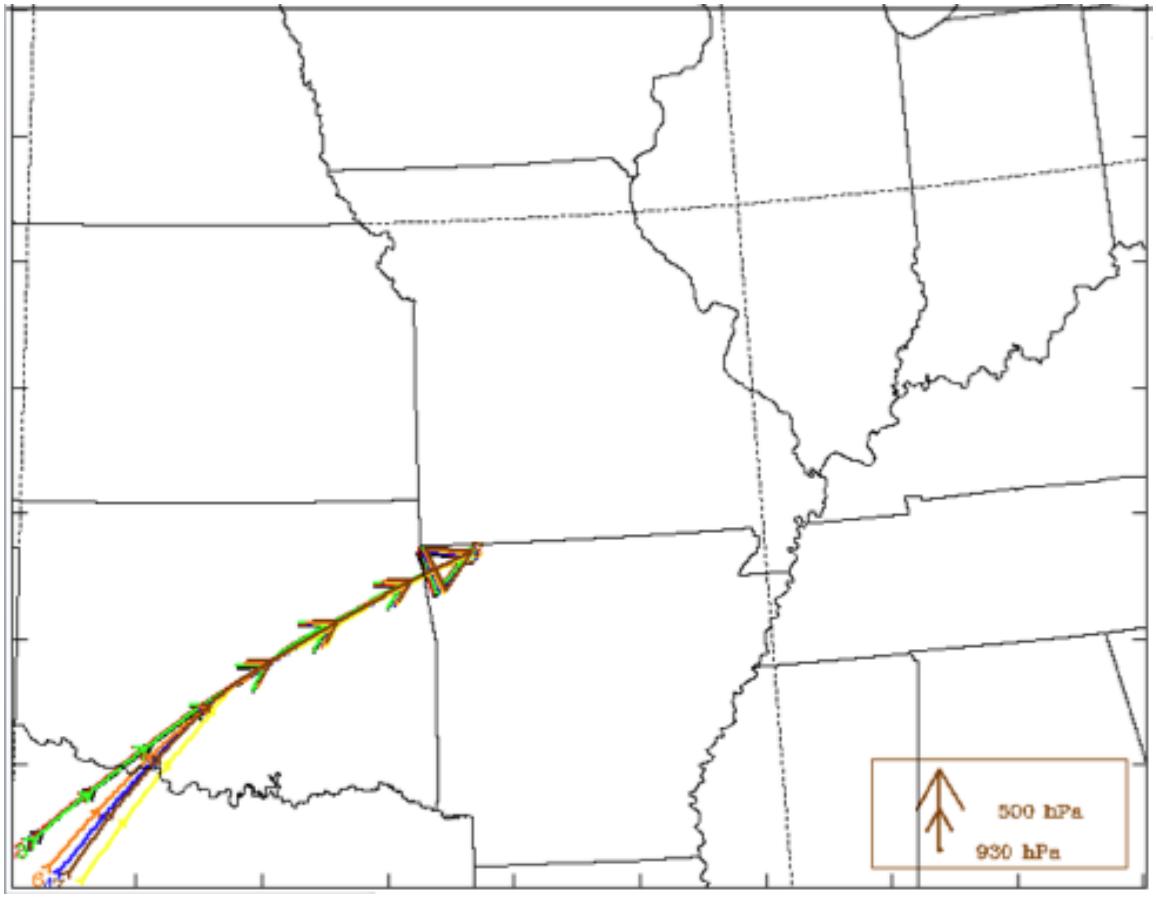


**Fig. 5.13.** As in Fig. 5.3, but for 1445 UTC, back to 0800 UTC 08 May 2009.

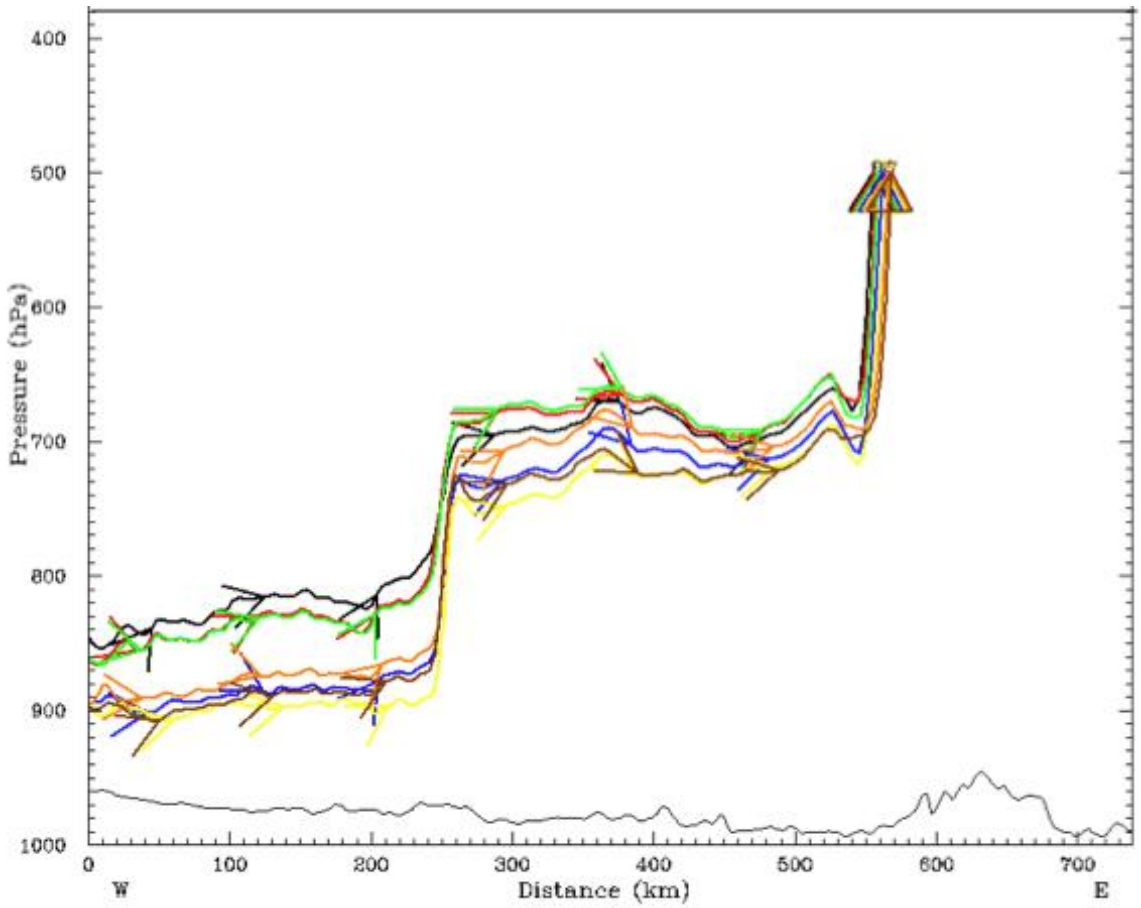


**Fig. 5.14.** As in Fig. 5.4, but for 1445 UTC, back to 0800 UTC 08 May 2009.

In order to analyze the cause of the vertical motion of parcels, various plots are examined at different pressure levels. The first two plots that are analyzed are the 900-hPa and 850-hPa plots, since the parcels all begin somewhere around these two levels. The 900-hPa plot (Fig. 5.15a) is from 1150 UTC. A blue bullet point is plotted to indicate the area in which the trajectory parcels are at that time, just before they are sharply lifted for the first time. It is evident that air is coming out of the southwest, and that the bullet is located just at the edge of the cold pool region, which has much cooler temperatures, behind the bow echo. It is, therefore,

assumed that the cold pool serves as a boundary that induces lifting of the parcels. The 850-hPa analysis (Fig. 5.15b) basically shows the same scenario at this time. Winds, again, are coming from the southwest, intercepting the boundary created by the cold pool. At this level, it is evident there is a strong LLJ, as wind speeds are as high as 50 knots. Some of the parcels rise at the 800-hPa level; however, this analysis is not shown because it portrays information that is repetitive of that shown in Fig. 5.15.

850-hPa analysis is shown for 1445 UTC (Fig. 5.16a). At this time, there is still evidence of a strong LLJ, with winds coming out of the southwest. It also appears that winds north of the arrow region are coming from the northern bookend vortex of the bow echo. The winds start from the east, wrapping around, becoming northerly, then westerly into the rear-inflow region behind the bow. These winds are creating convergence with the ambient southwesterly winds. Additionally, the winds in the rear-inflow region are faster (35-40 knots) than the surrounding winds (15-20 knots), indicative of the rear-inflow jet. There is also a narrow band of higher temperatures and lower wind speeds that extends from central Oklahoma, into the west side of the arrow region. It is unclear, however, what is causing this, or how it is related. Fig. 5.16b shows the 850-hPa wind speed analysis, where greater wind speeds are shown by darker colors. This shows a distinct line of faster winds in the location of the arrow region, indicating horizontal speed shear, and potentially the rear-inflow jet.

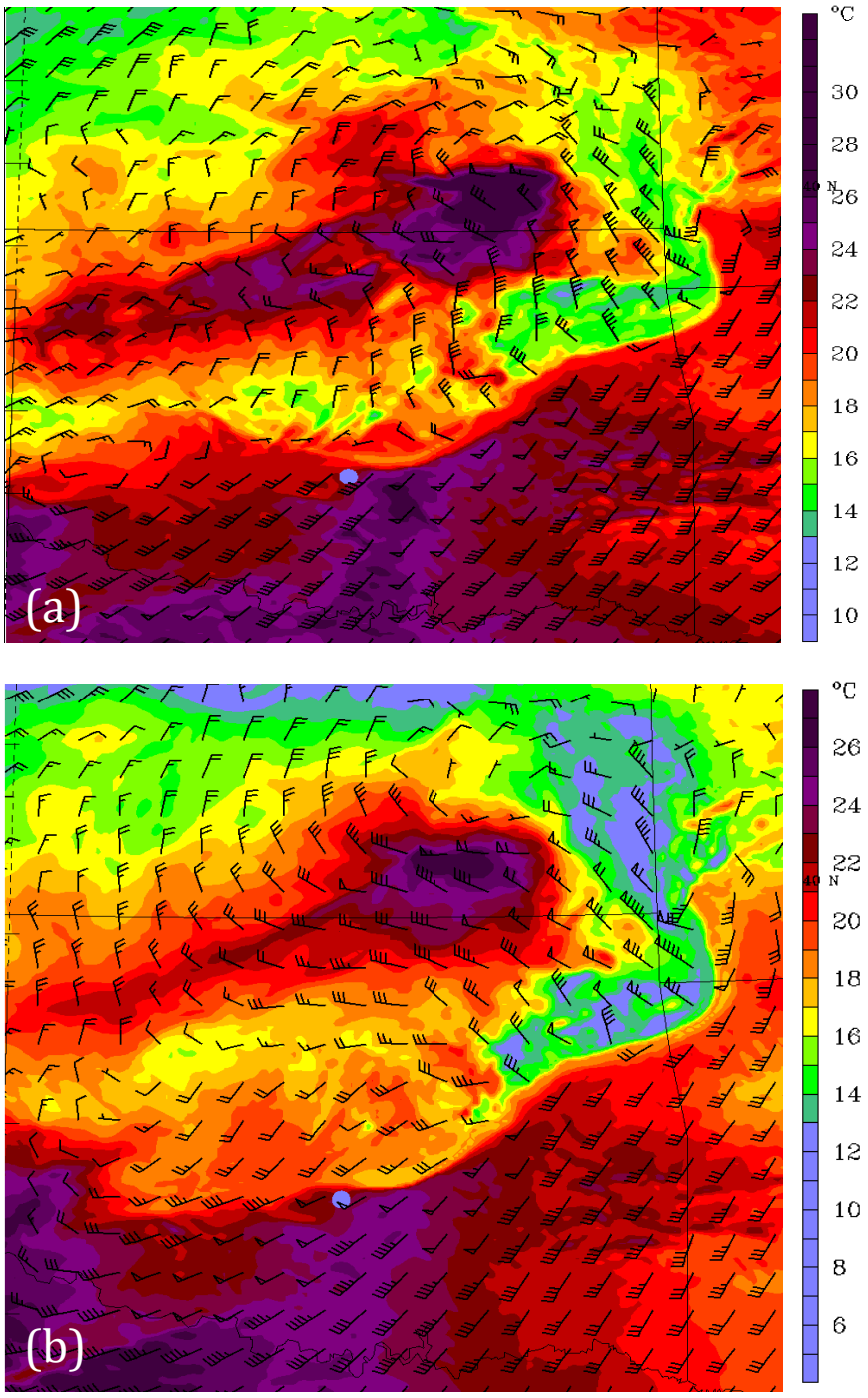


**Fig. 5.15.** Temperature and wind fields for 1150 UTC 08 May 2009 at the (a) 900-hPa level, and (b) 850-hPa level. Plot is created using WRF model output and the RIP4 program. Colors represent temperature (in increments of 1 degree C), while wind speed and direction are represented by wind barbs.

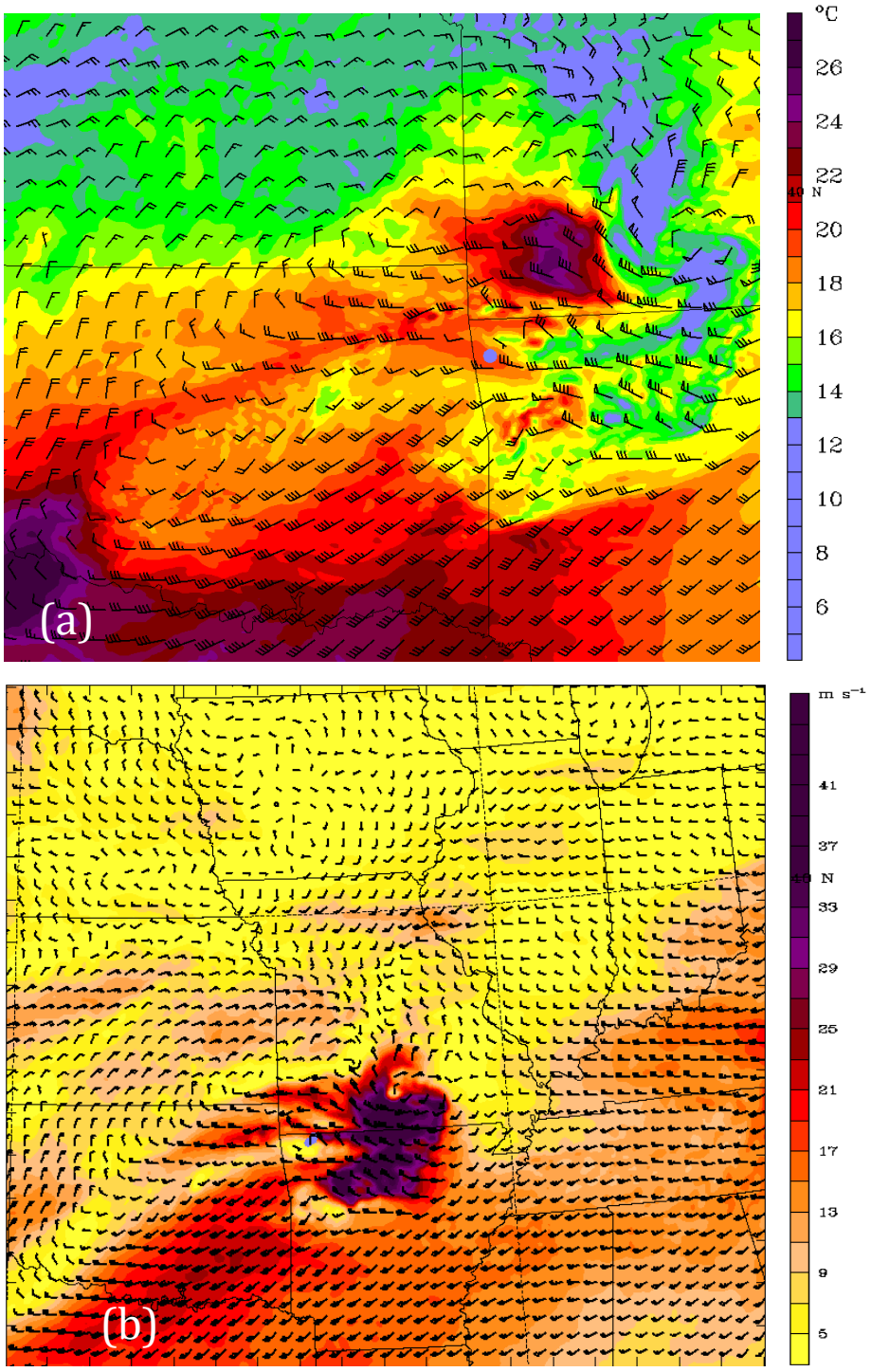


**Fig. 5.16.** (a) As in Fig. 5.15a, but for 1445 UTC 08 May 2009, and (b) 850-hPa wind speed analysis. Colors represent wind speeds in increments of 2 m $s^{-1}$. Plot is created using WRF model output and the RIP4 program.

700-hPa analyses are shown for 1400 UTC (Fig. 5.17a) and for 1445 UTC (Fig. 5.17b) since the parcels take their final ascent into the updraft region sometime between these two times. Both of these analyses are similar in that they both show that WAA is taking place over the region and into the convective arrow region. There is a large area of warmer air over Oklahoma. As southwesterly winds are moving into the arrow region, they are bringing that warm air with them. Additionally, there is evidence of convergence, as winds are coming out of the southwest, and the west-northwest, and meeting in the area in which the arrow is formed. There is also a fairly significant amount of speed shear in this area, especially at 1400 UTC, where winds from the southwest are 70-75 knots, while winds to the north of the arrow are 55-60 knots. By 1445 UTC, there is evidence of cooler temperatures just behind the updraft region, as is expected from the outflow from the convective cell.

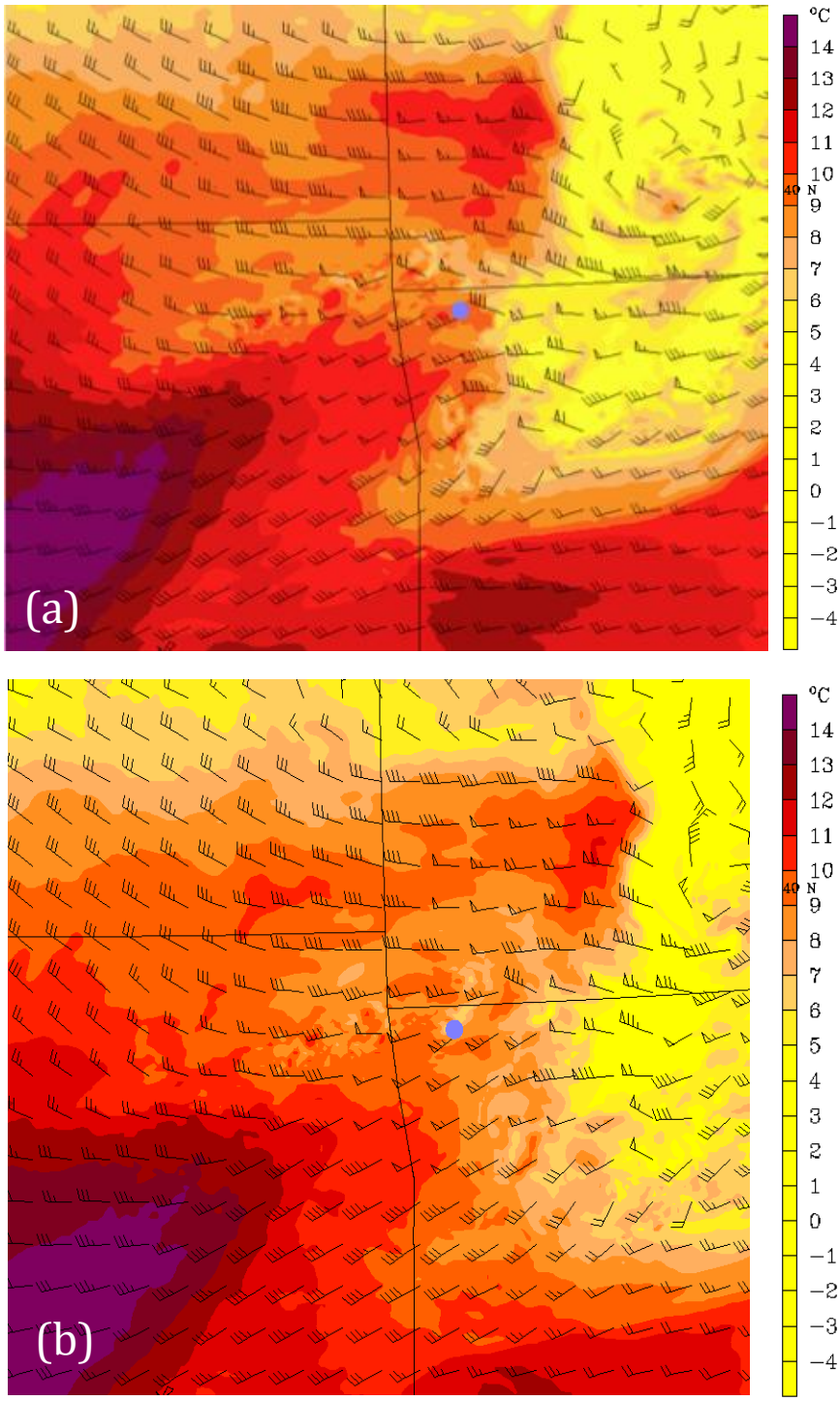


**Fig. 5.17.** As in Fig. 5.8, but for (a) 1400 UTC 08 May 2009, and (b) 1445 UTC 08 May 2009.

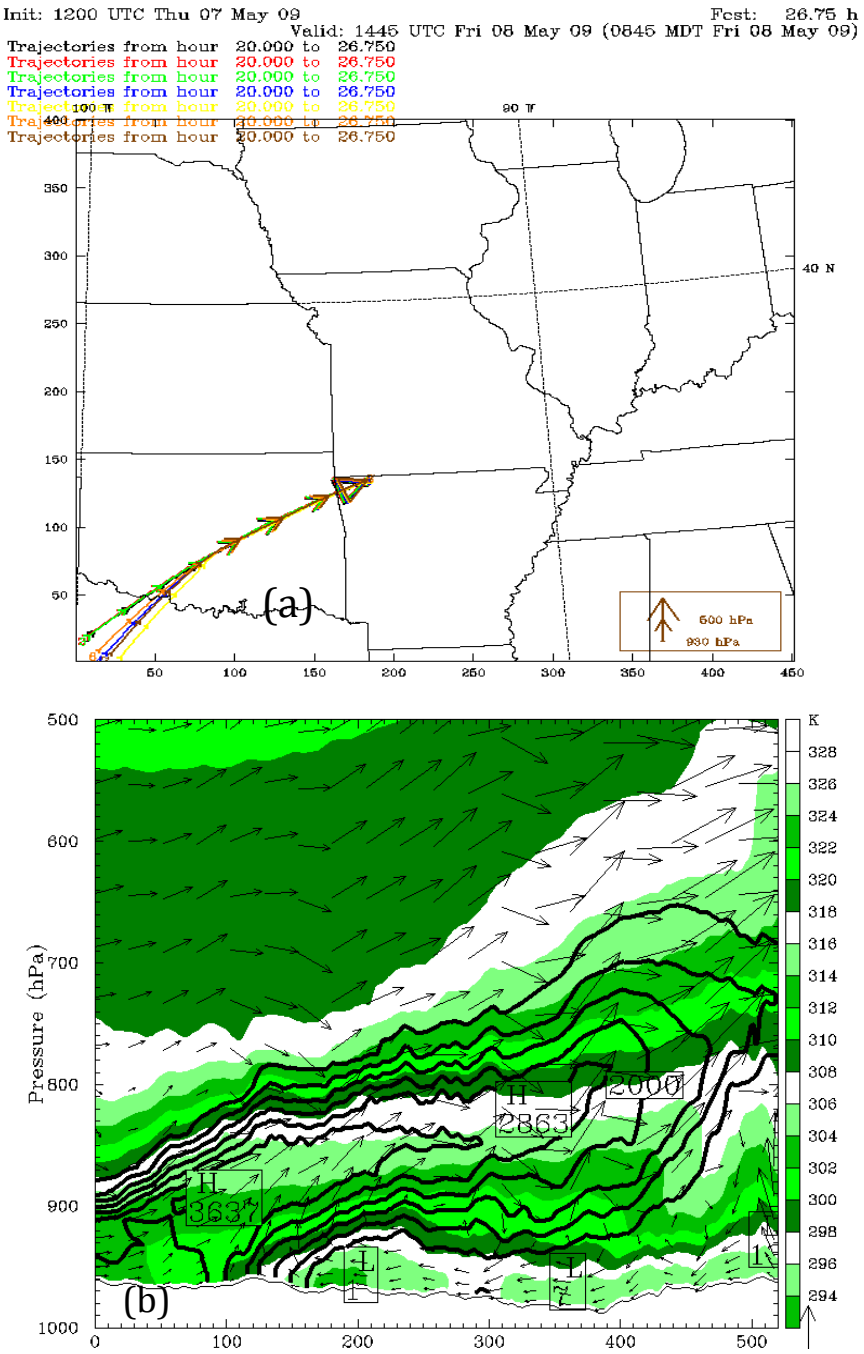


**Fig. 5.18.** (a) As in Fig. 5.13, but with a solid black line drawn across the trajectories to represent the location of the cross-section in 5.17b. (b) As in Fig. 5.9b, but at 1400 UTC 08 May 2009.

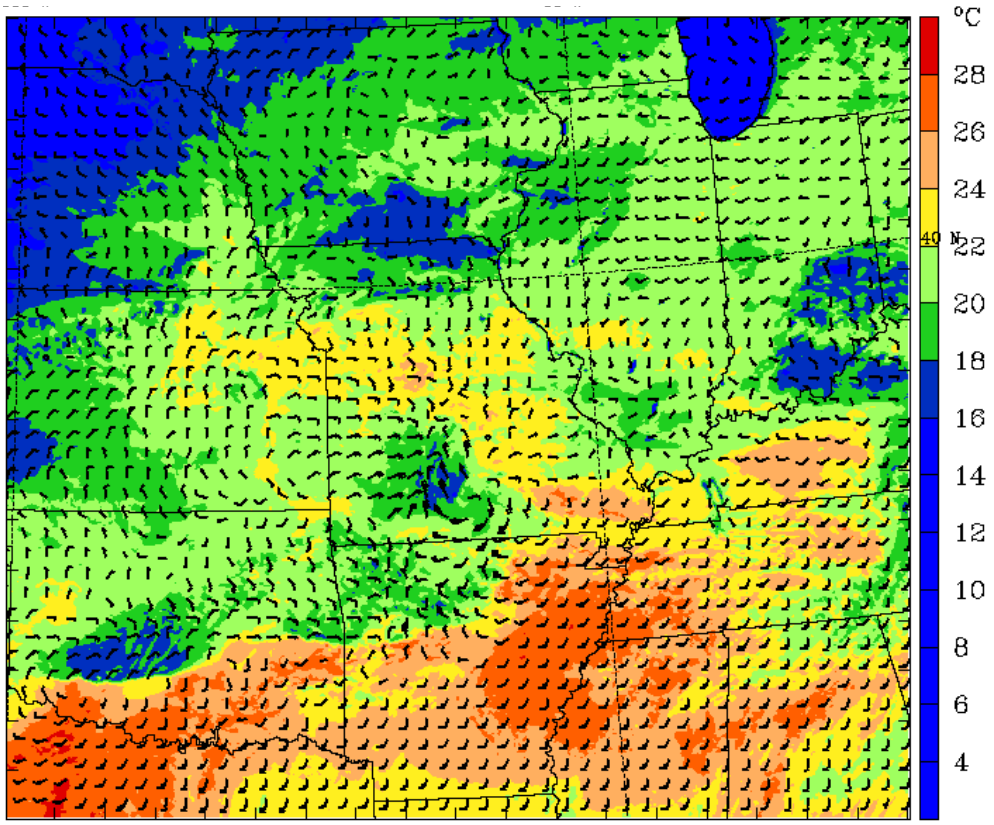


**Fig. 5.19.** Surface analysis from 1400 UTC 08 May 2009, where temperature is represented by colored contours (°C), and wind barbs give direction and speed of winds (in knots).

For thermodynamic examination of the area, the same analyses are conducted, as in the previous case study. The potential temperature plot, with an overlay of CAPE contours is shown in Fig. 5.18b, for 1400 UTC. Fig. 5.18a shows the XY-plane back-trajectory plot, with a solid black line drawn to reference the location of the cross-section. From this analysis, it is evident that there is no CAPE for surface-based parcels, but there is a great amount of instability (values > 3500 J $kg^{-1}$ over south-central Oklahoma) for elevated parcels, where lifting begins. In addition, it demonstrates gradual isentropic lifting, and then sharp lifting in the

area of strong updraft. Additionally, surface analysis at this time (Fig. 5.19) is shown, and shows that the edge of the cold pool extends much farther west of the area in which the strongest vertical motion appears, indicating that the outflow boundary is not responsible for the strong lifting taking place in the arrow region. Again the observational surface analyses (Figs. 4.21 and 4.22) are comparable to the simulated analysis shown here. They all show temperatures between 15°C and 24°C in the outflow region, indicating the presence of a cold pool, where the surrounding temperatures are near 30°C, and the winds to the south of the system are all out of the south-southwest.

MUCAPE for 1400 UTC is shown in Fig. 5.20. The area of greatest updraft is represented by the cluster of black bullets. Just prior to this time, this area is in the cold pool region of the bow echo, and therefore there is no CAPE. At this time, CAPE values are increased in this area to somewhere between 1000 and 1500 J $kg^{-1}$, increasing to values > 3500 J $kg^{-1}$ toward the southwest, into central Oklahoma. Although the CAPE values in the arrow region are not a substantial amount, it still indicates increased instability in the area.

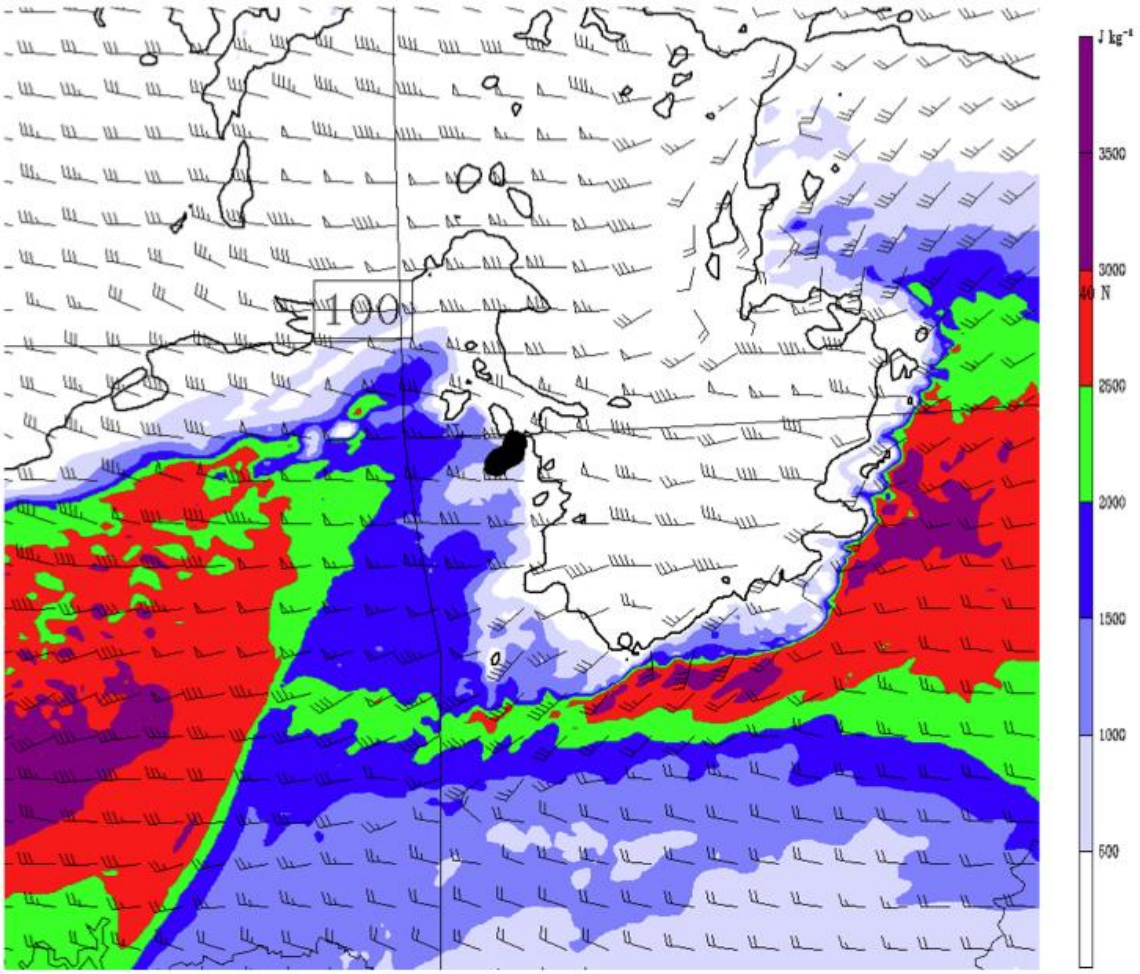


**Fig. 5.20.** As in Fig. 5.11, but for 1400 UTC 08 May 2009.

Several ingredients for lifting are evident in this analysis. As in the previous case, there is convergence of winds out of the southwest and northwest at all levels, (although in the previous case, the northwest winds do not appear to be related to a bookend vortex). In addition to confluence, there is also speed convergence in the arrow region. WAA is evident throughout the region, and into the location of the convective arrow, which explains the gradual isentropic lifting, shown on the potential temperature plot. The faster wind speeds in the arrow region could be

due to the rear-inflow jet, and could possibly explain the orientation of the convective arrow. Finally, although the CAPE values are not extremely high in the region of the convective arrow, the environment is still somewhat unstable, making the parcels vulnerable to the strong updraft at the end of the period.

### 5.3 15 September 2010 Event

The bow and arrow event on this day took place in three different phases, as was discussed in section 4.1.4.; however, the model simulation of this event only occurs in one phase, which is similar to the third phase discussed earlier. Fig. 5.21a shows observed radar reflectivity at 1926 UTC, while the simulated radar image is shown for 1700 UTC (Fig. 5.21b). It is apparent that the overall orientation of the system is the same, although the location is different. The arrow formed in the observed case around 1600 UTC, in southeast Nebraska and northeast Kansas. It traveled toward the southwest through central and southern Missouri before losing organization around 2250 UTC. The simulated event also shows the first cells in the convective arrow around 1600 UTC; however, it begins near the Nebraska, Iowa, and Missouri intersection, with the bow echo region extending from northeast Kansas, through the northwest corner of Missouri, and into southwest Iowa. It also propagates toward the southeast, but remains in northern and central Missouri, and loses organization around 2045 UTC.

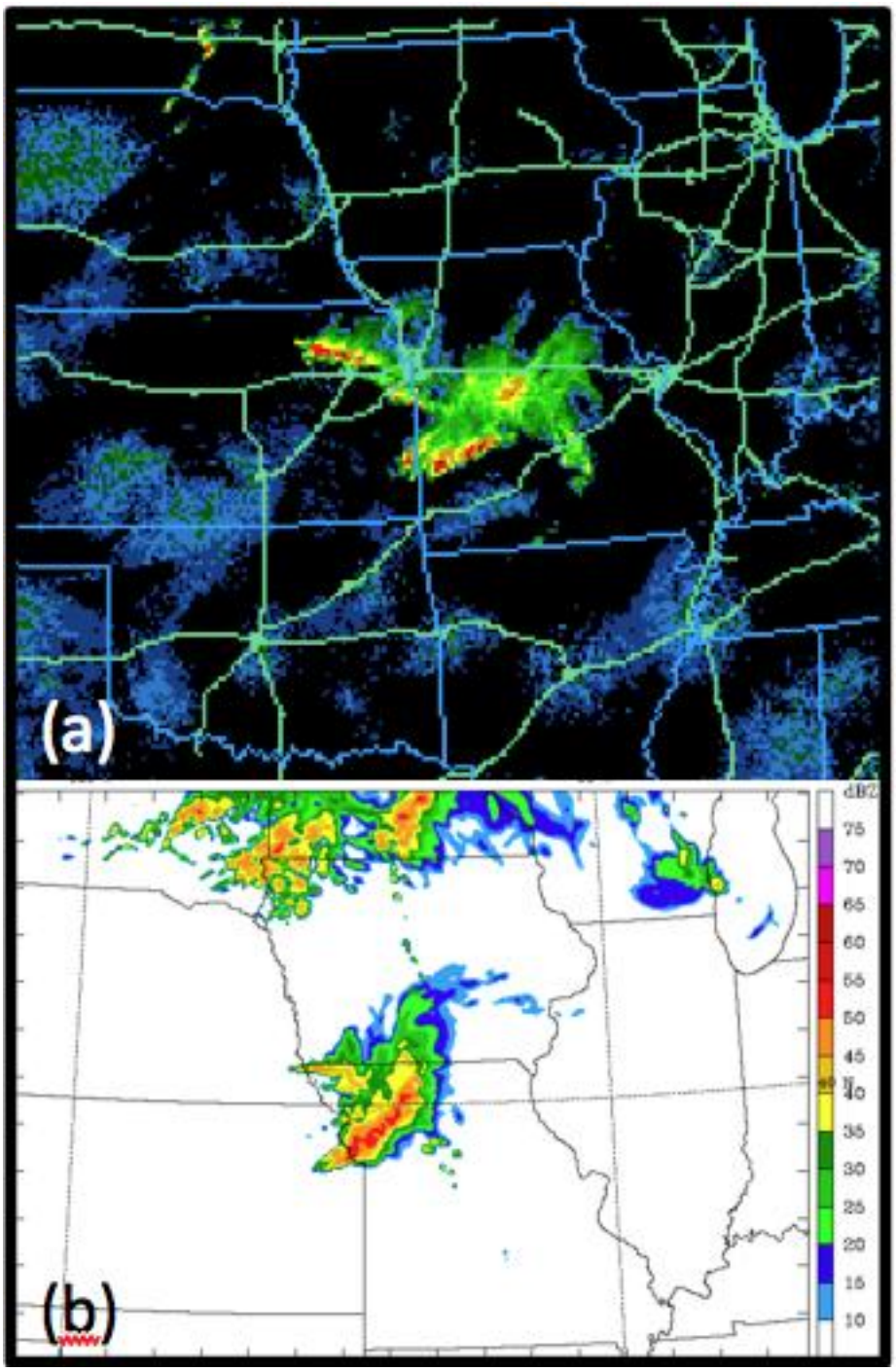


**Fig. 5.21.** Comparison of (a) real-time radar reflectivity 1926 UTC 15 September 2010 (from NCAR's MMM Image Archive), and (b) WRF numerically simulated radar reflectivity 1700 UTC 15 September 2010. Color represents reflectivity in increments of 5 dBZ.

Using vertical motion plots, it is determined that the time the updraft speed is the greatest is at 1700 UTC (with vertical speeds of 180-200 dPa $s^{-1}$) at the 550-hPa level. Back-trajectories are therefore calculated from this time, back to 0900 UTC. The XY-plane trajectory plot (Fig. 5.22) shows all of the parcels originating out of the southwest, and flowing toward the northeast, curving toward the east in the final 2-3 hours. As indicated previously, the size of the arrows depicts the elevation of the parcels (the larger the arrow, the higher the parcel is in the atmosphere). The arrowed notches on these trajectories slightly increase with size, over time, indicating that the parcels are gradually rising.

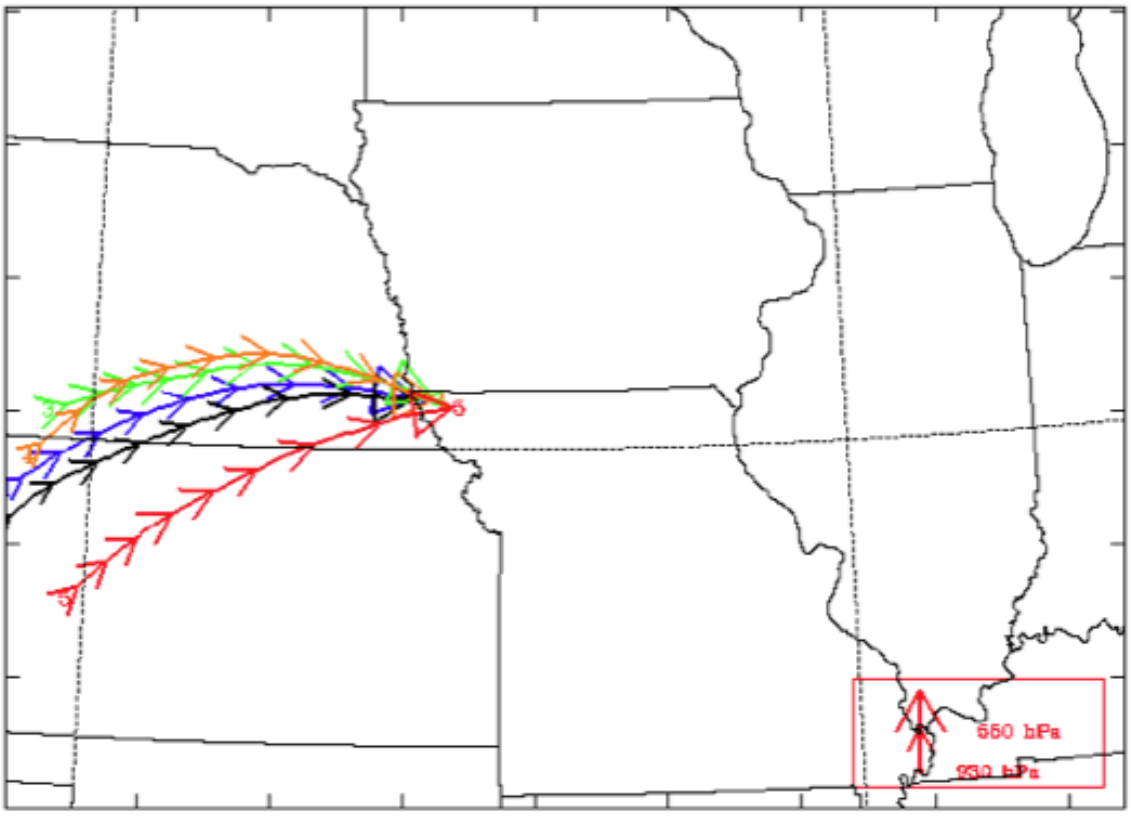


**Fig. 5.22.** As in Fig. 5.3, but for 1700 UTC, back to 0900 UTC 15 September 2010.

The XZ-plane trajectory plots (Fig. 5.23) solidifies the previous assumption that the parcels are gradually lifting with time. The parcels all start out somewhere between the 800-hPa and 700-hPa levels at 0900 UTC. From there, they gradually rise, before sharply lifting between 1600 UTC and 1700 UTC, between the 700 and 650-hPa levels.

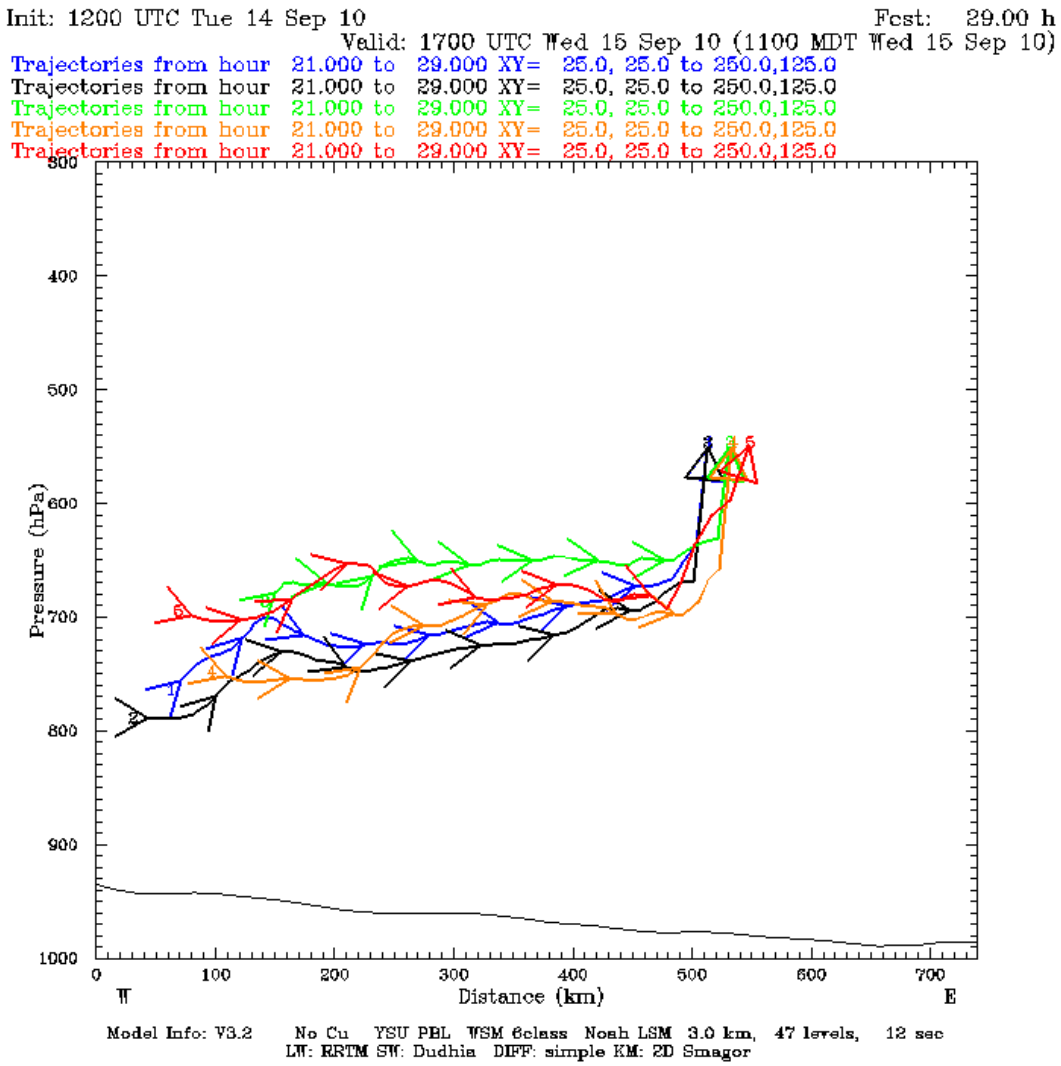


**Fig. 5.23.** As in Fig. 5.4, but for 1700 UTC, back to 0900 UTC 15 September 2010.

Although none of the parcels appear at the 850-hPa level in Fig. 5.23, it is still of interest to examine, especially since the LLJ, which is responsible for increasing instability at higher latitudes, is typically apparent at this level. The 850-hPa plot for 1700 UTC (Fig. 5.24a) shows a scenario that is similar to the other cases. Again, blue bullets have been placed in the location of the strongest updrafts. There is evidence of strong southwesterly flow, (most likely an indication of the LLJ), that turns westerly, and then northwesterly into the region of the convective arrow. The wind speeds in the arrow region are slightly stronger, possibly displaying evidence of a rear-inflow jet. To further illustrate these winds changes, 850-hPa isotachs are shown in Fig. 5.24b. Although the increased winds in the arrow region are not nearly as profound as the 08 May 2009 case, the evidence still exists in this case, as winds are increased from about 14 m $s^{-1}$ in the areas surrounding the arrow, to around 20 m $s^{-1}$ for the region where the arrow is found, again showing that the arrow forms along a strong wind speed gradient, as in the previous cases. This horizontal wind shear begins to develop about an hour prior to this (1600 UTC; not shown), after the bow echo passes through. Due to the strong southwesterly winds, WAA is taking place as winds carry warmer air from the south into the arrow region where temperatures are cooler. The difference in this analysis and the two previous cases is that, at this level, there is no evidence of winds coming from the northwest, or west, to converge with the southwesterly winds. The only confluence seems to take place where southwesterly flow intercepts the possible rear-inflow jet.

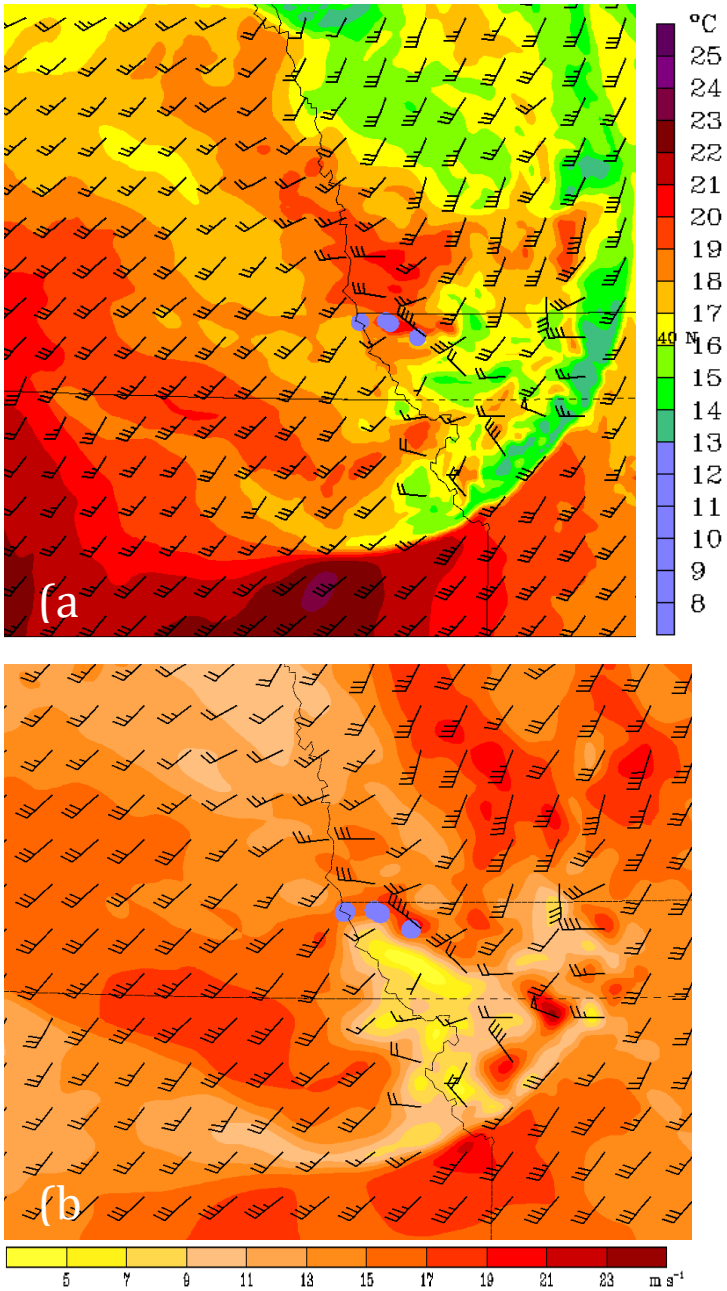


**Fig. 5.24.** As in Fig. 5.16, but for 1700 UTC 15 September 2010.

The 800-hPa level is analyzed at two different times. At 1100 UTC (Fig. 5.25a), the bow echo has not passed through the region where the convective arrow later occurs; however, there is still evidence of strong southwesterly winds at this level, creating strong WAA. By 1700 (Fig. 5.25b), the bow has passed through, and winds are still strong, out of the southwest. At this time, however, the winds to the north of the region shift and become westerly, possibly as a result of the rear-inflow jet, into the bow echo. Therefore convergence is occurring as the southwest winds are converging with the westerly winds. Additionally, slight speed shear is evident, as winds out of the southwest have speeds of 30-40 knots, while winds from the west are only 25-30 knots.

As mentioned earlier, all the parcels appear to rise abruptly near the 700-hPa level within the last hour of the back-trajectory calculation. Analysis of this layer is shown in Fig. 5.26. This figure is from 1645 UTC, which is just prior to the final time. Again, there is strong southwesterly flow at this level, creating WAA. There is also strong westerly flow in (and north of) the inflow region, into the bow. The winds from the southwest (which have speeds of 40-45 knots) are intersecting with the westerly and northwesterly winds (with speeds from 25-30 knots), creating convergence. Furthermore, the wind speeds in and around the updraft locations have speeds of 45-50 knots.

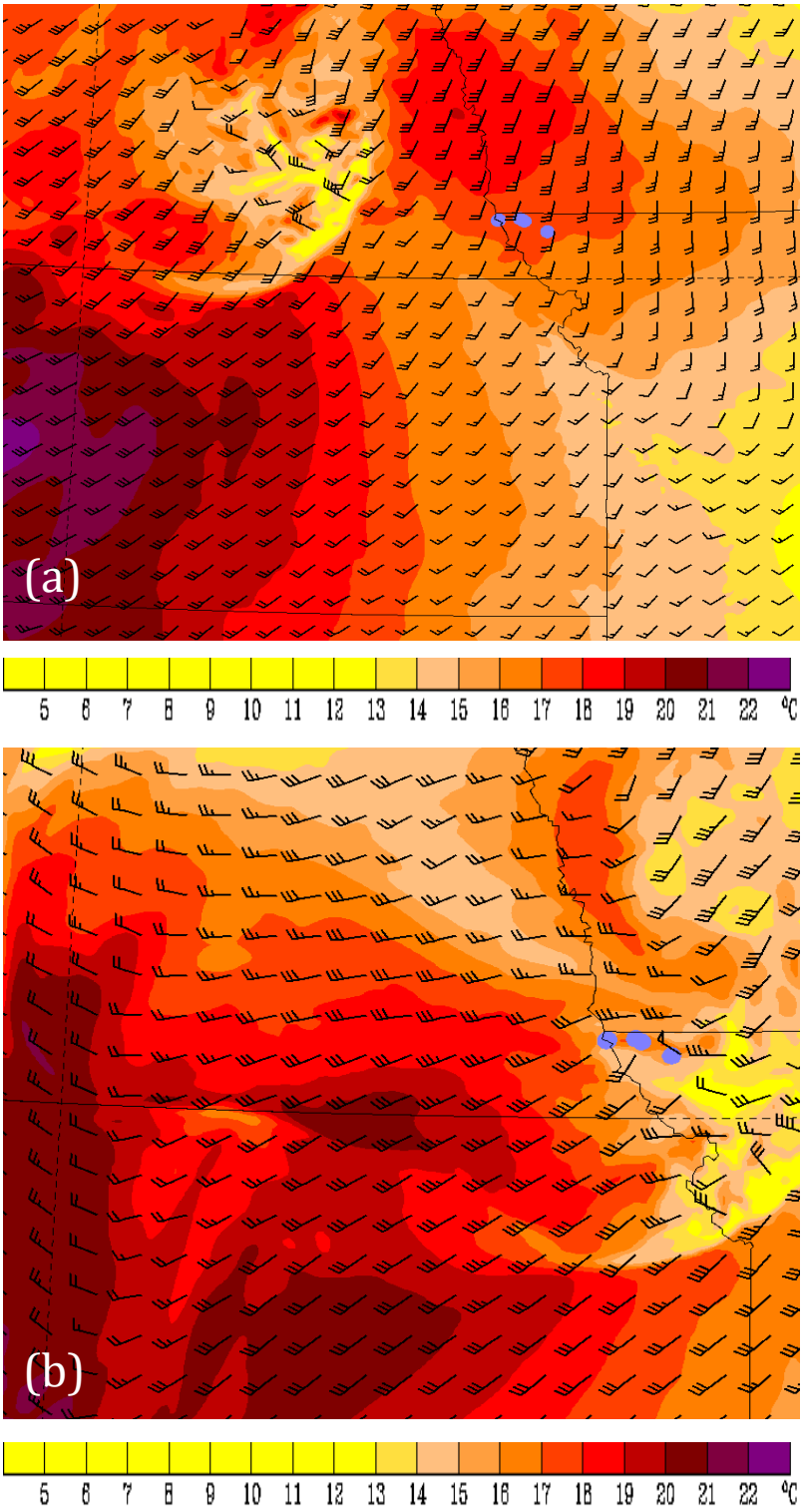


**Fig. 5.25.** As in Fig. 5.7, but for (a) 1100 UTC 15 September 2010, and (b) 1700 UTC 15 September 2010.

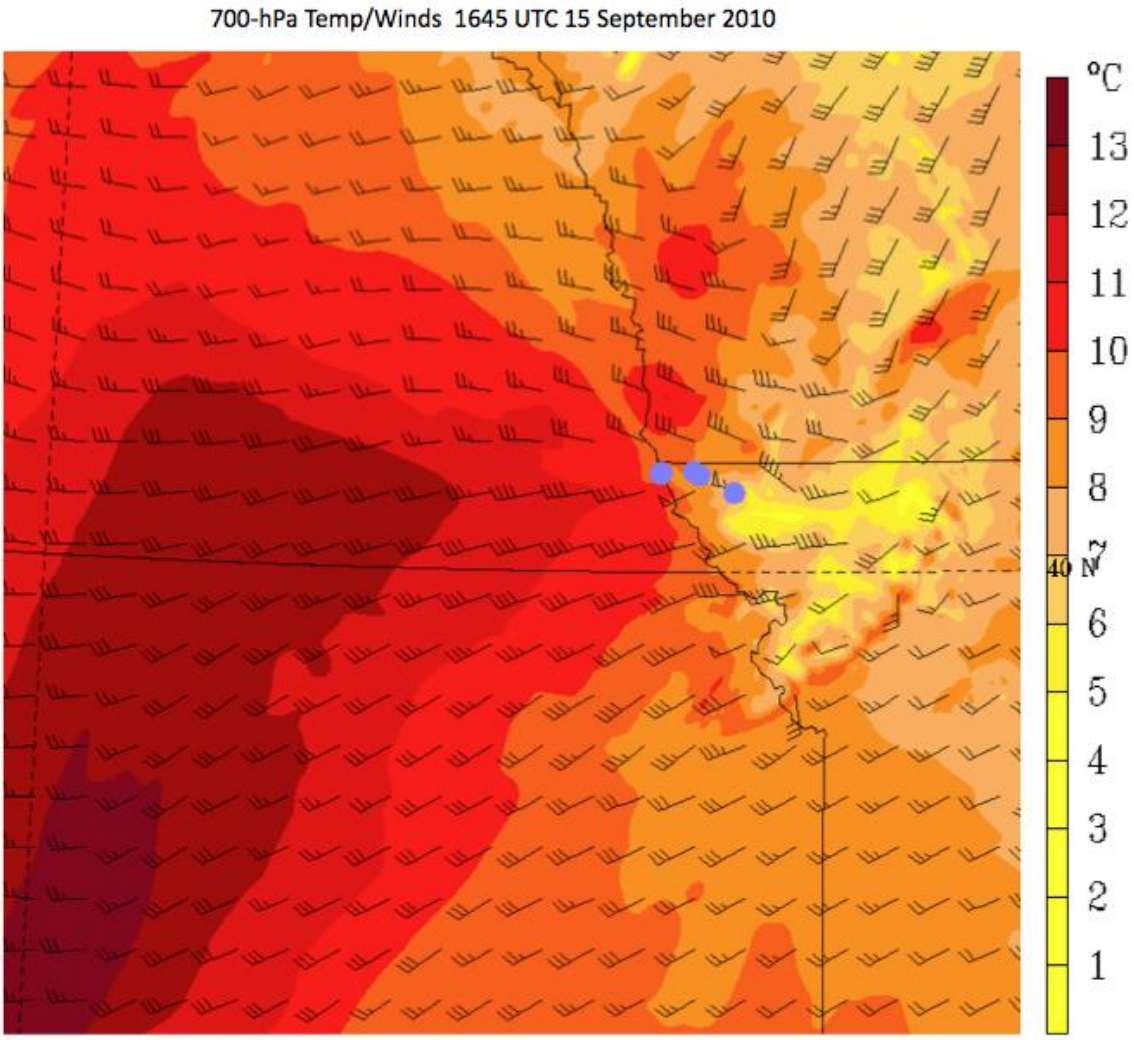


**Fig. 5.26.** As in Fig. 5.8, but for 1645 UTC 15 September 2010.

Potential temperature (with an overlay of CAPE contours) is shown in Fig. 5.27b. As before, to reference the location of this plot, Fig. 5.27a shows the XY-plane trajectory plot, with a solid black line to indicate the cross-section. The CAPE for this case is the weakest of the three, showing its highest value just above 2000 J $kg^{-1}$. Parcels gradually move vertically upward above the cold pool, and then enter a sharp updraft when they approach a region of stronger isentropic lifting. Additionally, it shows surface stabilization within the cold pool region, while elevated instability remains. Surface analysis is shown for this time, as well (Fig. 5.28). Although the cold pool is not nearly as extensive in size behind the bow echo for this case, it is still evident in shades of green and yellow. This still verifies that the location for the greatest updraft was not occurring in an orientation along the outflow boundary. This analysis is, again, similar to the observational surface analyses (Figs. 4.30 and 4.32), in that the temperature variations between the cold pool region (18°C to 24°C ) and the surrounding region (24°C to 30°C ) are all primarily consistent between the analyses. Additionally, the cold pool regions in the observational analyses are both fairly small, similar to the simulated analysis.

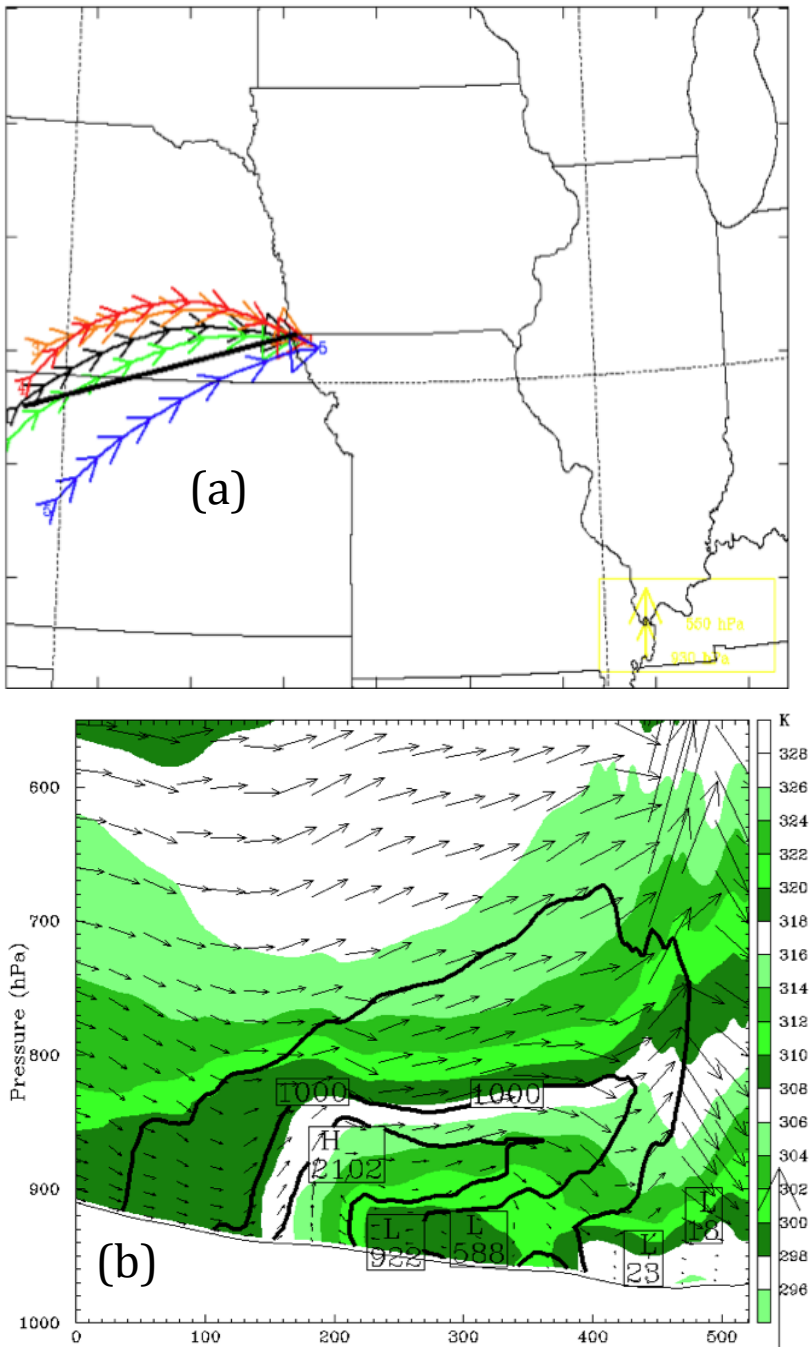


**Fig. 5.27.** (a) As in Fig. 5.22, but with a solid black line drawn across the trajectories to represent the location of the cross-section in 5.25a. (b) As in Fig. 5.9b, but at 1700 UTC 15 September 2010.

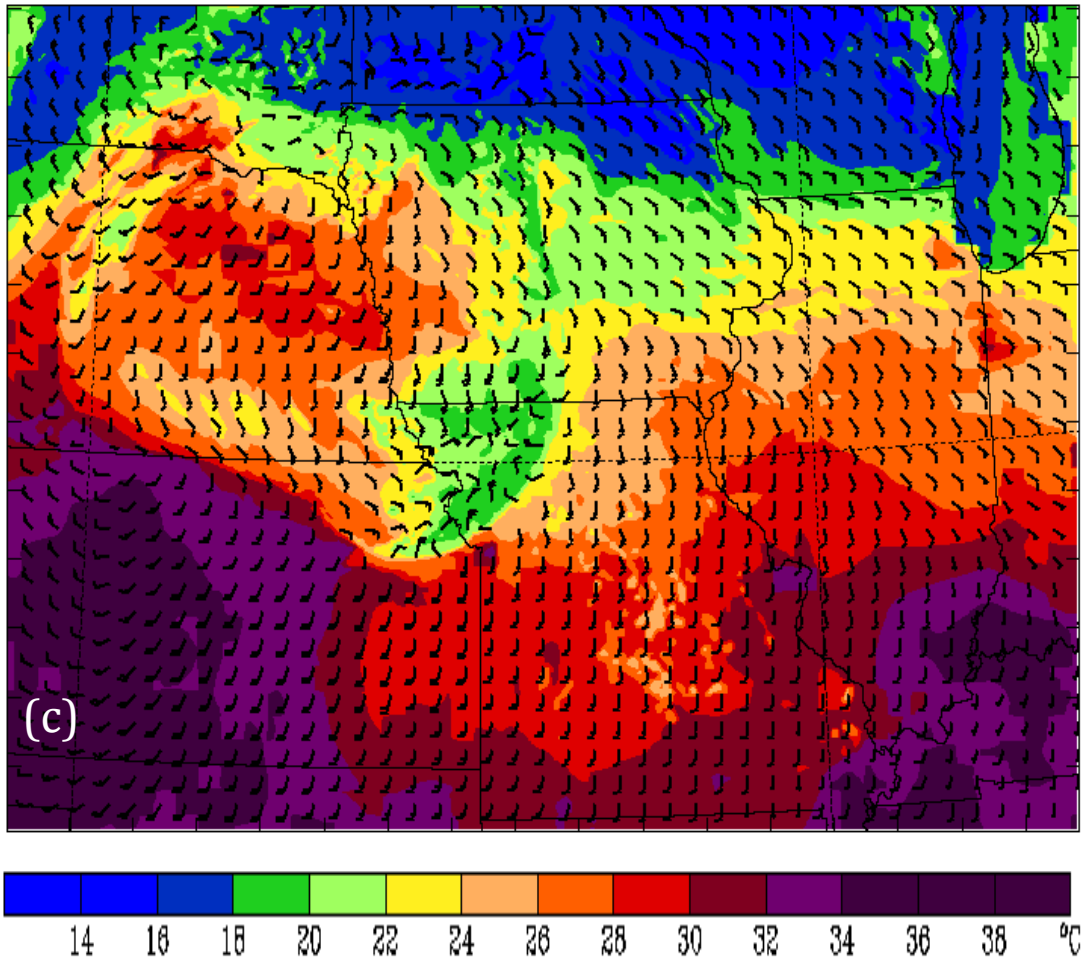


**Fig. 5.28.** Surface analysis for 1700 UTC 15 September 2010, where temperature is represented by colored contours, and wind barbs give wind direction and speed (in knots).

MUCAPE is shown in Fig. 5.29 for 1700 UTC. Just prior to this time, the updraft locations are in the stable cold pool region. At this time, two of the updraft regions are shown to be in an environment with 500-1000 J $kg^{-1}$ of CAPE. This is not a significant amount, but does create a small amount of thermodynamic instability for parcels.

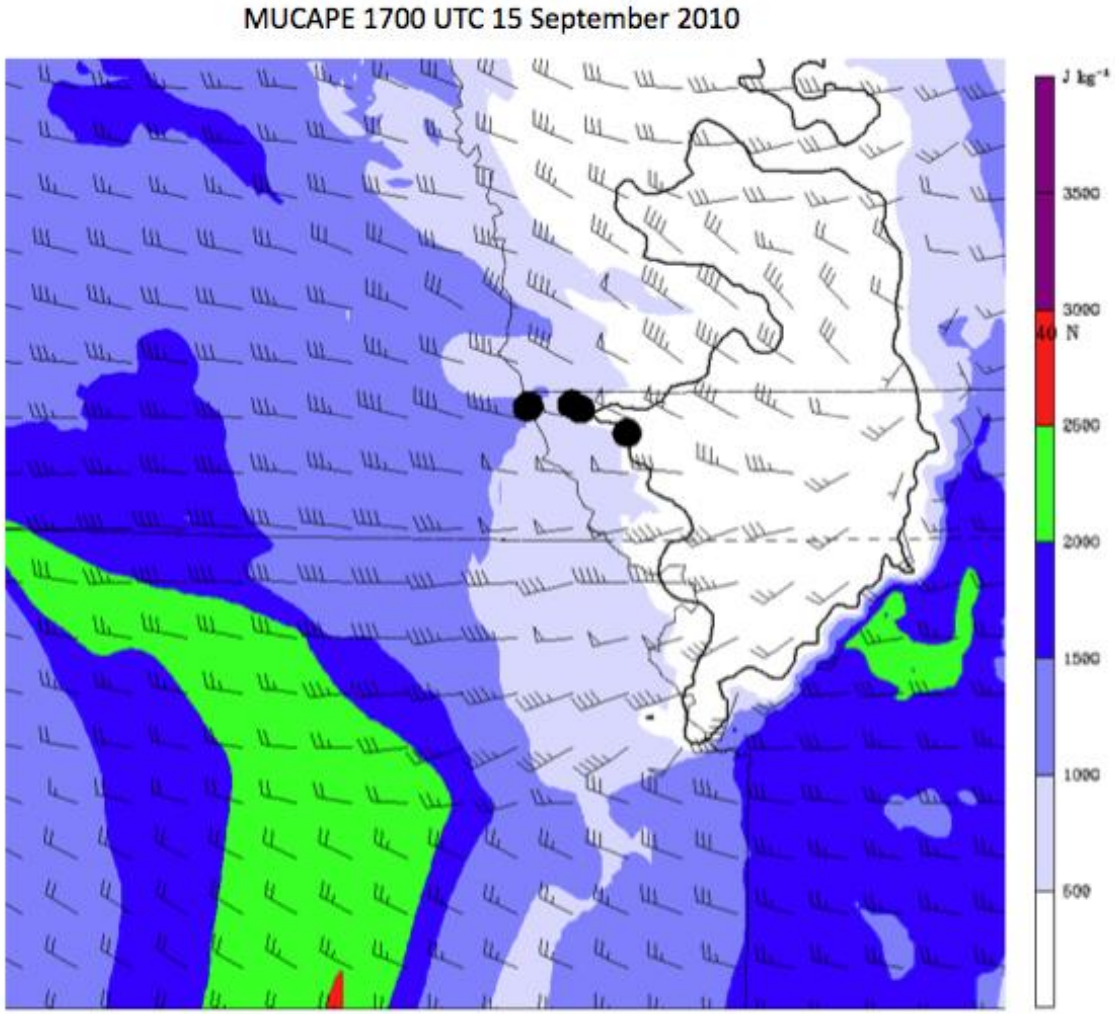


**Fig. 5.29.** As in Fig. 5.11, but for 1700 UTC 15 September 2010.

Many of the same factors are involved with this case, as with the prior two cases. At all levels, there is evidence of strong southwesterly winds, advecting warmer temperatures into the convective arrow region. Evidence of speed shear and convergence exists, although not at the lowest layers, which differentiates this case from the others. The wind speeds are higher in the region of the arrow,

indicative of a potential rear-inflow jet, which may be resulting in the linear orientation of the arrow. Instability is not quite as substantial in this case, but if other ingredients are in place, it only takes a small amount of instability to assist lifting.

There are a few noted differences between the cases, however. For instance, the source region for the arrow parcels varies from case to case. As shown in Fig. 5.3, there are two source regions for the 18 June 2006 case, while the other two cases only have essentially one horizontal location in which they originate. The parcels in the 08 May 2009 case all originate out of the southwest, at lower levels, however, while the parcels in the 15 September 2010 case begin more out of the west, from slightly higher up in the atmosphere. Another difference is that the orientation of the converging winds (in the arrow region) is inconsistent between cases. Additionally, there is no convergence present at the 850-hPa level for the 15 September 2010 case, while it is present for the other cases at that level. Regardless of these differences from case to case, they all provide the same ending result.

# 6. CONCLUSIONS AND FUTURE WORK

## 6.1 Conclusions

Over the course of 12 warm seasons, 14 cases of the bow and arrow phenomenon are identified. It has been shown that forecasting for such an event is difficult due to lack of detection by modeling products, in addition to no prior research explaining the causes of this phenomenon. Failure to produce accurate forecasts can lead to little or no warning for harmful consequences, such as flooding, hail, and severe wind damage, associated with bow and arrows.

A number of studies have been conducted in the past regarding the environmental conditions and ingredients needed to produce and maintain strong MCSs, as well as bow echoes. All research done in this area shows that the cold pool behind the leading line of convection (whether it is linear, or bow shaped) stabilizes the mesoscale environment, inhibiting convection from initiating within that column of air. Studies have shown that the cold pool can serve as a boundary, sometimes inducing secondary convection around its periphery; however, as revealed in this study, the convective arrow is capable of forming behind, and sometimes above the cold pool. Additionally, the convection forms in an orientation that is perpendicular to the leading line of convection (i.e. not along the periphery of the cold pool).

Observational analysis is performed to try to obtain a better understanding of the true environments prior to, and during the bow and arrow events. After

studying multiple analyses for four separate cases, it is determined that available observational data are limited, and therefore analyses are relatively coarse, giving little indication of the intricate details of each system. With each of these cases, the observations provide undeniable evidence that the ingredients are plentiful for producing major MCS and bow echo events. The observations do not, however, provide any insight into the rationale behind initiation and maintenance of the arrow portion of the bow and arrow system.

Output from high-resolution numerical model simulations is analyzed at a much finer spatial and temporal resolution than that of observational analysis. Three events are studied in detail to determine common characteristics among the cases that may be responsible for causing a bow and arrow event. Among the cases, several similarities were identified, as well as a few differences.

The environmental attribute that remains constant for all three cases is southwesterly flow into the arrow region (which is also found to be evident in the observational cases, as well). This is indicative of the existence of a LLJ, which is helpful in fueling the environment with instability, via its transport of warm and moist air into the area. For all cases, this southwesterly flow contributes to warm air advection, creating gradual isentropic lifting of parcels across the region and into the area in which the arrow is formed.

Although the orientation of the convergence differs for each case, it is always evident in the arrow region behind the bow. Winds converge in this region, and then turn sharply into the back of the bow echo, into what is assumed to be the

rear-inflow jet. Additionally, these converging winds typically have varying speeds (with stronger winds out of the southwest, converging with weaker winds out of the northwest or west). This creates horizontal speed shear, which when combined with convergence may enhance lifting in the arrow region. Furthermore, when combined with the increased wind speeds, induced by the rear-inflow jet, this speed shear may work to maintain the linear orientation of the convective arrow, via deformation.

It seems as though, when all of these characteristics are in place, in addition to even a relatively small amount of thermodynamic energy (CAPE), there is a greater possibility of the formation of convection behind the bow echo, and above the cold pool, as well as the orientation of the convective arrow to maintain linearity.

## 6.2 Indications for Future Work

Although some environmental characteristics have been identified as possibly initiating and maintaining a convective arrow, there are still several unanswered questions and opportunity to expand this study. For this study, a total of 14 cases are identified; however it is likely that many more exist. In the absence of a full climatology, 14 cases in 12 warm seasons, via the methods used to identify them, shows that this is not a rare occurrence. Given the consequences that evolve from such an event, it would be beneficial to try to obtain a much larger sample size of events for examination.

Because so many of the events are either unable to be reproduced by numerical simulation, or data are not available to conduct these simulations, having more events would increase the likelihood of more successful simulations. Additional analyses of extra events would help to further solidify results found in this study, as well as to possibly provide other explanations that were not found in the three cases studied here.

Figuring out the difference in environments from cases that do not create an arrow behind a bow echo is just as important as figuring out what does create the arrow. This is something that was attempted for this study, but due to a lack of cooperative simulations, this was not possible. Simulations that were unsuccessful in creating an arrow also failed to produce a bow echo. Ideally, using ensemble forecasts would create a variety of possible scenarios that would, perhaps, have simulations that would create bow and arrows, as well as those that only create the bow echo. Using several scenarios from one event would provide a more controlled study.

Finally, a detailed investigation of the problems in the numerical models, that inhibit them from producing accurate results, is needed. The fact that several cases in this study were unsuccessfully simulated, further highlights the depth of the problem forecasters face when trying to accurately predict for a bow and arrow event. If certain aspects of the model were found to be faulty, and were improved, this would not only help with forecasting precision and timely warnings to the public, but would help to improve efficiency in this type of research.

All of these implications for future work would help to improve the scientific theory behind bow and arrows, and the larger-scaled systems they are part of. They would help researchers to conduct more thorough analysis, and to formulate more solid hypotheses for an understanding of what environmental factors are necessary to create and maintain this type of event so that they may forecast more accurately. This, in turn, would then help the forecasting community to be able to understand and recognize key components that may lead to a bow and arrow event. The primary purpose of forecasting is to maintain safety for the public. When forecasts are accurate, the public is properly warned, which enhances protection of lives, health, and safety.

## REFERENCES

American Meteorological Society, 2011: Glossary of meteorology, [Available from: http: //amsglossary.allenpress.com/glossary/search?p=1&query=bow+echo&submit=Search].

Augustine, J. A. and F. Caracena, 1993: Lower-tropospheric precursors to nocturnal MCS development over the central United States. *Wea. Forecasting,* **9,** 116-135.

Carbone, R. E., J. D. Tuttle, D. A. Ahijevych, and S. B. Trier, 2002: Inferences of predictability associated with warm season precipitation episodes. *J. Atmos. Sci.,* **59,** 2033-2056.

Chappell, C. F., 1986: Quasi-stationary convective events. *Mesoscale Meteorology and Forecasting,* P. S. Ray, Ed. Amer. Meteor. Soc., 289-310.

Charba, J. P., 1974: Application of gravity current model to analysis of squall-line gust front. *Mon. Wea. Rev.,* **102,** 140-156.

Coniglio, M. C., S. F. Corfidi, and J. S. Kain, 2011: Environment and early evolution of the 8 May 2009 derecho-producing convective system. *Mon. Wea. Rev.,* **139,** 1083-1102.

Corfidi, S. F., 2003: Cold pools and MCS propagation: forecasting the motion of downwind-developing MCSs. *Wea. Forecasting,* **18,** 997-1017.

Cotton, M. –S. Lin, R. L. McAnelly, and C. J. Tremback, 1989: A composite model of mesoscale convective complexes. *Mon. Wea. Rev.,* **117,** 765-783.

Dawson II, D. T., M. Xue, J. A. Milbrandt, M. K. Yau, and G. Zhang, 2007: Impact of multi-moment microphysics and model resolution on predicted cold pool and reflectivity intensity and structures in the Oklahoma tornadic supercell storms of 3 May 1999. *22nd Conference on Weather Analysis and Forecasting/18th Conference on Numerical Weather Prediction.* Park City, UT, American Meteorological Society, 10B.2. [Available online at: http: //ams.confex.com/ams/22WAF18NWP/techprogram/paper_124706.htm].

Done, J., C. A. Davis, and M. L. Weisman, 2004: The next generation of NWP: explicit forecasts of convection using the Weather Research and Forecasting (WRF) model. *Atmos. Sci. Lett.,* **5,** 110-117, doi:10.1002/asl.72.

Doswell, C. A. III, H. E. Brooks, and R. A. Maddox, 1996: Flash flood forecasting: an ingredients-based methodology. *Wea. Forecasting,* **11,** 560-581.

Fujita, T. T., 1955: Results of detailed synoptic studies of squall lines. *Tellus,* **7,** 405-436.

------, 1978: Manual of downburst identification for project NIMROD. Satellite and Mesometeorology Research Paper No 156, Department of Geophysical Sciences, University of Chicago, 104 pp.

Fulton, R. A., J. P. Breidenbach, D. –J. Seo, D. A. Miller, and T. O'Bannon, 1998: The WSR-88D rainfall algorithm. *Wea. Forecasting,* **13,** 377-395.

Goff, R. C., 1976: Vertical structure of thunderstorm outflows. *Mon. Wea. Rev.,* **104,** 1429-1440.

Hamilton, R. E., 1970: Use of detailed intensity radar data in mesoscale surface analysis of the 4 July 1969 storm in Ohio. Preprints, *14th Conf. on Radar Meteorology,* Tucson, Amer. Meteor. Soc., 339-342.

Hong, S. and J. J. Lim, 2006: The WRF single-moment 6-class microphysics scheme (WSM6). *J. Korean Meteor. Soc.,* **42,** 129-151.

Houze, R. A., Jr., B. F. Smull, and P. Dodge, 1989: Mesoscale organization of springtime rainstorms in Oklahoma. *Mon. Wea. Rev.,* **118,** 613-654.

Janjic, Z. I., 1994: The step-mountain Eta coordinate model: further developments of convection, viscous sublayer, and turbulence closure schemes. *Mon. Wea. Rev.,* **122,** 927-945.

Johns, R. H., and W. D. Hirt, 1987: Derechos: widespread convectively induced windstorms. *Wea. Forecasting,* **2,** 32-49.

Johnson, R. H. and P. J. Hamilton, 1988: The relationship of surface pressure features to the precipitation and air flow structure of an intense midlatitude squall line. *Mon. Wea. Rev.,* **116,** 1444-1472.

Kain, J. S., 2004: The Kain-Fritsch convective parameterization: an update. *J. Appl. Meteor.,* **43,** 170-181.

Koch, S. E., M. DesJardins, and P. J. Kocin, 1983: An interactive Barnes objective Map analysis scheme for use with satellite and conventional data. *J. Climate Appl. Meteor.,* **22,** 1487-1503,

Lee, W. -C., R. E. Carbone, and R. M. Wakimoto, 1992: The evolution and structure Of a "bow-echo-microburst" event. Part II: The bow echo. *Mon. Wea. Rev.,* **120,** 2211-2225.

Lin, Y. and K. E. Mitchell, 2005: The NCEP stage II/IV hourly precipitation analyses: development and applications. *19th Conf. on Hydrology,* San Diego, CA, Amer. Meteor. Soc. 439-451.

Maddox, R. A., 1980: Mesoscale convective complexes. *Bull. Amer. Meteor. Soc.,* **61,** 1374-1387.

Metz, N. D. and L. F. Bosart, 2010: Derecho and MCS development, evolution, and multiscale interactions during 3-5 July 2003. *Mon. Wea. Rev.,* **138,** 3048-3070.

Moller, A. R., C. A. Doswell III, M. P. Foster, and G. R. Woodall, 1994: The operational recognition of supercell thunderstorm environments and storm structure. *Wea. Forecasting,* **9,** 327-347.

NOAA, cited 2011a: National Oceanic and Atmospheric Administration Hydrometeorological Prediction Center Synoptic Scale Analysis Archive. [Available online at http: //www.spc.noaa.gov/exper/archive/events].

------, cited 2011b: National Oceanic and Atmospheric Administration Storm Prediction Center Storm Report Archive, and Convective Outlook Report Archive. [Available online at http: //www.spc.noaa.gov/archive/].

------, cited 2011c: Natural hazard statistics. [Available online at http://www.nws.noaa.gov/om/hazstats.shtml.]

Nolen, R. H., 1959: A radar pattern associated with tornadoes. *Bull. Amer. Meteor. Soc.,* **40,** 277-279.

Parker, M. D., and R. H. Johnson, 2000: Organizational modes of midlatitude mesoscale convective systems. *Mon. Wea. Rev.*, **128,** 3413-3436.

Przybylinski, R. W., and D. M. DeClaire, 1985: Radar signatures associated with the derecho: one type of mesoscale convective system. Preprints, *14th Conf. on Severe Local Storms,* Indianapolis, IN, Amer. Meteor. Soc., 228-231.

Purdom, F. W., 1973: Meso-highs and satellite imagery. *Mon. Wea. Rev.,* **101,** 180-181.

Rotunno, R., J. B. Klemp, and M. L. Weisman, 1988: A theory for strong, long-lived squall lines. *J. Atmos. Sci.,* **45,** 463-485.

Schumacher, R. S., and R. H. Johnson, 2005: Organization and environmental properties of extreme-rain-producing mesoscale convective systems. *Mon. Wea. Rev.,* **133,** 961-976.

------ and ------, 2006: Characteristics of U.S. extreme rain events. *Wea. Forecasting,* **21,** 69-85.

Skamarock, W. C., J. B. Klemp, J. Dudhia, D. O. Gill, D. M. Barker, W. Wang, and J. G. Powers, cited 2011: A description of the Advanced Research WRF version 3. NCAR Tech. Note NCAR/TN-475+STR, 100 pp. [Available online at http: // www.mmm.ucar.edu/wrf/users/docs/arw_v3.pdf].

------ and M. L. Weisman, 2008: The impact of positive-definite moisture transport on NWP precipitation forecasts. *Mon. Wea. Rev.,* **137,** 488-494.

Smull, B. F. and R. A. Houze, Jr., 1985: A midlatitude squall line with a trailing Region of stratiform rain: radar and satellite observations. *Mon. Wea. Rev.,* **113,** 117-133.

------, and ------, 1987: Rear inflow in squall lines with trailing-stratiform precipitation. *Mon. Wea. Rev.,* **115,** 2869-2889.

Thompson, G., P. R. Field, R. M. Rasmussen, and W. D. Hall, 2008: Explicit forecasts of winter precipitation using an improved bulk microphysics scheme. Part II: implementation of a new snow parameterization. *Mon. Wea. Rev.,* **136,** 5095-5115.

Trier, S. B. and D. B. Parsons, 1992: Evolution of environmental conditions preceding the development of a nocturnal mesoscale convective complex. *Mon. Wea. Rev.,* **121,** 1078-1098.

------, 2010: Environmental controls on the simulated diurnal cycle of warm-season precipitation in the continental United States. *J. Atmos. Sci.,* **67,** 1066-1090.

Weisman, M. L., and J. B. Klemp, 1986: Characteristics of isolated convective storms. *Mesoscale Meteorology and Forecasting.* Peter S. Ray, Ed., Amer. Meteor. Soc., 331-358.

------, ------, and R. Rotunno, 1988: Structure and evolution of numerically simulated squall lines. *J. Atmos. Sci.,* **45,** 1990-2013.

------, 1992: The genesis of severe, long-lives bow echoes. *J. Atmos. Sci.,* **50,** 645-670.

------, C. Davis, W. Wang, K. W. Manning, and J. B. Klemp, 2008: Experiences with 0-36-h explicit convective forecasts with the WRF-ARW model. *Wea. Forecasting,* **23,** 407-437.

# VITA


| | |
|---|---|
| Name: | Kelly M. Keene |
| Address: | 1204 Eller O&M<br>3150 TAMU<br>College Station, TX 77843-3150 |
| Email Address: | kellykeene44@gmail.com |
| Education: | B.S., Geography, The University of Georgia, 2009<br>Certificate, Atmospheric Science, The University of Georgia, 2009<br>M.S., Atmospheric Science, Texas A&M University, 2011 |